Report Submitted to	Erika Coffey Carbon Management | CO2 Removal and Conversion U.S. DOE, National Energy Technology Laboratory 3610 Collins Ferry Road Morgantown, WV 26505 Tel: 304.285.5306 Email: erika.coffey@netl.doe.gov	Naomi O’Neil, Ph.D. Carbon Capture Team U.S. DOE, National Energy Technology Laboratory 626 Cochrans Mill Road P.O. Box 10940 Pittsburgh, PA 15236 Tel: 412-386-7668 Email: naomi.oneil@netl.doe.gov
Project Number	DE-FE-0031919	
Project Title	High-Efficiency Electrochemical Conversion of CO_2 to Ethylene	
PI Contact Information	Professor Xiao-Dong Zhou 131 Rex Street University of Louisiana at Lafayette Lafayette, LA 70504 Tel: 337-482-1453 E-mail: zhou@louisiana.edu	
Submitted by	Professor Xiao-Dong Zhou 131 Rex Street University of Louisiana at Lafayette Lafayette, LA 70504 Tel: 337-482-1453 E-mail: zhou@louisiana.edu	
Submission Date	November 15, 2023	
DUNS	11-131-0249	
Recipient Organization	Sponsored Programs Office University of Louisiana at Lafayette	
Project Period	09/01/2020 – 08/31/2023	
Final Report	08/31/2023	
Report Frequency	Final Report	
Signature		

DISCLAIMER* --

High-Efficiency Electrochemical Conversion of CO_2 to Ethylene

A. EXECUTIVE SUMMARY

During the past century, our civilization's technological advances have been driven by the conversion of carbon-rich fossil fuels into electricity, heat, polymers, fertilizers, and other carbon-based products that are the foundation of modern society. It is now clear, however, that this carbon economy is no longer sustainable for humanity or our ecosystem. A study by the National Academies showed that to avoid catastrophic climate change, we not only need to dramatically and rapidly reduce global emissions of CO_2, but we will need to remove billions of tons of CO_2 from the earth's atmosphere and oceans by mid-century.[1] This presents a massive, unprecedented challenge to our species,[2] but if managed well it also represents a historic opportunity: capture and utilization of CO_2 is arguably the largest economic opportunity of the next hundred years, also known as "industry of the future".[3]

Numerous projects have been funded by US DOE to support the R&D of CO_2 capture, storage, and utilization, particularly CO_2 from coal-fired power plants. The DOE University Coal Program (UCR) has been successfully operated since 1979. The ultimate goal of DOE's Carbon Storage Program is to develop and advance both onshore and offshore carbon storage technologies that will significantly improve the effectiveness of the technology, reduce the cost of implementation, and be ready for widespread commercial deployment in the 2025–2035 timeframe. The aim of this project is to support one of five goals of the Carbon Storage program: *to develop and test technologies that can utilize CO_2 from coal-fired power plants to reduce the emissions and create valuable products to offset the cost of CCS*.

It is well known that a long-lasting challenge in CO_2 utilization is the cost. CO_2 can be used as a precursor in a number of physical and chemical processes, including enhanced oil recovery, beverages and microcapsules, and production of syngas, carboxylates, urea and so on. The underlying questions are "*can these processes create products with additional values*" and "*will the product have a large enough market so that it can potentially transform millions of tons CO_2*". The main objective of this research is to address these two questions by developing a highly active and durable electrode that can be paired with pulsed electrolysis for the cost-effective conversion of CO_2 to ethylene. This project invokes a systematic and intensive effort focused on translating our theoretical understanding of the electrocatalyst and electrochemical engineering to

1. design and fabricate tandem electrodes with active and distinct Cu and carbon-based catalysts to direct cascade process of $CO_2 \rightarrow CO \rightarrow C_2H_4$,
2. develop functionally graded catalyst layers,
3. research and develop pulsed electrolysis technology, and
4. combine them for the conversion of CO_2 to value-added C_2H_4 with a selectivity of 90% and an energy efficiency of 50% at a partial current density of 1,000 mA cm^{-2} in a MEA-type cell.

B. Task 2 and 3. Design and Fabricate Tandem Electrodes and Develop Functionally Graded Catalyst Layers

B.1. Introduction

In the reaction of CO_2 to C_{2+} on Cu, the kinetics of the rate-determining step, which dictates the partial current density for C_{2+} products (j_{C2+}),[5-9] depends on the adsorption energy of adsorbed carbon monoxide (*CO) and, subsequently, on the *CO surface coverage (θ_{*CO}).[10-12] Therefore, recent work has attempted to increase the binding of *CO on Cu in order to increase the rate of conversion to C_{2+}.[6,13-16] Since θ_{*CO} is determined by the concentration of CO near the catalyst, the yield of C_{2+} products on Cu can be enhanced by increasing local CO concentration.[12,17] In particular, for vapor-fed systems that do not suffer from the concern of low CO solubility in the electrolyte, an increase in CO partial pressure has been shown to directly result in enhanced C_{2+} production.[18]

Cascade CO_2RR systems, which integrate two consecutive steps of CO_2-to-CO and CO-to-C_{2+} on two distinct catalytic sites, can intensify the θ_{*CO} on a Cu surface.[19-23] In these systems, one catalyst material selectively converts CO_2 to CO to provide an *in-situ* source of CO that enhances θ_{*CO}, and another Cu-containing catalyst performs C-C coupling. Since the θ_{*CO} is often the limiting factor, higher j_{C2+} values can be achieved by increasing the local CO partial pressure (P_{CO}) with increased CO generation rates.[12,26,27] However, if the rate of CO generation exceeds the rate of C-C coupling, CO utilization and C_{2+} FE are diminished.[20,22,25,28] This tradeoff presents a need to manage *in situ* CO formation in order to maximize the C_{2+} FE while still maintaining high j_{C2+}.[29,30]

This task aims 1) to investigate the interplay of CO transport and CO-CO coupling reaction kinetics, 2) to determine the optimal spatial distribution of catalyst layers in tandem electrodes to maximize the CO utilization efficiency in the CO-CO coupling reaction, 3) to balance the loadings of two distinct catalysts in the tandem electrodes to reach a maximum Faradaic efficiency (FE) of C_2H_4, and 4) finally to establish the design principle of tandem electrodes to steer efficient cascade reaction of $CO_2 \rightarrow CO \rightarrow C_2H_4$.

B.2. Experimental Method

B.2.1. Multiphysics simulation

The simulation was performed using the COMSOL Multiphysics 5.6 software package. The Navier-Stokes equations were used to solve the bulk fluid transport within the flow channel. Darcy's Law described the flow of fluid through a porous medium. The concentration of species was solved in throughout the domain by solving species conservation, and the θ_{*CO} was defined by the Langmuir adsorption model.

B.2.2. Preparation of the segmented gas-diffusion electrode

The Cu catalyst ink was prepared by dispersing 200 mg of Cu nanoparticles (25 nm, MilliporeSigma) in a solvent mixture followed by ultrasonication for 30 minutes. The solvent mixture is comprised of 20 mL water, 20 mL isopropyl alcohol, and 500 µL Sustainion XA-9 ionomer solution (5 wt.%). The Ag (20-40 nm, Alfa Aesar), ZnO (< 100 nm, MilliporeSigma), and Fe-N-C catalyst inks were prepared using the same procedure. The volume of solvent and ionomer solution was adjusted in proportion to the catalyst weight. The Cu catalyst ink was firstly sprayed onto the $8.0 \times 25.0\ cm^2$ gas diffusion layer (GDL, Sigracet 39BC) to fabricate a uniform Cu GDE. The actual loading of Cu catalyst was $0.40\ mg\ cm^{-2}$ unless otherwise stated. The catalyst loading was determined by weighing the electrode before and after the spraying. This Cu GDE was then cut into four equal pieces (2.0 × 25.0 cm^2). Three of them were used for subsequent coating with CO-selective catalyst inks, while the fourth piece was used as a control electrode.

The Cu GDE was then covered by various templates made of polyethylene terephthalate plastic. The templates were machined to open windows with different lengths of 0.10, 0.20, 0.40, 0.80, 1.20, 1.60, and 1.90 cm. Afterward, the Ag catalyst ink was sprayed onto the Cu CL to form an Ag CL segment with a constrained area at one end of the electrode. The mass of Ag catalyst was fixed to 0.04 mg for each 1.0 cm^2 stacked SGDE. The quantity was determined by weighing a large piece of the electrode before and after the spraying. The templates with lengths of 1.0 mm and 19.0 mm were used together to fabricate the co-planar Cu/Ag SGDE. The mass of Cu and Ag catalyst in each 1.0 cm^2 co-planar Cu/Ag SGDE is also 0.40 and 0.04 mg, respectively. Following spraying, the SGDEs were dried at 60 °C in the vacuum oven. Finally, the big sheet of stacked SGDE was cut into smaller samples with dimensions of 2.00 cm (length, L) × 0.50 cm (width, W) corresponding to an area of 1.00 cm^2 for the electrochemical tests. For the co-planar Cu/Ag SGDE, the Cu and Ag CLs had the same width of 0.50 cm, and the segment areas were 0.95 and 0.05 cm^2 for Cu and Ag CLs, respectively. The Cu/Ag (1.00:1.00) SGDE, which has an equal area of 1.00 cm^2 for Cu and Ag CLs segments, is equivalent to the l-GDE. The Cu/ZnO and Cu/Fe-N-C SGDEs were fabricated by following the same procedure. The doubly loaded Cu/Fe-N-C SGDE contained a Cu loading of 0.80 mg cm^{-2} and Fe-N-C mass of around 0.08 mg for each 1.0 cm^2 electrode.

B.2.3. Electrode characterization

The cross-sectional area of the electrode was imaged by scanning electron microscopy (SEM, FEI SCIOS DualBeam). The SEM samples were prepared by breaking the electrodes in liquid N_2. The optical images of electrodes were taken by optical microscopes (Keyence VHX-2000E).

The electrochemically active surface area was determined by measuring the double-layer capacitance (C_{dl}) of the corresponding electrodes in Ar-purged 1.0 M KOH in an H-type electrolyzer. To exclude the effect of carbon paper, the backside of the electrode was sealed with epoxy and only left the CL exposed. The scan rate varied from 10 to 100 mV s^{-1} in the non-Faradaic potential range. The obtained current was plotted as a function of the scan rate to derive the C_{dl}.

B.2.4. CO_2 electrochemical reduction in the MEA and flow cell

The activity and selectivity of both SGDE and l-GDE were tested in a customized MEA electrolyzer comprising the GDE cathode, Sustainion anion exchange membrane, and the Ni-Fe LDH coated Ni foam as the anode. The 0.50 M KOH or 0.10 M $KHCO_3$ anolyte stream that flowed through the anode at a rate of 5.00 mL min^{-1} was controlled by a peristaltic pump (Harvard Apparatus P70-7000). The dry CO_2 feedstock was supplied to the cathode at a rate of 20 sccm controlled by a mass flow controller (Alicat Scientific MC-100SCCM-D). The applied cell voltage was controlled by a potentiostatic/galvanostatic station (Solartron EnergyLab XM). The anode potential was monitored online in reference to a saturated calomel electrode (SCE). The gas products were quantified by gas chromatography (GC, Agilent 7890B), while liquid products were measured by ^{1}H nuclear magnetic resonance spectroscopy (Bruker AV500).

The FE of each gas product was calculated based on a prior equation where the outlet CO_2 flow rate was accurately measured.[29] For the measurement of outlet CO_2 flow rate, a constant stream of Ar gas (10 sccm) was used as an internal reference and evenly mixed with the cell outlet gas stream before it was injected into the GC column. The standard curve for CO_2 flow rate was established by a similar way of mixing the 10 sccm Ar gas with a pure CO_2 stream with a flow rate varying from 5 to 100 sccm. The concentration of other gas components was quantified by using CO_2 as the internal reference. The standard GC calibration curves for the other gas components were established based on three standard calibration gases, comprising 1000, 2000, and 5000 ppm of H_2, CO, CH_4, C_2H_4, and C_2H_6, respectively, with CO_2 as the balance gas.

The internal ohmic resistance between the cathode and anode was determined by electrochemical impedance spectroscopy operated under open-circuit voltage with a frequency ranging from 10^5 Hz to 0.01 Hz. Almost 90% of the measured cell resistances ranged from 0.20 to 0.30 Ω, while around 10% of cell resistance ranged from 0.50 to 0.60 Ω. Contact resistances resulting from cell assembly contributes 0.10 Ω variance whereas variations in the membrane ion conductivity from batch to batch accounts for another 0.30 Ω variance. Therefore, to deconvolute the impacts of these variances from the kinetic performance, the cell voltage was IR compensated unless otherwise stated. All the reported cell voltages were corrected by the measured cell internal resistance loss under each specific test unless otherwise stated. For the modified SGDEs, the cathode potential was obtained by subtracting the recorded anode potential from IR-free cell voltage.

The flow cell, including a 2 mm buffer layer of catholyte (0.5 M KOH), has a larger ohmic resistance (1.00 to 1.10 Ω) than that for the MEA electrolyzer. The test conditions in the flow cell were generally identical to those in the MEA electrolyzer except that a catholyte was supplied at a flow rate of 0.5 mL min^{-1}.

The long-term stability was operated under potentiostatic mode in which the cell voltage was controlled by the Solartron EnergyLab XM. During the long-term testing, gas and liquid products were periodically quantified by GC and ^1H NMR, respectively.

B.2.5. Calculation of the CO_2 reduction performance on each sub-segment

The Cu CL sub-segment (S_i) was defined as the difference in Cu CL segments between two consecutive modified SGDEs (E_i) as follows:

$$S_1 = E_1;\ S_i = E_i - E_{i-1}, (6 \geq i \geq 2)$$

where *i* is an integer. Correspondingly, the $j_{C_{2+}}$ for each sub-segment was calculated by finding the total current in each sub-segment and dividing by the sub-segment area as follows:

$$j_{C_{2+}}(S_1) = \frac{I_{C_{2+}}(E_1)}{A(E_1)};\ j_{C_{2+}}(S_i) = \frac{I_{C_{2+}}(E_i) - I_{C_{2+}}(E_{i-1})}{A(E_i) - A(E_{i-1})}, (6 \geq i \geq 2)$$

In this equation, $I_{C_{2+}}(E_i)$ is the total C_{2+} current (units of mA) in segment E_i, $A(E_i)$ is the area of segment E_i. and $j_{C_{2+}}(S_i)$ is the C_{2+} current density (units of mA cm^{-2}) in sub-segment S_i.

The outlet CO flow rate for each S_i was directly converted from the I_{CO} for the corresponding E_i according to the following equation.

$$Q_{CO}(S_i) = \frac{I_{CO}(E_i)}{nF}$$

where the Q_{CO} (mol s^{-1}) represents the flow rate of CO along the y-axis of the electrode within a given sub-segment, the n is the number of electron transfer (n = 2), and the F is Faraday's constant.

B.2.6. Calculation of CO_2 crossover

This work applied an Ar stream with a constant flow rate as an internal standard to calibrate the CO_2 flow rate; so that the CO_2 flow rate at the outlet can be accurately measured, as shown below.

$$\frac{Q_{CO_2}}{Q_{Ar}} = a \times \frac{A_{CO_2}}{A_{Ar}} + b$$

where the Q_{CO_2} and Q_{Ar} are the volumetric flow rate of CO_2 and Ar, while the Q_{Ar} is 10.00 sccm; the A_{CO_2} and A_{Ar} represent the peak area of CO_2 and Ar in the GC trace; the a and b are the slope and intercept of the calibration curve, respectively.

The difference in CO_2 flow rate between the inlet and outlet accounts for the CO_2 consumption and the CO_2 crossover to the anode side. The volumetric rate of CO_2 ($\dot{V}$) consumed by the Faradaic reaction can be calculated from the current.

$$\dot{V}_{consumption} = \frac{\sum \frac{I_i}{n_i * F} \times R \times T}{P}$$

where the n is the number of charge transfer for product i; F is the Faradaic constant; R is the gas constant; P is the gas pressure; T is the temperature.

Therefore, the volume of CO_2 crossover can be calculated as follows.

$$\dot{V}_{crossover} = \dot{V}_{inlet} - \dot{V}_{outlet} - \dot{V}_{consumption}$$

B.2.7. Cu-based catalyst synthesis

$Cu(OH)_2$ precursor was first synthesized by a precipitation method: 0.5 M $Cu(NO_3)_2 \cdot 3H_2O$ and 0.5 M NaOH were added dropwise into the deionized water under rapid stirring. The pH of the precipitating solution was kept at ~9. After aging for 8 h with stirring at room temperature and N_2 protection, the blue slurry was washed and centrifuged with water until the pH was close to 7. The precipitates were dried overnight in vacuum to obtain $Cu(OH)_2$ matrix. For a typical synthesis of the Rh-Cu catalyst, a calculated amount of $RhCl_3$ solution (1 mg ml^{-1}) was injected into $Cu(OH)_2$ solution (10 mg ml^{-1}) by a syringe pump at a rate of 10 μl s^{-1}. The mixture solution was stirred vigorously for 5 h. After the cation exchange process, the sample was washed, dried, and annealed at 330 °C for 3 h to obtain Rh-CuO product. Rh-Cu catalyst was then formed in situ by reducing Rh-CuO pre-catalyst on gas diffusion electrode (GDE) at −0.35 V for 10 min in a flow cell system supplied with CO_2 gas and 1 M KOH as electrolyte. ICP-OES was used to determine the mass loading of Rh. The preparation of other M-Cu samples with similar M atomic contents (Supplementary Table 7) was identical to that of the Rh-Cu catalyst except for using the corresponding metal salts instead of $RhCl_3$. The pristine Cu was obtained by direct calcination of $Cu(OH)_2$ followed by electroreduction.

B.2.8. Material characterizations

High-resolution SEM was performed on the FEI Apreo SEM. TEM, HAADF-STEM, and EDS elemental mapping were conducted using the JEOL ARM 200F microscope, which is equipped with a cold field emission gun and operated at 200 kV voltage. XPS data were collected from an ESCALAB Xi^+ spectrometer equipped with a monochromatic Al Kα radiation source operating at 200 W. XRD was carried out on the Malvern Panalytical Aeris research edition powder diffractometer using Cu Kα radiation. XAS measurements were performed on the Beamline 7-BM and 8-ID of the National Synchrotron Light Source II (NSLS II) at Brookhaven National Laboratory. The Athena and Artemis software in Demeter package was employed for data processing and analysis[55]. The theoretical EXAFS signal was fitted to the experimental EXAFS data in *R*-space by Fourier transforming both the theoretical and experimental data.

B.3. Results and Discussion

B.3.1. Track the C-C coupling reaction kinetics along the electrode length

We designed segmented gas diffusion electrode (SGDE), the second-generation tandem electrode following the layered GDE (LGDE), to manipulate the CO concentration gradient along the electrode length (**Figure 1**). The SGDE comprises of CO-selective and C_{2+}-selective catalyst layer (CL) segments. The CO-selective CL segment provides concentrated CO feedstock to the C_{2+}-selective CL segment along the electrode length, which substantially enhances *CO surface coverage and thereby C-C coupling reaction kinetics compared to the LGDE possessing dispersive and homogeneous CO feedstock along the electrode length.

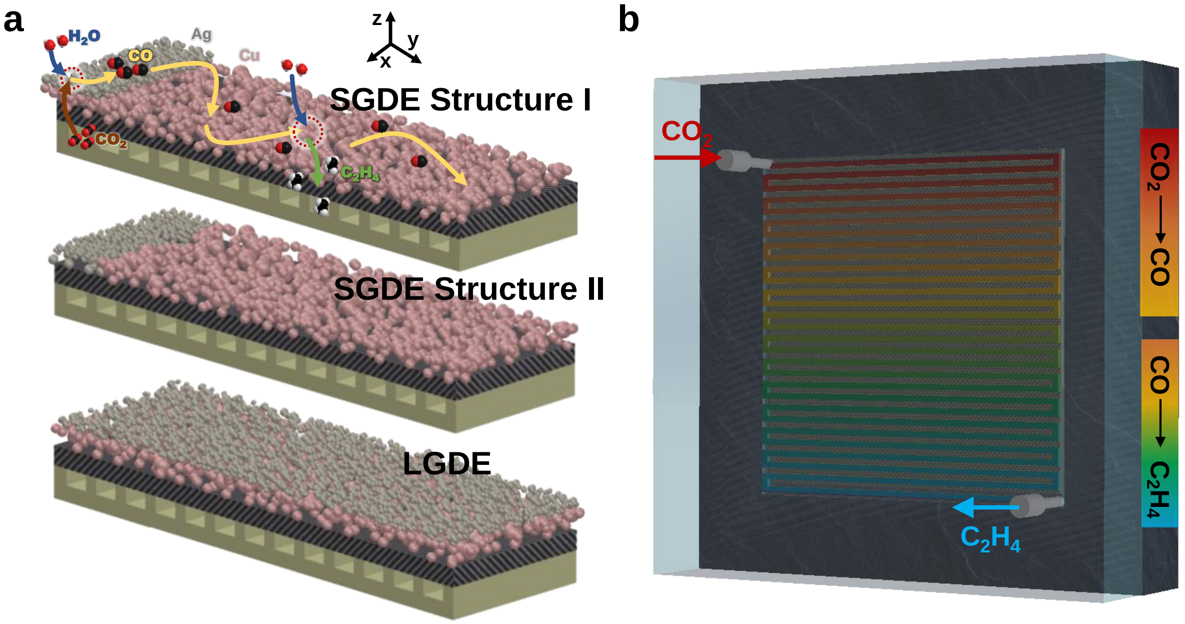

Figure 1. Concept of segmented tandem gas diffusion electrodes. (a) Schematic of structure I (top panel) and structure II (middle panel) segmented gas diffusion electrodes. For comparison,

the structure of the layered gas diffusion electrode is also displayed in the bottom panel. The arrows in structure I represent the reaction and mass transport of the proposed tandem reaction process in the catalyst layer. **(b)** Schematic of the gas concentration changing along the flow channel during the tandem reaction of $CO_2 \rightarrow CO \rightarrow C_2H_4$.

To guide the design of SGDE, we first tracked the interplay between CO flux and C-C coupling reaction kinetics. We developed a template-assisted spraying and post-exfoliation method to prepare six mapping SGDEs with varying length of Cu CL segment from 0.20 to 2.00 cm (designated as E1 to E6) while maintaining a consistent width of 0.50 cm (**Figure 2a**). In the electrode preparation process, the uniform Cu CL segment was firstly coated onto the gas diffusion layer (GDL) followed by a Ag CL segment (L 0.50 × W 0.10 cm^2) concentrated at the end of GDE. The area of Ag CL segment was precisely controlled by a machined template. Afterwards, a sub-segment with length varying from 0 to 1.80 cm in the Cu CL segment was exfoliated off the GDL. To prevent the undesired occurrence of the hydrogen evolution reaction (HER) on the carbon, the exposed GDL was sealed with epoxy. Simultaneously, the backside of the exposed carbon paper was sealed to prevent gas diffusion into the carbon paper/membrane interface. Except sub-segment S1 corresponging to Cu CL segment of E1 itself, each of sub-segments, S2 to S6, is assigned as the difference in the Cu CL segment of two consecutive electrodes (for example, S2 = E2-E1) (**Figure 2e**).

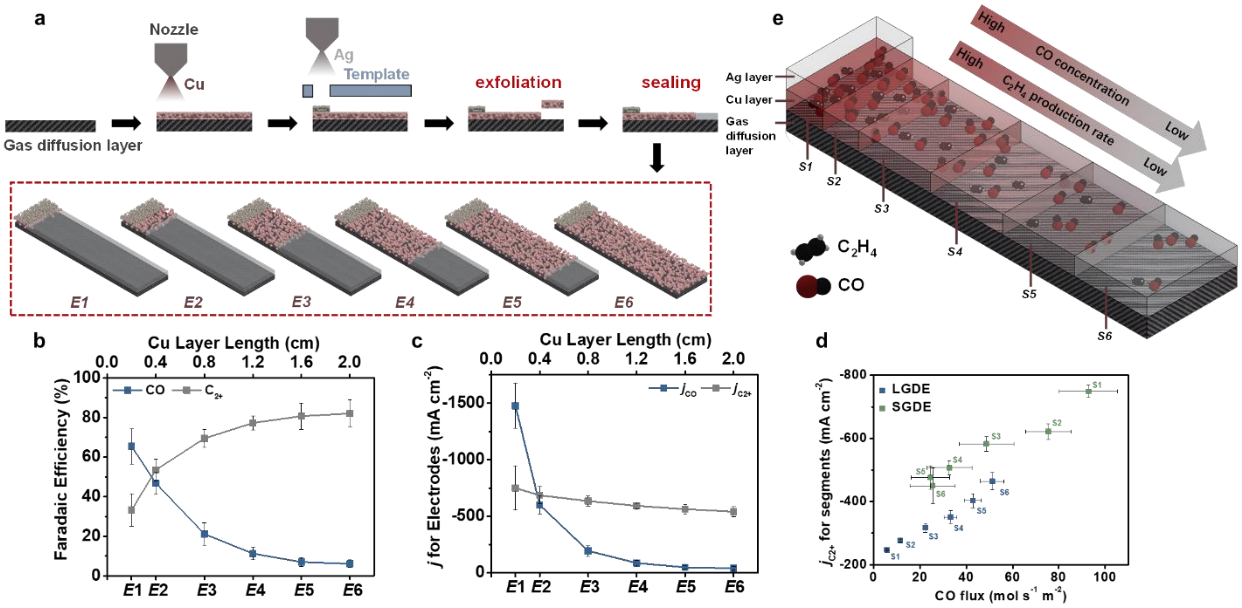

Figure 2. Track the interplay between CO flux and C-C coupling reaction kinetics. (a) Schematic of preparation process for segmented gas diffusion electrodes. (b-c) FEs and partial current densities of CO and C_{2+} in each segmented gas diffusion electrodes with partial to full Cu catalyst layer. (d) Partial current densities of C_{2+} in sub-segment as schemed in (e).

The CO_2 reduction performance of these six electrodes (E1 to E6) was evaluated in a customized membrane electrode assembly (MEA) electrolyzer. The iR-corrected cathode potential was calculated by subtracting the measured anode potential from the applied cell voltage. As expected, plotting the CO_2 reduction performance versus the length of the Cu CL segment implies a nonlinear correlation. Specifically, from E1 to E6, the FE of CO gradually declines from 65.5%

to 6.2% at -0.70 V vs. RHE by extending the Cu CL length from 0.20 to 2.00 cm, while the overall FE of C_{2+} products progressively rises from 33.2% to 82.0% (**Figure 2b**). The rise of the overall FE of C_{2+} products from E1 to E6 is acrscribed to the increase of CO conversion. However, the gradients of both FEs of CO and C_{2+} products decline as the Cu CL length extends. The FEs of specific C_{2+} products, such as C_2H_4, C_2H_5OH, and CH_3COO^-, showed a similar Cu CL length-dependent behavior to the overall FE of C_{2+} products. In contrast, the partial current density of C_{2+} products (j_{C2+}) monotonically drops from -750 mA cm^{-2} to -540 mA cm^{-2} with increasing Cu CL segment length. The gradient of j_{C2+} between two electrodes decreases as the Cu CL segment length increases (**Figure 2c**). The electrochemical active surface area (ECSA) analysis illustrates a linear relationship between the capacity and the Cu CL length, excluding the effect of ECSA variation on the CO_2 reduction performance. Since the production rate of C_{2+} products declines synchronously with the consumption of CO concentration, we suggest that the variation in j_{C2+} on different electrodes is governed by the change in CO concentration along the y-axis (electrode length).

To gain a clear insight into the relationship between CO flux and C_{2+} productivity within the tandem electrode, we conducted a detailed analysis of j_{C2+} and CO flux for each sub-segment. The increment of the sub-segment order number (S1, S2, … S6) represents the direction from the inlet to the outlet It's important to note that, due to computational limitations, the CO flux represents the outlet flux for each sub-segment (for instance, the CO flux of S1 represents the conditions at the interface between S1 and S2). The results presented in **Figure 2d** support our hypothesis that the instantaneous C_{2+} production rate in different regions of the electrode is closely linked to the real-time CO concentration in the local gas environment. This finding provides an explanation for the non-linear relationship observed in CO_2 reduction performance as a function of CL length. Notably, each sub-segment in the SGDE exhibits significantly higher C_{2+} product productivity compared to the sub-segment with the same number in the LGDE (**Figure 2d**). The improvement of productivity of C_{2+} products is magnified especially in the first four sub-segments (S1-S4). A comparison in **Figure 2d** unequivocally demonstrates the superior C-C coupling reaction kinetics of the SGDE compared to the LGDE.

Figure 2e intuitively depicts the spatial profile of CO flux and C_{2+} productivity for the SGDE. It is noteworthy that while there is likely a large amount of CO generated in the Cu CL, it appears that the trends in j_{C2+} are largely driven by the residence time of the *in-situ* generated CO. Placing the CO-selective catalyst at the inlet of the SGDE leverages the along-the-channel transport within the MEA to distribute and subsequently further reduce the entrance CO from the Ag. However, for the layered GDE, the *in-situ* generated CO can easier exit the Cu CL prior to conversion.

B.3.2. Assess the effect of Cu:Ag area ratio on the performance of SGDEs

To further assess the impact of the spatial management of CO concentration on the rate of C_{2+} production within SGDEs, five different stacked Cu/Ag SGDEs with varying ratios of Cu and Ag CL areas were prepared and tested. The area of the Cu CL was held at 1.00 cm^2, while the Ag CL had the same width, but its length was varied from 0.10 cm to 2.00 cm (*i.e.*, its area varied from 0.05 to 1.00 cm^2) (**Figure 3a-b**). These SGDEs are denoted as Cu/Ag (x:y) SGDE, where x and y represent the area of the Cu and Ag CLs, respectively. A pure Cu GDE was also prepared for comparison. Because the Ag mass is kept constant for all Ag CL areas, the thickness of the Ag CL segment grows as its area shrinks. **Figure 3c and d** show the cross-sectional SEM and EDS of the two CLs overlapping section in the Cu/Ag (1.00:0.05) SGDE, which has the thickest Ag CL in this study. The total thickness of the CL in the overlapping area is ~ 2.0 μm, including 0.5 μm for the Ag CL, which is still thin enough so as to not produce mass-transport limitations, in accordance with our previous work.

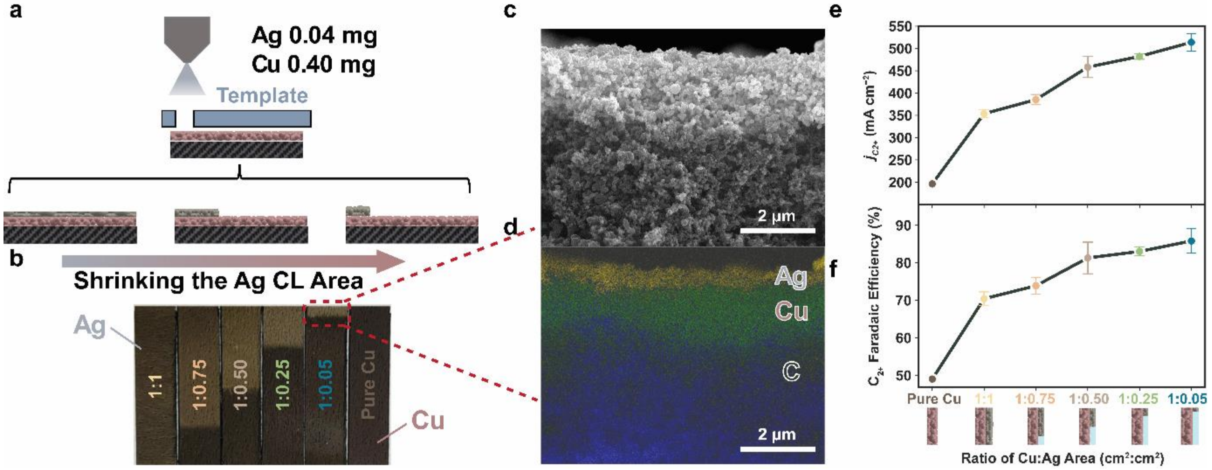

Figure 3. Effect of Cu:Ag area ratio on the performance of SGDEs for CO_2 reduction. **(a)** The schematic of the preparation procedure of five SGDEs with fixed quantities of Cu and Ag catalysts but a varied area ratio between Cu and Ag CLs. **(b)** Photos of five Cu/Ag (*x*:*y*) SGDEs and a control Cu GDE. *x* and *y* represent the area of the Cu and Ag CLs, respectively. **(c)** The cross-sectional SEM image and **(d)** EDS elemental mapping of the overlapping section in the Cu/Ag (1.00:0.05) SGDE. **(e)** The C_{2+} Faradaic efficiency and **(f)** j_{C2+} as a function of the ratio of the Cu:Ag CL areas at a constant applied cell voltage of 3.05 V. The error bars represent the standard deviation from the measurement of three independent electrodes.

As shown in **Figure 3e-f**, all SGDEs offer an improved yield of C_{2+} products compared to the Cu GDE at an equivalent applied cell voltage. For the SGDEs, both the FE of C_{2+} products (**Figure 3f**) and j_{C2+} (**Figure 3e**) rise gradually as the Ag CL area shrinks from 1.00 cm^2 to 0.05 cm^2. The Cu/Ag (1.00:0.05) SGDE exhibits the highest C_{2+} FE and j_{C2+} because it produces the highest concentration of CO and in accordance with the results shown in **Figure 2**, achieves the highest CO utilization. The Cu/Ag (1.00:0.05) SGDE achieves a maximum FE of C_{2+} of 86.1% and j_{C2+} of 560 mA cm^{-2} at a cell voltage of 3.20 V. The cell voltage reported here is IR compensated unless otherwise stated. These values correspond to a 1.7× increase in C_{2+} FE and a 2.7× increase in j_{C2+} compared to a pure Cu GDE at the same applied cell voltage. Notably, all SGDEs exhibit lower FE and partial current density of CO than the Cu GDE, which translates to a greater CO utilization. Furthermore, the average residence time of the CO increases as the ratio of Cu/Ag area is increased. This increase in the CO utilization and residence time for the SGDE when compared to the Cu GDE implies that the increased θ_{*CO} not only allows for greater conversion of the *in-situ* generated CO, but also enables increased conversion of the Cu-generated *CO intermediates by mass action.

B.3.3. Multiphysics model of mass transport and CO adsorption in an SGDE

A 2D continuum model of the cathodic chamber of the cell was developed to rationalize and guide the results and design, respectively. The Langmuir adsorption model was implemented in a multiphysics simulation of gas-phase CO and CO_2 transport within the SGDE and flow channel (shown schematically in **Figure 4a**) to estimate the local θ_{*CO} in experimentally tested SGDEs. It is important to note that the simulation assumes the SGDE behaves as a perfect tandem. In other words, all C_{2+} products are derived from CO generated over Ag, as opposed to the direct reduction of CO_2 on Cu. While indeed a simplification, this assumption is relatively consistent with the results shown in **Figure 2**, which suggest that the trends in j_{C2+} are largely driven by the consumption of *in-situ* generated CO.

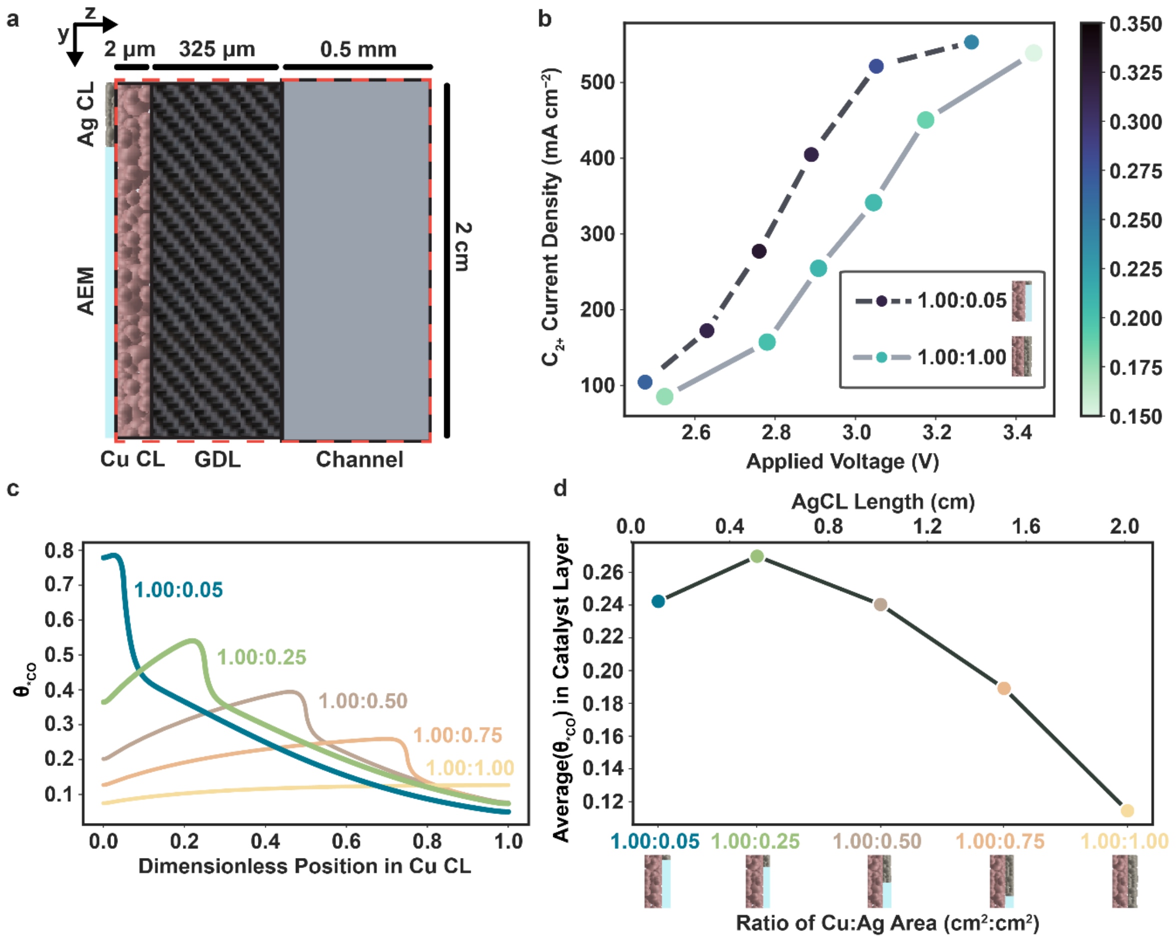

Figure 4. Multiphysics model of mass transport and CO adsorption in an SGDE. (a) Schematic of the modeled domain (red dotted box). **(b)** Polarization curves for the Cu/Ag (1.00 : 0.05) SGDE and (1.00 : 1.00) SGDE. The color of the marker represents the average *CO surface coverage attained in the Cu CL for a given Cu/Ag area ratio, voltage, and C_{2+} current density. **(c)** Simulated profiles of local θ_{*CO} in the Cu CL for all five Cu/Ag area ratios studied experimentally at a C_{2+} current density of 550 mA cm^{-2}. **(d)** Average local θ_{*CO} in the Cu CL versus Cu/Ag area ratio at a C_{2+} current density of 550 mA cm^{-2}.

As shown in **Figure 4b**, moving from an LGDE (Cu/Ag 1.00:1.00) to an SGDE with a highly concentrated Ag layer (Cu/Ag 1.00:0.05) significantly increases the average value of θ_{*CO}

achieved within the catalyst layer. This phenomenon can be explained as follows. As the Cu:Ag area ratio increases, the formation of CO in the Ag CL occurs in a concentrated end, thereby raising the local concentration of CO, resulting in an increased θ_{*CO} locally near the Ag/Cu boundary that decays along the length of the Cu CL as CO is consumed to form C_{2+}. This change in θ_{*CO} profile with increasing Cu/Ag area ratio is reflected in the simulations shown in **Figure 4c** and is consistent with above results. **Figure 4d** shows the average θ_{*CO} achieved in the CL as a function of the Cu/Ag area ratio at constant j_{C2+}, demonstrating that for the same j_{C2+}, the average θ_{*CO} in the Cu CL increases as the length of the Ag layer shrinks. This increase in the average θ_{*CO} enhances j_{C2+} by mass action and corresponds to a decrease in the required overpotential to achieve the identical C_{2+} current density. The simulations provide significant evidence for the hypothesis that a higher average θ_{*CO} is achieved in SGDEs.

B.3.4. Performance of SGDE with different CO-selective catalysts

CO-selective catalysts, such as Ag, ZnO, and emerging single-atom catalysts (*e.g.*, iron-nitrogen-carbon (Fe-N-C) nanostructure), exhibit dramatically different performance for CO evolution at a given applied voltage. The effectiveness of the SGDE requires compatible overpotentials to produce CO in the CO-selective CL and subsequently dimerize that CO in the Cu CL. To determine the optimal catalyst pairing, we compared SGDE performance for three CO-selective catalysts: Ag, ZnO, and Fe-N-C. The Fe-N-C was home-made. For a fair comparison, the catalyst quantities, electrode structure, and segment dimensions were maintained the same for all SGDEs. The optimal cell voltage for the production of C_{2+} products decreases as the productivity of CO increases from ZnO to Ag and further to Fe-N-C (**Figure 5a**). Therefore, the Cu and Fe-N-C represent the most efficient combination at the range of low cell voltage. The Cu/Fe-N-C SGDE achieves a maximum C_{2+} FE of 87.0% and j_{C2+} of -437 mA cm^{-2} at 2.89 V (**Figure 5a)**. The FE of C_2H_4 accounts for 47.0% at this cell voltage. Consequently, the full cell energy efficiency is 18.0%, which takes into account the cell internal resistance loss. The Cu/Fe-N-C SGDE demonstrates a half-cell energy efficiency of over 33.0% for C_2H_4 production.

Seeking to achieve higher C_2H_4 and C_{2+} productivity on the Cu/Fe-N-C SGDE, both Cu and Fe-N-C loadings were doubled but still keeping the Cu loading at a reasonable value of 0.8 mg cm^{-2}. To mitigate flooding at a current density of over 1,000 mA cm^{-2}, the test of Cu/Fe-N-C SGDE was transferred to a flow cell equipped with a thin buffer layer (2 mm) at the cathodic compartment. After doubling the loading, the Cu/Fe-N-C SGDE boosts the j_{C2+} to -1072 mA cm^{-2} with a C_{2+} FE of 89.0% at 3.38 V (cathodic potential of -0.65 V) (**Figure 5b and c**). The FE of C_{2+} products and j_{C2+} for Cu/Fe-N-C SGDE reach 1.2 times and 1.8 times, respectively, compared to those for Cu GDE tested in the flow cell under identical conditions. Moreover, the maximum FE of C_2H_4 rises to 63.5% at j_{C2H4} of -762 mA cm^{-2}. The half-cell energy efficiency of C_2H_4 in the flow cell achieves 40.0%, while the full cell energy efficiency decreases to 16.9% due to the increase of cell internal resistance.

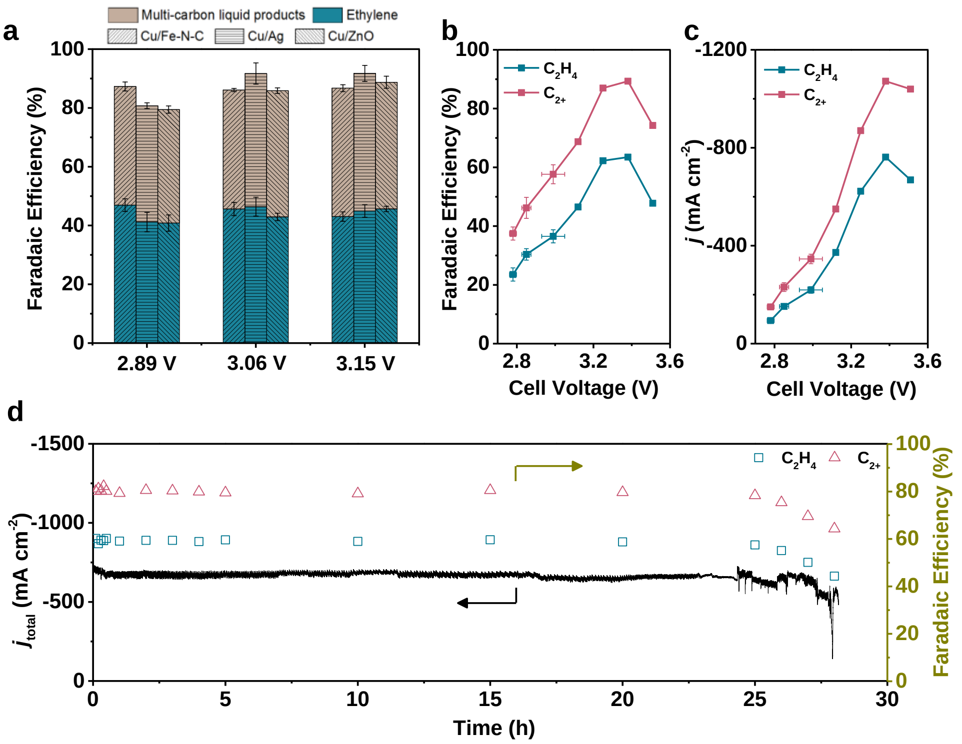

Figure 5. The compatibility between Cu and CO-selective catalysts. (a) The Faradaic efficiency of C_2H_4 and C_{2+} liquid products under three cell voltages for Cu/Fe-N-C, Cu/Ag, and Cu/ZnO SGDEs. The Cu/Fe-N-C, Cu/Ag, and Cu/ZnO SGDEs achieve their optimal C_2H_4 Faradaic efficiency on 2.89, 3.06, and 3.15 V, respectively. **(b)** The Faradaic efficiency and **(c)** partial current densities of C_2H_4 and C_{2+} products as a function of cell voltage on Cu/Fe-N-C SGDE. The test was conducted in a flow cell with a thin buffer layer of 2 mm. **(d)** The long-term stability of Cu/Fe-N-C SGDE operated in a thin-buffer flow cell at 4.6 V. The error bars represent the standard deviation from measurements of at least three independent electrodes.

B.3.5. Stability of gas diffusion electrodes for CO_2 and CO reduction

We carried out a systematic study on the stability of GDE for CO_2RR/CORR, We found the significant role of GDL in water management and revealed the water transport mechanism in porous GDE during CO_2RR/CORR using *In-situ* optical microscope and *ex-situ* micro-computed tomography (micro-CT) techniches. To accelerate the assessment of the water management ability of GDL, the CORR was used as a probe reaction instead of the CO_2RR owing to the lower solubility of CO (0.99 mM at 20 ^{o}C) and thus the higher sensitivity of CORR performance to flooding.

Identification of the origin of sluggish CO transport. The GDEs were prepared based on the commercial GDL (SGL Sigracet 39BB) containing 5 wt% PTFE. The CL had a PTFE content of 33.3 wt% with respect to the Cu catalyst loading (denoted as SGL-Cu-PTFE-33). When a fresh SGL-Cu-PTFE-33 GDE was used for 10 min testing for each applied potential, the SGL-Cu-PTFE-33 exhibited remarkable CO reduction performance. Specifically, the fresh SGL-Cu-PTFE-33 delivered close to unity C_{2+} Faradaic efficiency (FE) and a partial current density of C_{2+} (j_{C2+}) of 600 mA cm^{-2} at -0.60 V vs. RHE (**Figures 6a and b**). The FE of C_{2+} declined to 75%, while j_{C2+}

further increased to 1100 mA cm^{-2} at -0.84 V vs. RHE. This short-term performance rivals most of the peer-reported performances. However, during the long-term CORR at a constant total current density (j_{total}), e.g., 400 mA cm^{-2}, the FE of C_{2+} degraded from 80% to 16% within 90 minutes, accompanied by a cathodic shift of potential from -0.60 to -0.85 V vs. RHE (**Figures 6c and d**). As expected, the FE of H_2 rapidly increased from 10% at 10 min to 60% at 90 min. After disassembling the electrolyzer, a significant amount of water was observed in the flow channel. The water comes from the catholyte penetration into the GDE, indicating severe GDE flooding. We hypothesized that CORR performance declines due to sluggish CO transport in the flooded GDE. The increased cathodic shift of potential is due to the mass transport overpotential seen in flooded systems.

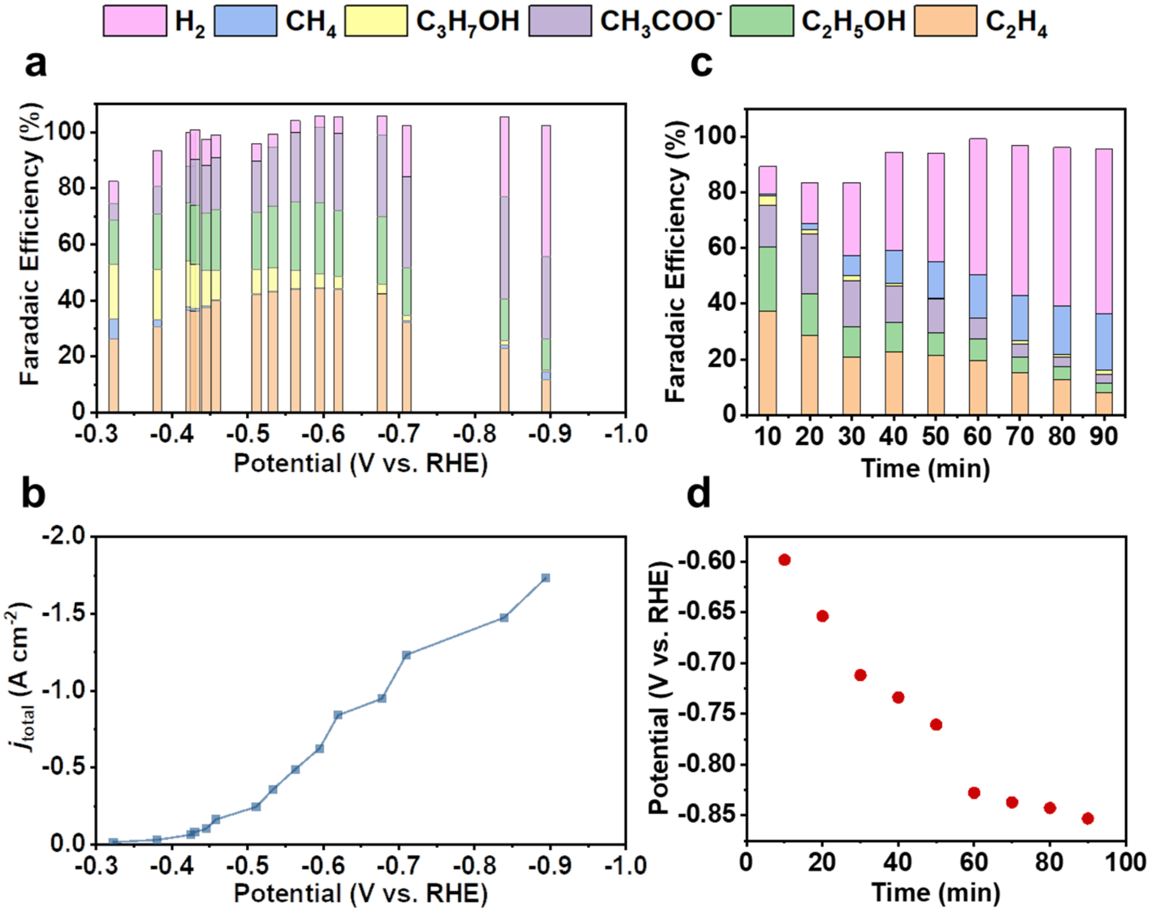

Figure 6. (a) The Faradaic efficiency of all CO reduction products and (b) the total current density versus the potential for SGL-Cu-PTFE-33 when a fresh GDE is operated for a short period of 10 min at each applied potential. The test was conducted in a flow cell with 1 M KOH as a catholyte. (c) The Faradaic efficiency of all CO reduction products and (d) the corresponding cathode potential as a function of operation time on the SGL-Cu-PTFE-33. The test was conducted in a flow cell with 1 M KOH catholyte at a constant total current density of 400 mA cm^{-2}.

To mitigate flooding in the CL, we sought to prepare GDEs with a higher PTFE content in the CL, which increases the CL hydrophobicity. However, increasing PTFE content cannot ease the degradation of FE of CORR. The spent GDE maintained a water contact angle of 125^{o}, suggesting that the CL preserved considerable hydrophobicity after 90-minute CORR. The degradation of CORR performance was caused by flooding of GDL. Therefore, a more hydrophobic GDL (Toray-090) with a higher PTFE content (30 wt%) was used to prepare the fourth GDE (denoted as Toray-Cu-PTFE-66). The stability of CORR performance was relatively improved for Toray-Cu-PTFE-66, as revealed by the relatively constant FE of C_{2+} in the first 60 min. However, the FE of C_{2+} still gradually declined to 57% at 90 minutes. Compared with the CL, an increase in hydrophobicity of the GDL exhibits a more pronounced improvement in durability.

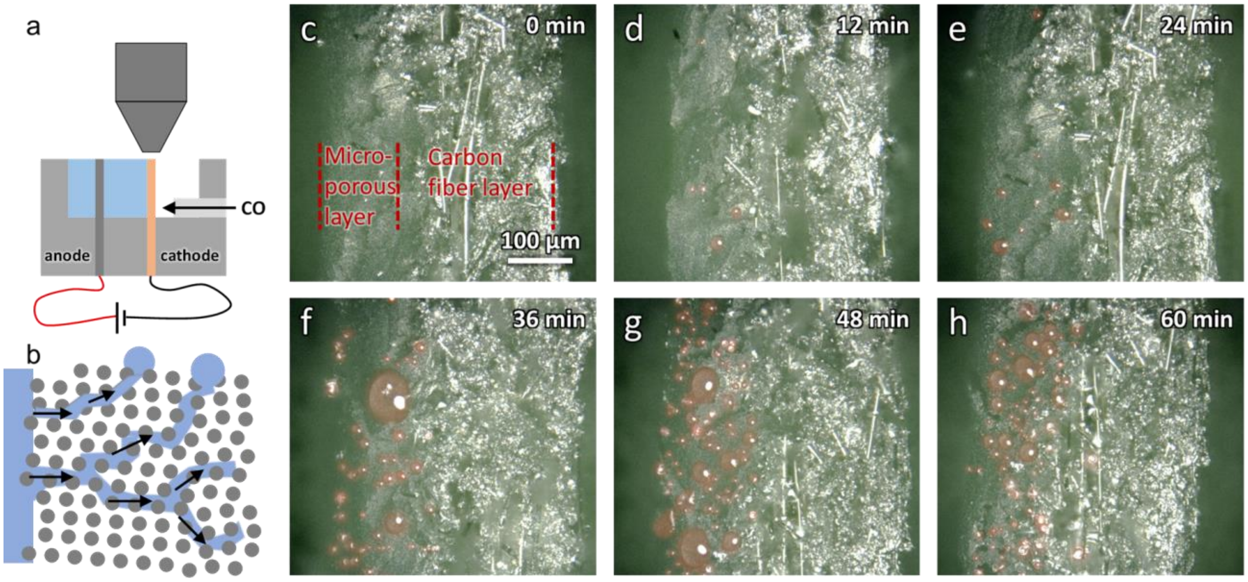

Figure 7. (a) Schematic of *in-situ* optical microscope characterization of the GDE. (b) Schematic of the predicted fingering-type water flow pattern in the GDL. (c-h) The optical microscope images of droplets distribution along the thickness direction of the GDL/Cu/PDMS-20 electrode at different reaction periods.

In-situ and ex-situ characterization of water transport in GDL. To understand the water flow scenario in the GDL, *in-situ* characterization was conducted to monitor the water percolation in GDL during CORR. As shown in **Figure 7a**, we designed a particular electrolyzer with an open-top so that the cross-sectional area of GDE is exposed. CO gas stream was fed to the electrolyzer to create a comparable environment to the flow cell. An optical microscope with 500× magnification was placed right above the cathode electrode during electrolysis. To visulize the water transort in the GDL, we designed a CL-free GDE prepared by electrodepositing Cu cubic particles into GDL. To increase the hydrophobicity, the microporous layer (MPL) of GDE was further coated with PDMS in a content of 20 wt% (denoted as GDL/Cu/PDMS-20). For the CL-free GDE, the GDL maintained an almost dry condition with sparse droplets scattered on the cross-sectional area during the first 30 min (**Figure 7c-e**), agreeing with the relatively constant CO reduction activity within the first 30 min. After that, the number of droplets increased, accompanied by the appearance of some large droplets (**Figure 7f-h**). The droplet size was proportional to the quantity of the water flow in the GDL. Note that the water contact angle on the cross-sectional area was visually large, illustrating a good hydrophobicity of the MPL. Referring to the existing mechanism of liquid transport through the GDL, the randomly scattered droplets across the cross-sectional area support the fingering-type flow, which spreads across the network (**Figure 7b**). In contrast, the water flooding in GDL/Cu without PDMS coating resembles stable displacement, where liquid flow occupies most of the pores and displaces the gas. The difference in liquid transport mechanisms inside the pores arises from different inner hydrophobicity.

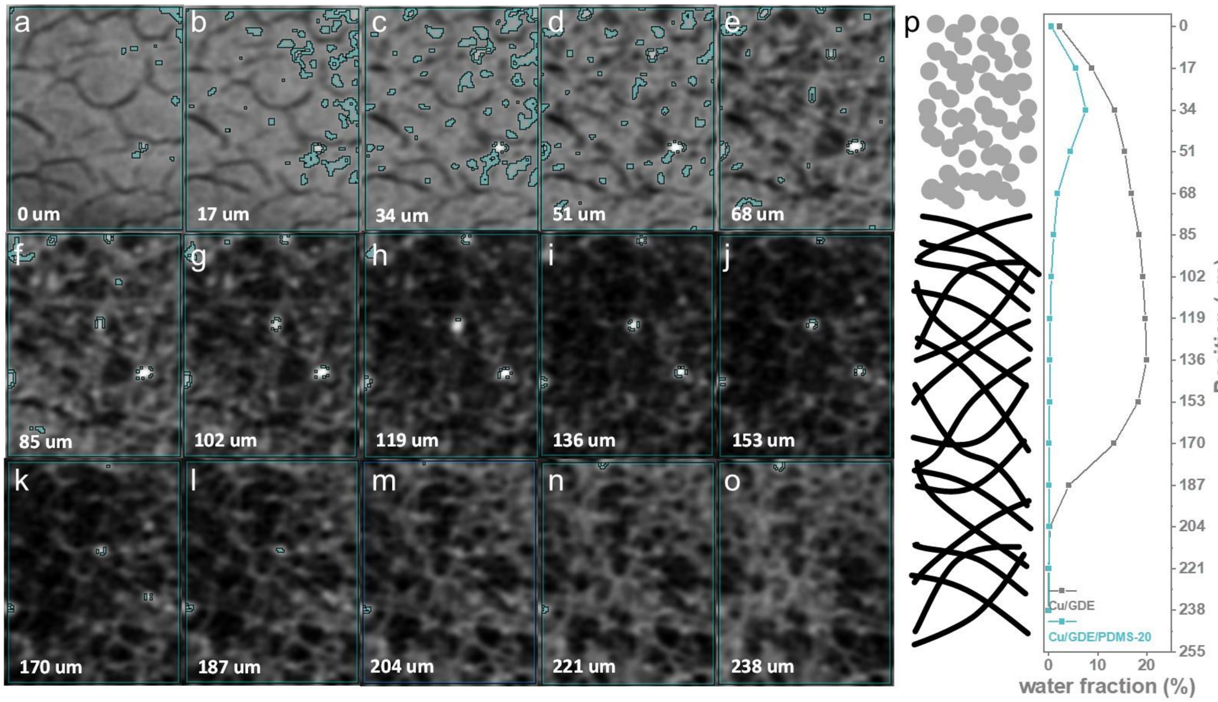

Figure 8. (a-o) Micro-CT images of the GDL/Cu/PDMS-20 taken layer by layer down the thickness (vertical) direction in 17 μm interval. The area marked by cyan color corresponds to the Hounsfield unit value ranging from -50 to 50, representing water distribution. 0 μm represents the front surface (MPL) facing the electrolyte side, while 238 μm is the back surface (carbon fiber layer) facing the flow channel. (p) The water fraction over each different slice across the thickness of GDL/Cu (grey) and GDL/Cu/PDMS-20 (cyan).

To capture the water distribution inside the GDL pores, micro-CT was performed as a non-destructive, *ex-situ* characterization tool. The spent GDL/Cu and GDL/Cu/PDMS-20 were sealed immediately after the one-hour CORR to prevent water evaporation. A fresh GDL was also characterized as the benchmark. The micro-CT imaged the electrode in the thickness direction slice by slice with 17 μm resolution. The area with Hounsfield unit value ranging from -50 to 50 was identified as water. The visualization of water distribution in each slice of the GDL/Cu/PDMS-20 electrode is displayed in **Figures 8a-o**. Water is scattered randomly, resembling the fingering flow revealed by *in-situ* optical microscope characterization. The water fraction in each slice was calculated by counting the pixel of the water area over the entire imaging area. Note that each pixel point in the images represents the average value in a cubic volume of 17 × 17 × 17 μm^3. For the spent GDL/Cu/PDMS-20, water mainly stays in the MPL within the top 68 μm thickness, while the rest of the GDL remains unwetted (**Figure 8p**). The slice of 34 μm contains 7.5% water out of the image area, corresponding to 24% of the pores occupied by water when taking the MPL porosity into consideration. However, the dry pores cannot guarantee efficient gas transport because some gas may be trapped by the looping water flow pathway. Therefore, the actual volume blocked by water should be more than 24%. The spent GDL/Cu exhibits a much higher water fraction (10% to 20% per image area) for each slice than GDL/Cu/PDMS-20 except for the last two slices adjacent to the gas flow channel. Moreover, the maximum occupation of the pores by water reaches 40%. The higher water fraction translates to more sluggish CO transport, which is detrimental to the activity toward CORR.

According to the experimental observations, increasing the GDL and CL hydrophobicity can alter the water flow pattern inside the GDE, but it cannot prevent the GDE from flooding. The conventional GDE structure has shown excellent stability in other reactions like water electrolysis and fuel cell. However, the electrochemical CO_2 or CO reduction possesses more sophisticated reaction scenarios. First, the electrochemical CO_2 or CO reduction involves reactants in both gas and liquid phases, rather than the simple liquid phase reactant in water electrolysis. Thus, the GDE must compromise the activity of gas and liquid phase reactants in the CL to ensure sufficient reaction kinetics. Second, the electrochemical CO or CO_2 reduction involves electrolytes in various concentrations rather than pure water in the fuel cell. Hence, electro-osmosis will speed up the flooding and thereby restrict gas availability. The conventional GDE structure is intrinsically prone to flooding, resulting in poor stability of CORR and CO_2RR. Future research on solving flooding should focus on changing the reaction conditions to neutral electrolytes like pure water or transforming the structure of GDE.

B.3.6. Development of Catalysts for Selective C_2H_4 Formation

The tandem electrodes can boost C-C coupling and thus enhance the overall C_{2+} selectivity and productivity. However, tandem electrodes cannot control the selectivity toward a single C_2 product (e.g., C_2H_4 or C_2H_5OH) following the C-C coupling stage. To further increase the selectivity of C_2H_4, UC developed single-site doped Cu catalysts to direct the post-C-C coupling pathway.

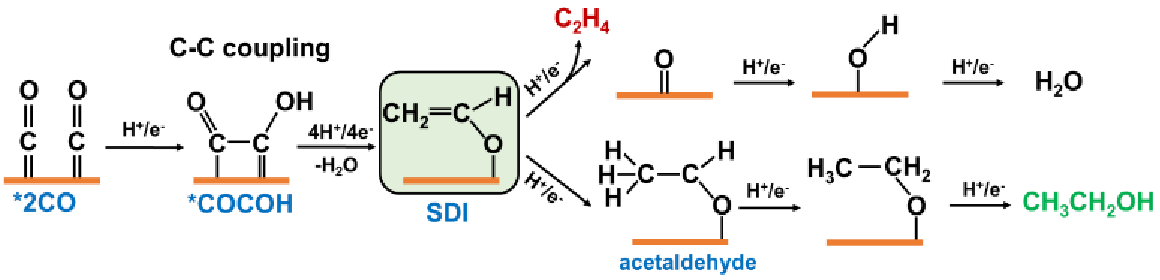

Figure 9. One potential raction pathway invovling CH_2CHO* as the selectity determining intermediate from which the bifurcation of product into C_2H_4 and C_2H_5OH starts.

Probing the selectivity-determining intermediate (SDI) that bifurcates the reaction pathway toward either C_2H_4 or C_2H_5OH is the pre-requite for the rational design of post-C-C coupling catalysts. The strategy to adjust various catalyst surface properties depends on the SDI chemical structure and adsorption. Prior computational results suggest that the O-bound species (CH_2CHO*) is a plausible SDI, from which the formation of C_2H_4 and C_2H_5OH diverges (**Figure 9**). The hydrogenolysis of CH_2CHO* (C-O cleavage) leads to C_2H_4, whereas the hydrogenation of α carbon in CH_2CHO* gives rise to acetaldehyde (CH_3CHO*) and consequently to C_2H_5OH. It is worth noting that an O*-adsorbate would undergo two reduction steps leading to H_2O formation after C_2H_4 is released from the catalyst surface. Thereby, the stabilization of O* species after C-O cleavage is an effective descriptor that measures the potential bifurcation of SDI to C_2H_4. In addition, according to the scaling relations between adsorption energies, the O* binding strength of the catalyst has a significant effect on the adsorption configurations and energetics of O-bound intermediates (e.g., CH_2CHO*) and resultant product selectivity. We aim to utilize the single site dopant to tune the oxygen affinity of Cu surface. Various noble metal single site doped Cu catalysts (M-Cu, M = Rh, Ir, Ru, Pd, Ag, and Au) were synthesized by cation exchange methode. As an example, **Figure 10** shows the structural characterization of Rh-Cu catalysts (Rh content 1 at.%). A spectrum of spectrocopy and electron microscopy characterization clearly elucidate that Rh dopants are atomically dispersed on metallic Cu in Rh-Cu catalyst. Other M-Cu catalysts possess a similar M single site feature.

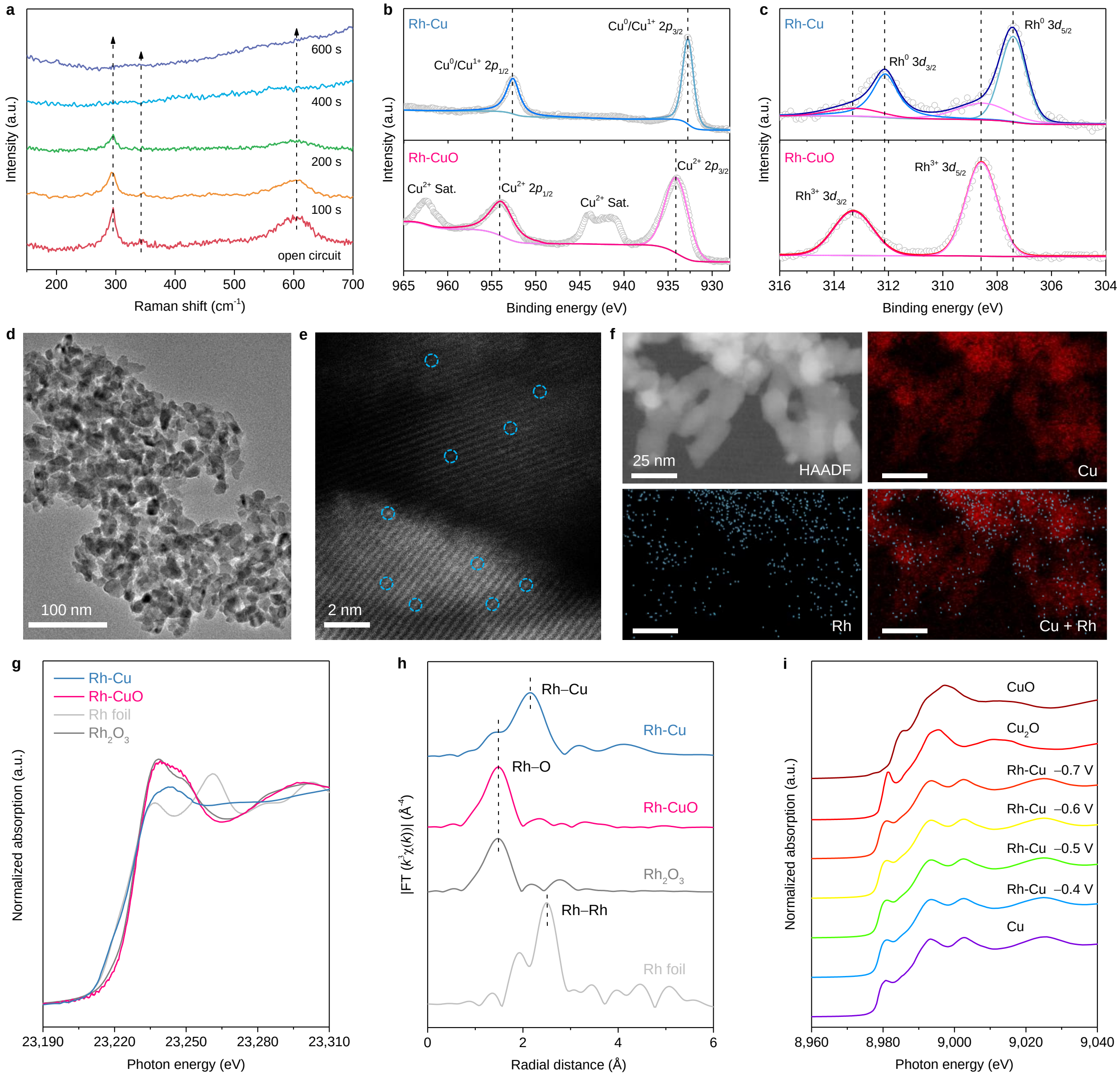

Figure 10. Structural characterization. a, In situ Raman spectrum of Rh-CuO at –0.35 V under CO_2RR, the pre-reduction process of Rh-CuO turning into Rh-Cu. **b,c,** Cu 2*p* XPS spectrum (**b**) and Rh 3*d* XPS spectrum (**c**) of Rh-CuO precursor and Rh-Cu catalyst. **d,** TEM image of Rh-Cu catalyst. **e,** HAADF-STEM image of Rh-Cu catalyst. The blue circles highlight Rh atoms. **f,**

STEM-EDS mapping of Rh-Cu catalyst, showing atomic dispersion of Rh sites on the Cu matrix. **g,h,** Ex situ XANES spectrum (**g**) and EXAFS spectrum (**h**) at the Rh K-edge of Rh-CuO precursor and Rh-Cu catalyst. The spectrum of Rh foil and Rh_2O_3 are shown as references. **i,** In situ XAS spectrum at the Cu K-edge of Rh-Cu under CO_2RR, along with the spectrum of Cu, Cu_2O and CuO as references.

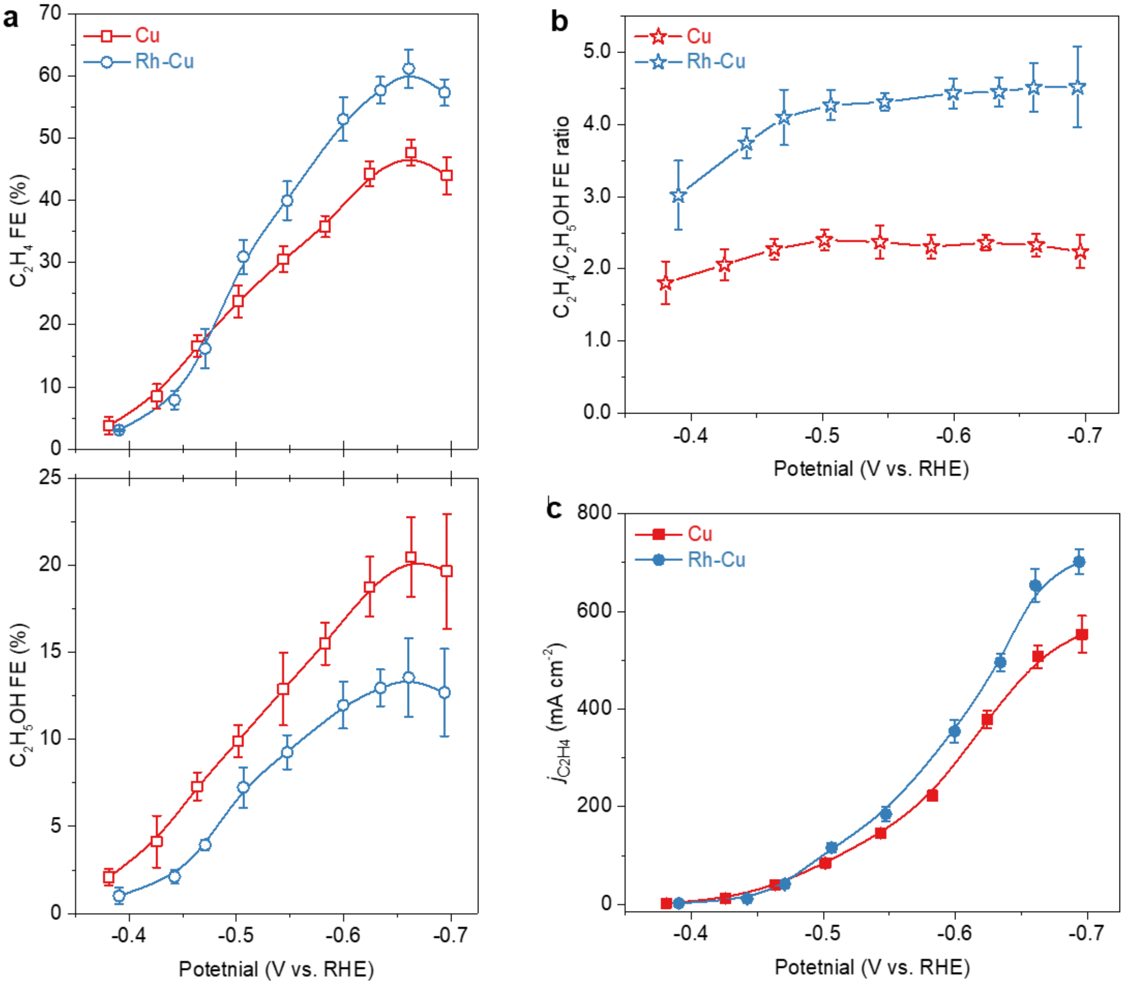

Figure 11. Electrocatalytic CO_2RR performance of M-Cu catalysts. a, Comparison of C_2H_4, C_2H_5OH and C_{2+} products FEs, and C_2H_4/C_2H_5OH FE ratios on M-Cu catalysts at –0.65 ± 0.01 V. **b-d,** Comparison of C_2H_4 and C_2H_5OH FEs (**b**), C_2H_4/C_2H_5OH FE ratios (**c**), and $j_{C_2H_4}$ (**d**) on the Rh-Cu and pristine Cu catalysts at different overpotentials. The error bars represent standard deviations from measurements of three independent electrodes.

Among all M-Cu catalysts, Rh-Cu catalyst exhibits the highest selectivity to C_2H_4 while Au-Cu catalyst shows the highest C_2H_5OH FE. Rh-Cu catalyst exhibited superior C_2H_4 selective at the expense of C_2H_5OH formation at potentials more negative than −0.48 V (**Fig. 11a**), leading to a promoted C_2H_4/C_2H5OH FE ratio of ~4.50 across the potential range of −0.48 to −0.70 V (**Fig. 11b**). As a control, pristine Cu shows a C_2H_4/C_2H_5OH FE ratio of 2.33. Rh-Cu reached a peak C_2H_4 FE of 61.2% with partial current density ($j_{C_2H_4}$) of 653 mA cm^{-2} at −0.66 V. As a comparison, pristine Cu yielded C_2H_4 FE of 47.7% and $j_{C_2H_4}$ of 507 mA cm^{-2} at the same overpotential (**Fig. 11a and c**). We investigated the possible influence of electrochemical surface area (ECSA), which was determined by the double-layer capacitance method. The ECSAs for M-Cu catalysts were nearly invariant, indicating the surface roughness is not the main factor contributing to performance change. The normalized partial current densities of C_2H_4 and C_2H_5OH still followed the same orders as geometric ones.

We studied the SGDE performance by incorporating Rh-Cu catalysts. We adopted a co-planar segmented electrode design by combining Rh-Cu catalyst with homemade ZnO nanoparticles (ZnO/Rh-Cu SGDE). The ZnO catalyst, serving as an extra CO supplier, was placed at the inlet segment of catalyst layer to prolong CO residence time along the length of the electrode (**Fig. 12a**). In this way, SGDE efficiently intensifies *CO surface coverage at the Rh-Cu surface to enhance the reaction kinetics of the C–C coupling step and in turn maximize CO_2-to-C_{2+} conversion. The ZnO/Rh-Cu SGDE reached the C_{2+} FE of 85.4% and C_2H_4 FE of ~70% at 3.7 V (**Fig. 12b**), corresponding to a C_2H_4 EE_{full} of 22%. Concurrently, partial current densities of C_2H_4 and C_{2+} products were boosted to 1,012 and 1,256 mA cm^{-2}, respectively (**Fig. 12b**). Hereby, we demonstrated the collective control of rate-determining and selectivity-determining steps, i.e., initial and post C–C coupling steps, to direct CO_2 conversion to a specific C_2 product (e.g., C_2H_4) at high selectivity and productivity based on both catalyst and electrode designs.

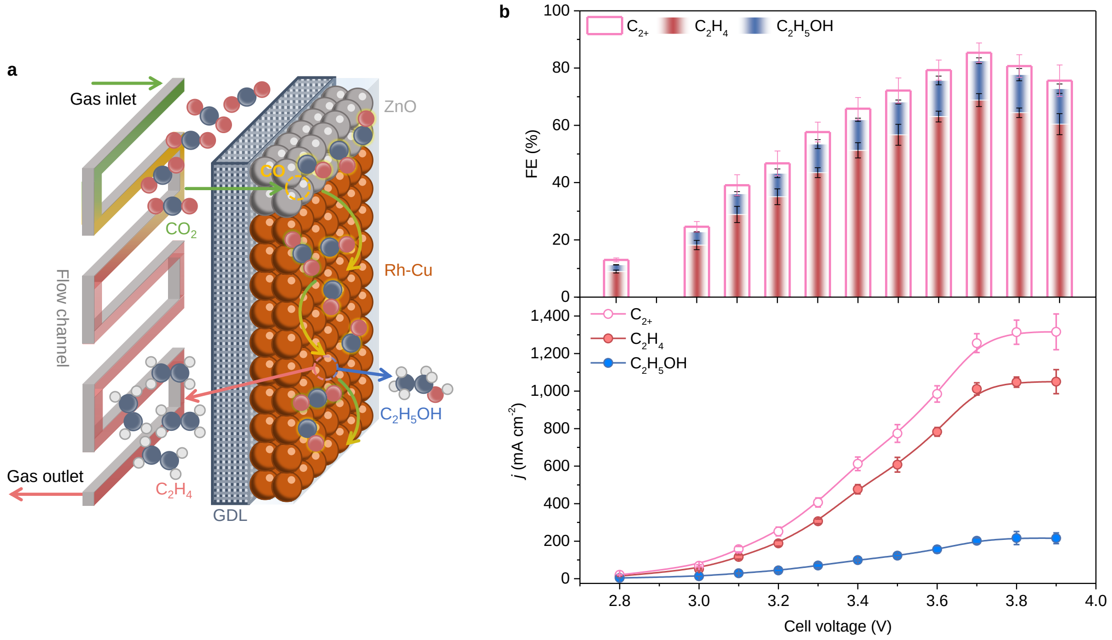

Figure 12. CO_2RR performance of the ZnO/Rh-Cu SGDE in an MEA cell. a, Schematic illustration of the tandem electrode structure. **b,** FEs and partial current densities of C_2H_4, C_2H_5OH and C_{2+} products at different applied cell voltages. Ni foam was used as the anode.

B.4. Summary

Segmented tandem electrodes. We designed a simple yet efficient SGDE in which a short, heavily loaded CO-selective CL segment placed at the inlet of the SGDE prolongs the residence time of generated CO in the subsequent Cu CL segment where C-C coupling takes place. By optimizing the relative lengths and loadings of Cu and Ag in a Cu/Ag SGDE, we maximized the residence time of CO in the Cu CL segment to facilitate a 300% increase in CO utilization compared to a non-segmented Cu/Ag GDE. Moreover, we found that a 250% increase in j_{C2+} relative to pure Cu could be achieved using an optimized Cu:Ag area ratio of 1.00:0.05. A 2D-continuum model verified the effects of CL area ratios, residence time, and feed flow rate on the θ_{CO^*} on the observed enhancements in j_{C2+}. Lastly, using the SGDE design and a Cu/Fe-N-C tandem CL, 90% FE to C_{2+} products at a j_{C2+} exceeding 1 A cm^{-2} and a half-cell energy efficiency for CO_2-to-C_2H_4 conversion of 40.1% was achieved. The SGDE architecture employed in the present study presents unique opportunities for application in industrial systems for CO_2 electrolysis. Aside from the achievement of high C_{2+} current densities and FEs with a relatively low loading of Ag, the present study leverages along-the-channel gradients to enhance CO utilization in a tandem catalyst. These downstream concentration gradients will be more pronounced in industrial systems that employ larger electrodes for CO_2 reduction at scale. Therefore, it can be imagined that the developed SGDE scheme would be even more effective at-scale, and future studies should aim to examine the performance of these SGDEs within industrial scale electrolyzers and cell sizes and distinct flow channel architectures to enhance the readiness of the emerging technology.

Advanced C_2H_4-selective catalysts. We demonstrated that single-site doping is an efficient strategy to modulate the Cu surface oxygen affinity. Our research reveals that the oxygen binding energy of the catalyst surface serves as a generalized descriptor, enabling the prediction of whether the post-C–C coupling pathway leans toward producing C_2H_4 or C_2H_5OH. The oxygen affinity of the dopant on the Cu surface has a decisive influence on the feasibility of C–O bond dissociation in the SDI. Strong oxygen binding sites, such as Rh, promote C_2H_4 formation by facilitating the C–O bond scission. Rh-Cu reached a peak C_2H_4 FE of 61.2% with partial current density (j_{C2H4}) of 653 mA cm^{-2} at −0.66 V. The Cu SGDE with Rh-Cu catalysts promotes C_2H_4 generation with FE of ~70% and partial current densities > 1,000 mA cm^{-2} at 3.7 V.

Stability of gas diffusion electrode. GDE experiences fast CORR selectivity degradation due to water flooding during electrochemical reactions. The water management in GDL is more important than in CL to prevent water flooding. Simply adding more hydrophobic polymer to GDL cannot stop the decline of CORR selectivity. That is because the space wetted by water is still thick enough to cause sluggish CO transport, resulting in rapid degradation of CORR performance. Modifying the hydrophobicity of both CL and GDL only influences the water flow pattern but cannot restrain the CL flooding. The flooding may mainly come from the electroosmotic flow driven by the applied potential. The GDE that combats the flooding issue must have significant regions maintaining sustainable hydrophobicity even during electrolysis operation. A revolutionary change in the structure of GDE should be considered for the long-term stable operation of CORR and CO_2RR.

C. Task 4. Develop Pulse Electrolysis Protocol

C.1. Introduction

Oxide-derived copper catalysts show an improvement in catalytic performance towards C_2H_4 and C_2H_5OH due to the formation of active defect sites during the reduction of catalyst.[63,65] The theoretical calculations suggest that the coexistence of Cu^0 and Cu^{1+} in the defect region enhances *CO binding strength and enables favorable *CO binding configuration, together boosting the C-C coupling and enhancing the formation of C_{2+} products.[64,66] Pulse electrolysis offers the cycle of the oxidation and reduction of catalysts during the electrochemical processes. The oxidation state of copper (e.g., Cu_2O) can be formed at an anodic potential and the oxidized copper is reduced during the reduction portion. As a result of the cycle, the electrochemically active sites including grain boundaries (GBs) are formed and the catalyst morphology becomes more favorable toward C_{2+} product formations. However, the enhancement of selectivity and productivity using a pulse sequence of oxidation and reduction reactions strongly depends on the morphology of catalysts. In addition, the energy efficiency is significantly low because the oxidation process at an anodic potential requires energy but does not produce any desired CO_2 reduction products. An alternative profile to the pulse sequence of oxidation and reduction reactions is the pulse electrolysis with a combination of two different reduction potentials. Previous studies revealed that CO_2 accumulation and enhanced pH effect may enhance the formation of C_{2+} products under the pulse electrolysis with two different reduction potentials compared to potentiostatic electrolysis.[37,39,49] Generally, the main CO_2RR takes over at a more cathodic potential, and the change in the microenvironment occurs at a less cathodic potential. At the less cathodic potential, the selectivity and activity for each CO_2R product are different from the more cathodic potential, and the difference allows us to change the local reaction conditions during pulse electrolysis. Due to the less consumption of CO_2 at the less cathodic potential, the local concentration of CO_2 is increased gradually during the period. The increase of local CO_2 concentration at the less cathodic potential is called CO_2 accumulation. Then, the CO_2RR at the more cathodic potential can perform at a higher concentration of CO_2, leading to a higher yield of C_{2+} products. In addition to the CO_2 accumulation, the enhanced pH effect is accomplished during pulse electrolysis because of the difference in the consumption of OH^-. In general, the basic microenvironment favors the formation of C_{2+} products.[26,76] The rate of CO_2RR decreases at the less cathodic potential due to the lower total current density, resulting in less consumption of OH^-. This causes the gradual increase of OH^- concentration until it reaches equilibrium. As a result, upon switching to the more cathodic potential, the local pH becomes more basic than the potentiostatic condition, and the basic condition supports the C_{2+} formation at the designated potential. However, previous studies have been performed with an H-cell configuration theoretically and experimentally, thus the effect of pulse electrolysis in a flow cell relevant to industrial applications is unclear. CO_2 needs to be dissolved in the electrolyte for an H-cell to perform CO_2RR. The total current density in H-cell is low (~10 mA cm^{-2}) due to the low solubility of CO_2 in the electrolyte, however, the total current density in the flow cell is high (>100 mA cm^{-2}). For a flow cell, CO_2 is supplied in the gas phase through flow channels, and the gas-fed CO_2 improves the reaction rates of CO_2RR because of the significantly higher mass transfer of CO_2. Thus, an understanding of the trends for pulse electrolysis under industrial conditions is necessary for further development. In addition to the influence of the local microenvironment, the flow cell takes another advantage by supplemental CO utilization. The combination of CO selective potential and C_{2+} selective potential can lead to improved CO concentration and enhanced CO surface coverage on the catalyst.

This task aims to tune the local concentration of active species at the catalyst layer by tuning the temporal profile of the electrochemical potential pulse to enhance the activity and selectivity of CO_2 reduction and establish the pulse electrolysis protocol at industrially relevant current density.

C.2. Experimental Method

C.2.1 Electrode Preparation

For the preparation of Cu NP electrodes, 10 mg of Cu NPs (Sigma) was dispersed in 10 mL IPA (isopropyl alcohol). The suspension was then sonicated for 1 hour to form catalyst ink. The electrodes were prepared by air spraying the ink onto the carbon paper with a microporous carbon gas diffusion layer (Sigracet 39BB) followed by drying at 130 ℃. The Cu loading was kept constant at approximately 1.0 mg cm^{-2} by measuring the weight of electrodes before and after the spraying.

C.2.2 Electrochemical Test

The selectivity and productivity of gaseous and liquid products were tested in a customized flow cell. The cell system consists of a GDE cathode, a Sustainion anion-exchange membrane, and Ni foam as an anode. 1 M KOH was supplied as the catholyte and anolyte through the electrolyte buffer layers between membrane and cathode/anode at a rate of 0.8 mL min^{-1} controlled by a peristaltic pump (Harvard Apparatus P70-7000). The dry CO_2 feedstock was supplied to the cathode at a rate of 20 standard cubic centimeters per minute (sccm) controlled by a mass flow controller (Alicat Scientific MC-100SCCM-D). The applied potential for a flow cell was controlled by a potentiostatic/galvanostatic station (EnergyLab XM, Solatron Analytical). All potentials are referenced versus a reversible hydrogen electrode (RHE) unless stated otherwise. The potential is calculated without iR compensation. The solution from the catholyte buffer layer was collected to analyze liquid products. The gas products were quantified by gas chromatography (GC, Agilent 7890B), and the liquid products were measured by ^1H NMR spectroscopy (Bruker AV500). For the correct quantification of outlet CO_2 and gas products, a constant stream of Ar gas (10 sccm) was used as an internal reference and evenly mixed with the cell outlet gas stream before it was injected into the GC column. The injection of gas products for GC is set at 200 seconds after the electrolysis started to keep consistency. The solution containing trisodium phosphate (TSP) and H_2O_2 was utilized as the internal reference for NMR spectroscopy.

C.3. Results and Discussion

C.3.1. Pulse Electrolysis in the Flow Cell

We developed pulse electrolysis protocols for the pure Cu electrode and Cu/Fe-N-C SGDE. We aim to perform pulse electrolysis to maximize the selectivity and activity of CO_2RR towards C_{2+} products, especially C_2H_4, while reducing overpotentials (increasing energy efficiency). Instead of using positive reset potential (E_r) to oxidize the Cu surface in the previous study, we emphasize using negative reset potential to provide CO for the following reduction at more negative cathodic potential (E_c), as illustrated in **Figure 13**. The pulse electrolysis was performed in both flow and MEA cells with a serpentine channel. Compared to static electrolysis, the pulse electrolysis improves the FEs of C_2H_4 and C_{2+} products at the same time-averaged potential.

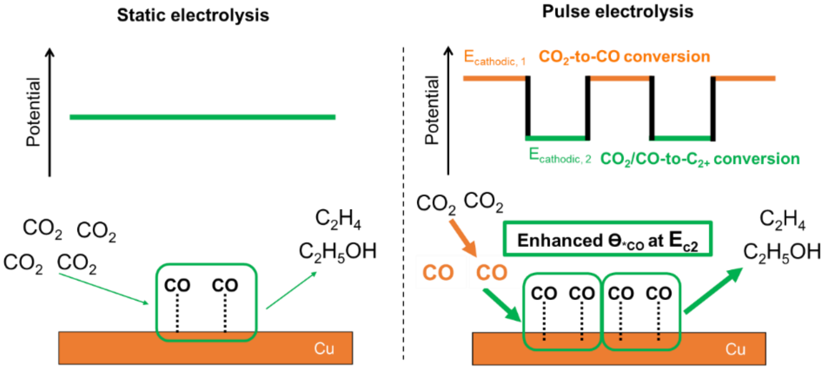

Figure 13. Pulse electrolysis with two alternated negative cathodic potentials at which two tandem reactions occur: CO_2-to-CO conversion and CO-to-C_{2+} conversion. Compared to static electrolysis, the pulse electrolysis improves the selectivity and productivity of C_{2+} products at the same time-averaged potential.

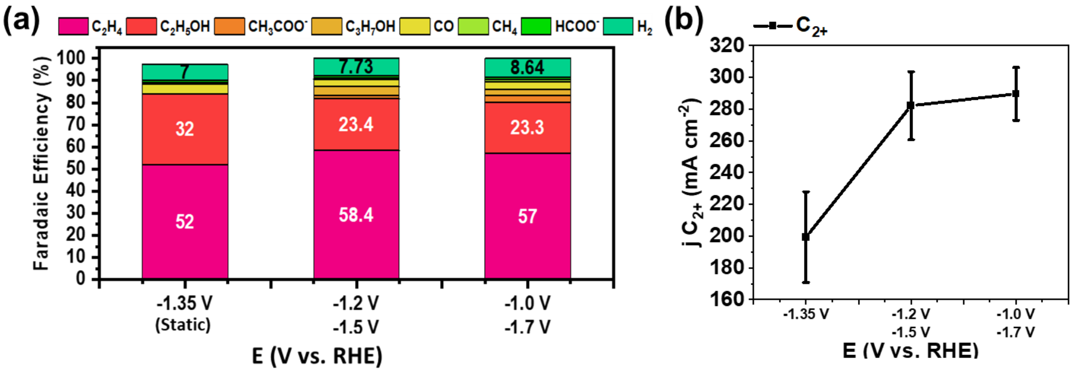

Figure 14. Comparison of FEs and partial current densities of pulsed electrolysis to static electrolysis for Cu GDE in the flow cell. (a) FEs of all CO_2 reduction products. (b) Partial current density of C_{2+} products. The pulse electrolysis duration is t_r (t_{c1})=t_c (t_{c2})= 0.3s.

The initial study to establish the pulse electrolysis protocol was performed in the flow cell using 1M KOH. When applying different combinations of less negative and more negative potentials to the cells, two important factors come into play: CO_2 accumulation and pH effects, which are interrelated. The less negative cathodic potential (E_{c1}) of pulse electrolysis has a lower current density, and the OH^- concentration is lower and the CO_2 utilization is less than the one at a more negative cathodic potential (E_{c2}). Thus, the CO_2 accumulation occurs because of the difference in CO_2 utilization between two cathodic potentials. The increase of CO_2 concentration at E_{c2} lead to a higher rate of CO_2 reduction reactions, and it leads to the increase of the formation of *CO correspondingly. On the other hand, the CO formed at E_{c1} also accumulates at E_{c2} upon potential switching. Therefore, the adsorbed *CO concentration on the catalyst surface increases, and it favors C-C coupling toward the formation of C_{2+} products. This phenomenon is particularly advantageous for C-C coupling, as the rate of C_{2+} product formation is more sensitive to the *CO coverage compared to C_1 products. As a result, the performance observed with pulse electrolysis surpasses that of static electrolysis at the same averaged potential (**Figure 14**).

CO utilization experiences a boost in pulse electrolysis, where we observed lower FE and partial current density of CO compared to potentiostatic electrolysis (**Figure 15**). This result indicates that CO is consumed at a faster rate during pulse electrolysis than during static electrolysis at the same time-averaged potential. In essence, the extra CO from the less cathodic potential facilitates C-C coupling at the subsequent, more cathodic potential within the flow cell.

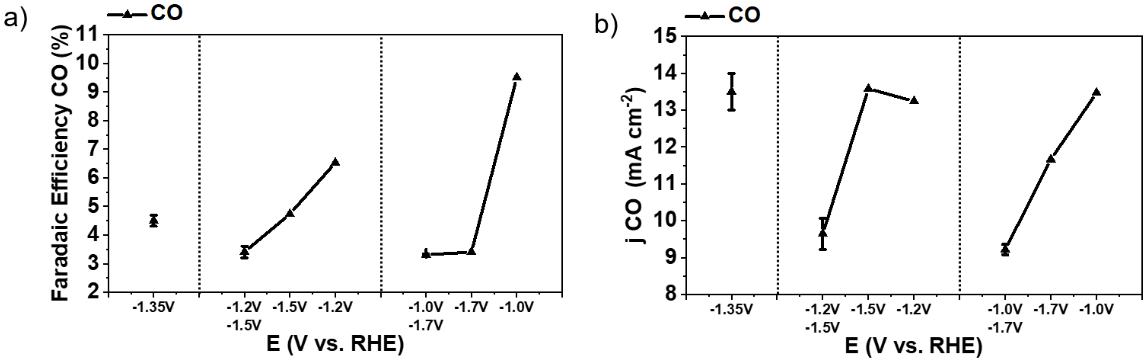

Figure 15. Comparison of pulse electrolysis for Cu NP GDEs in the flow cell with the potential setup (E_{c1}/E_{c2}) of -1.2 V/-1.5 V and -1.0 V/-1.7 V with static electrolysis at potentials of -1.0 V, -1.2 V, -1.35 V, -1.5 V and -1.7 V. The potential is referenced to the RHE scale and does not include iR compensation.

C.4. Summary

To seek industrial applications, pulse electrolysis with alternated two reduction potentials was applied to a flow cell. The pulse electrolysis in the flow cell helps enhance the selectivity and activity of C_{2+} products, especially C_2H_4, due to a combined effect of CO_2 accumulation, enhanced pH, and supplementary CO utilization. Supplementary CO utilization is an advantage of using flow cells. Due to the accumulation, the concentration of CO intermediate near the catalyst surface increases when the more cathodic potential is applied to the cell to produce C_{2+} products. As a result, the production of C_{2+} products especially C_2H_4 is enhanced due to the higher CO surface coverage.

D. Task 5. Demonstrate MEA-type Cell for High Efficiency CO_2-to-C_2H_4 Conversion

D.1. Introduction

The buffer layer in the flow cell accounts for the majority of the total cell ohmic resistance, which is around 2 Ω cm^2 when flowing 1 M KOH in an even 1.5 mm thick buffer layer. Therefore, the MEA-type cell without the buffer layer is required to reduce ohmic loss. The tandem electrodes and pulse electrolysis both can enhance the local CO concentration at the Cu surface, providing synergistic effects. This task aims to combine tandem electrodes and pulse electrolysis into MEA-type cell for CO_2-to-C_2H_4 conversion.

D.2. Experimental Method

D.2.1. Electrochemical Test

Both pure Cu electrode and Cu/Fe-N-C SGDE were used in the pulse electrolysis operated in the MEA cell. The MEA cell consists of a GDE cathode, a Sustainion anion-exchange membrane, and Ni foam as an anode. 1 M KOH was supplied as the anolyte at a rate of 0.8 mL min^{-1} controlled by a peristaltic pump (Harvard Apparatus P70-7000). The dry CO_2 feedstock was supplied to the cathode at a rate of 20 standard cubic centimeters per minute (sccm) controlled by a mass flow controller (Alicat Scientific MC-100SCCM-D). The applied cell voltage was controlled by a potentiostatic/galvanostatic station (EnergyLab XM, Solatron Analytical). The gas products were quantified by gas chromatography (GC, Agilent 7890B), and the liquid products were measured by ^{1}H NMR spectroscopy (Bruker AV500).

D.3. Results and Discussion

D.3.1. Integrate tandem electrodes into MEA-type cell for CO_2 pulse electrolysis

We extended the pulse electrolysis from flow cell to the MEA cell. The MEA cell has lower ohmic resistance than flow cell, thus potentially having higher energy efficiency. Similar to the results obtained in the flow cell, our study with the Cu GDE in the MEA cell also demonstrates that pulse electrolysis enhances the selectivity and productivity of C_2H_4 compared to static electrolysis at the same time-averaged cell voltage (**Figure 16**).

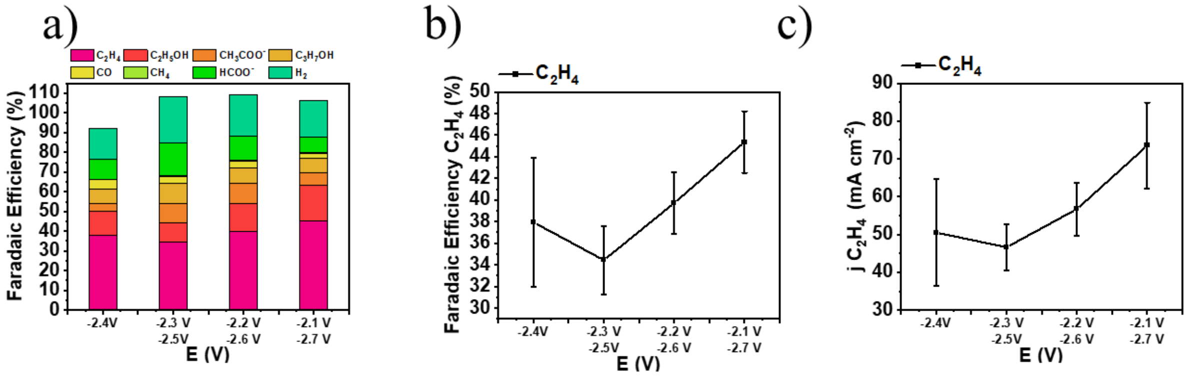

Figure 16. Comparison of FEs and partial current densities of pulsed electrolysis to static electrolysis for Cu GDE in the MEA cell. (a) FEs of all CO_2 reduction products. (b) FE of C_2H_4. (c) Partial current density of C_2H_4. The static electrolysis was operated at cell voltage of 2.4 V. The pulse electrolysis duration is $t_{c1} = t_{c2} = 0.3$ s. Three combinations of pulse cell voltage (E_{c1}/E_{c2}) were used: 2.3 V/2.5 V, 2.2 V/2.6 V, and 2.1 V/2.7 V. The cell voltage is without iR compensation.

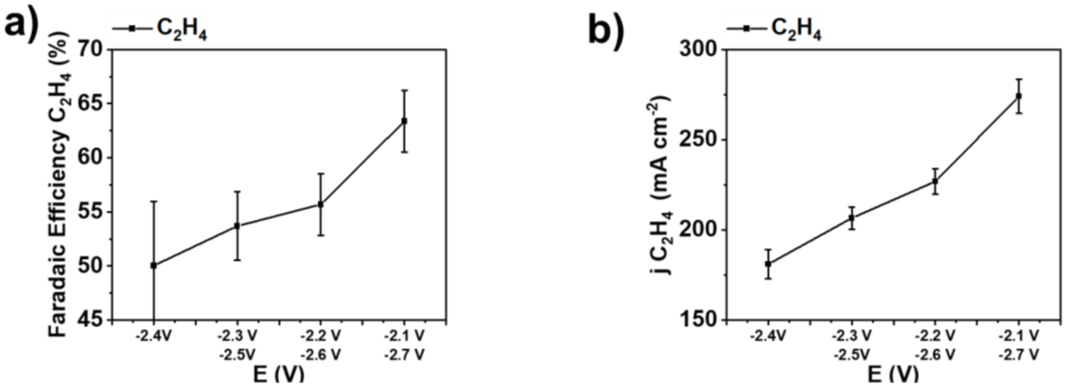

Figure 17. Comparison of FEs and partial current densities of pulsed electrolysis to static electrolysis for Cu/Fe-N-C SGDE in the MEA cell. (a) FE of C_2H_4. (c) Partial current density of C_2H_4. The static electrolysis was operated at cell voltage of 2.4 V. The pulse electrolysis duration is t_{c1} = t_{c2} = 0.3 s. Three combinations of pulse cell voltage (E_r/E_c) were used: 2.3 V/2.5 V, 2.2 V/2.6 V, and 2.1 V/2.7 V. The cell voltage is without iR compensation.

Similarly, when we conducted the pulse test on Cu/Fe-N-C SGDE in the MEA cell, the optimal pulse electrolysis led to a 26% increase in FE and a 50% increase in the partial current density of C_2H_4 compared to static electrolysis at the same time-averaged cell voltage (**Figure 17**). This enhanced selectivity and productivity of C_2H_4 during pulse electrolysis can be attributed to a combination of dynamic changes in pH, CO, and CO_2 concentrations near the Cu surface.

We monitored the anode potential during pulse electrolysis. The average anode potential was 1.72 V vs. RHE. The cathode potential is around -0.30 V vs. RHE calculated by subtracting the ohmic loss (internal resistance 0.82 Ω cm^2 × 0.432 A cm^{-2} = 0.35 V) and anode potential from the average cell voltage. The half-cell cathodic energy efficiency (CEE) was calculated by the equation [1]:

$$CEE = \frac{(1.23 - E^0_{C2H4}) \times FE_{C2H4}}{1.23 - E_{cathode}} \qquad [1]$$

where the overpotential of anodic oxygen evolution reaction is assumed to be zero, E^0_{C2H4} denotes the standard potential of CO_2 reduction to C_2H_4, 0.08 V vs. RHE, FE_{C2H4} is the FE of C_2H_4, and E_{cathode} is the applied potential of cathode. Under the pulse electrolysis protocol of E_{c1}= 2.1 V and E_{c2}= 2.70 V with 64% FE of C_2H_4, the half-cell CEE is around 48%.

D.4. Summary

The pulse electrolysis provides the enhancement for C_2H_4 formation in the MEA cell due to the change in the local environment and CO utilization as the flow cell configuration is achieved. The FE of C_2H_4 was enhanced by over 25% compared to the potentiostatic electrolysis at the time-average cell voltage, and the partial current density of C_2H_4 products was also improved by 50%. Pulse electrolysis can be implemented in SGDE to augment the selectivity and productivity of C_2H_4. It's worth noting that, to prevent the flooding effect, the pulse electrolysis was executed at a low cell voltage on the SGDE.

E. Task 6. Technoeconomic analysis of a self-sustained, integrated system for capture and conversion of CO_2 to C_2H_4: new prospects for large-scale deployment

1. Motivations and Background Information

Global net anthropogenic emissions have been steadily climbing in the past decades, with only exception of a shallow decline during the recent pandemic. [1] Current predictions project that the current rate of pollution will cause deviation of global average temperatures to exceed the 1.5 ℃, *e.g.*, the limit set by the Paris climate accord. [2] This would have a wide array of negative environmental effects throughout the globe as well as social implications, as these effects may affect impoverished regions of the world to a greater extent, as, for instance, they would be more vulnerable to food and water sector disruptions. [3-4] One of the most drastic effects of global warming is the best known being the rising sea level. [2]

Among various strategies to mitigate climate change, Carbon Capture and Storage has long been considered a plausible approach. [5] This tactic relies on capturing CO_2 with various methods and different sources and then storing it underground, usually in depleted oil reserves. However, carbon storage by itself cannot be considered a definitive solution, but rather as a temporary expedient to decrease the CO_2 budget in the atmosphere, as we transition to a greener economy. Furthermore, capturing CO_2 and storage is usually a rather expensive process, which may appear disadvantageous or unfeasible for several industries.

In this context, carbon capture and utilization (CCU), wherein CO_2 is used as the precursor for useful, valuable chemicals may be a more appealing option, as well as good compromise between economics and environmental protection. In this study, we analyze a complex, integrated system for CCU to be employed to convert industrial emissions into useful chemicals via a series of electrochemical reactions. We will carefully evaluate the investment required for assembling the set-up, its operation cost, and any eventual revenue for producing ethylene starting from CO_2 emissions. The total cost of production for C_2H_4 via this novel integrated system will therefore be evaluated. Before operational aspects are added a systematic design process takes place to optimize the design of the anion exchange membrane (AEM) reactor, hybrid electrolyte electrochemical membrane reactor (HE-EMR), and the solid oxide electrolysis cell (SOEC) reactor. Following, Parametric analysis will be carried out by considering different operation parameters to evaluate the conditions at which the manufacturing and operation costs are fully balanced by the potential revenue for ethylene, based on its current market price.

2. Mathematical Model

In this section, we report a detailed description of the mathematical models used to evaluate the impact of manufacturing and operating different critical components of the integrated set-up. In the first section, we will outline the characteristics of the gas used to simulate the output stream of an energy/industrial power plant. Then we will describe all the necessary components of the setup. We will first qualitatively model and evaluate the impact of necessary auxiliary equipment (gas cleaner, heat exchangers, and other auxiliary equipment) before reviewing in detail the modeling process for the three modular reactors.

2.1. Industrial stream characteristics

Incoming Gas. This section provides a description of the chosen initial composition of the industrial incoming gaseous stream (**Table 1**). The chemical compositions and other characteristics of the gas (e.g., flow rate, pressure, temperature etc.) will depend on its emission source. In this study, we assume a temperature of 600° C for the incoming industrial stream. The mass flow rate was set to 360. kg/hour. The data was evaluated considering that the cumulative percentage mass of the N_2, O_2, and CO_2 make up a total of ~70% of the industrial stream with N_2 being the most abundant gas. The remaining 30% in mass may include a mixture of various unspecified gasses (H_2O, NO_x, SO_x), as well as particulate matter and other types of pollutants.

Table 1: Industrial stream composition and characteristics.

Incoming industrial Parameters	**Value**	**Units**
Mass flow rate incoming	360.	kg/hr
Temperature	600	°C
Pressure	5.0	atm
CO_2	20.5%	
N_2	45.7%	
O_2	3.7%	
Other gasses and PM	30.0%	

The industrial stream interacts with the first element of the set-up consisting of a gas cleaner which is described in the next section (**Gas Filter**).

2.2. Auxiliary Equipment

Gas Filter. To the best of our knowledge, no previous detailed reports of gas cleaning units suitable for our purpose has been reported. Thus, here we report a qualitative assessment of the capital cost for manufacturing a gas cleaning unit. The composition and characteristics of the industrial stream are reported in **Table 1**. The type of cleaning unit will depend on the gas composition and other gas characteristics such as the temperature.[8] For instance, barrier filters may be used for blocking solid particles within the gas stream and may be constructed with different materials, including ceramic and metal/metal oxide sorbents. For high temperature applications, rigid hot gas filters may be employed. For obstructing the flow of molecular and particulate contaminants in low temperature gases, good candidates for membrane filters may be polymeric materials, such as poly[1-trimethlysily-1-propyne] or PTMSP (glass transition temperature >300° C).

Here, we do not report a detailed modelling of the gas filter as this is beyond the scope of this study. We do however present a generic system model to demonstrate that the cost of manufacturing the filter is negligeable compared to investment required for constructing the reactors. As a proof of principle, we propose a simple model of a gas membrane filter made of a polymeric material (PTMSP).

The mass flow rates of the components i ($\dot{m}_i$) entering the gas filter was calculated from their mass fraction (x_i) and total mass flow ($\dot{m}_t$), according to Eq. [1].

$$\dot{m}_\iota = x_i \dot{m}_t$$

[1]

The mass of the retentate ($m_{r,t}$) and permeate ($m_{p,t}$) can be easily calculated from Eq. [2] and [3], considering the mass of the components i retained ($m_{r,i}$) on or permeating ($m_{p,i}$) through the membrane filter:

$$m_{p,t} = \sum_{i=1}^{l} m_{p,i}$$

[2]

$$m_{r,t} = \sum_{i=1}^{l} m_{r,i}$$

[3]

For practical purposes, the mass flow rate may be converted to a molar flow rate ($\dot{N}_t$) using the molar mass of component *i* (MW_i) as in Eq. [4].

$$\dot{N}_t = \sum_{i=1}^{l} \dot{N}_i = \sum_{i}^{l} \frac{\dot{m}_i}{MW_i}$$

[4]

Analogously, the mole fraction of component *i* (y_i) can then be also calculated and further used to obtain its partial pressure (p_i) in the gas stream of total pressure P_T, in accord to Eq.[5]:

$$p_i = p_T y_i$$

[5]

For permeable gases passing through a membrane of area A and thickness t_{ms}, the molar flux ($J_{m,i}$) of the *i*th component with the permeability P_i in PTMSP (**Table S2**)[7] and molar density of $\rho_{m,i}$ can be obtained from Eq. [6]:

$$J_{m,i} = \frac{P_i A \rho_{m,i}}{t_{ms} y_{i,p}} \left[p_h y_{i,r} - p_l y_{i,p} \right]$$

[6]

Where $y_{i,r}$ and $y_{i,p}$ are the molar fraction of *i* on the high- and low-pressure sides, respectively, and p_h and p_l are the total pressures on the high- and low-pressure sides.

The permeability coefficients for various gasses through the membrane are listed in **Table 2** and were used for the purpose of evaluating the quantity of polymeric membrane required to construct the filter.

Table 2: permeability coefficients for various gasses through the chosen membrane

Molecule	Permeability Coefficients, P_i ($m^2/(s \cdot atm)$)
CO_2	2.13×10^{-8}
N_2	5.87×10^{-9}
O_2	3.78×10^{-9}

From Eq. [6], the area of the membrane can be evaluated for a set thickness t_{ms} for a set component *i*. Since N_2 represents the most abundant component in the incoming stream and in the permeate, its flux was used for this purpose. To do so, the thickness of the membrane was fixed to 0.50 mm and the area A of the membrane was computed to allow to obtain the required molar flux of N_2. The capital cost of the filter was assumed to be primarily dictated by the cost of the polymeric membrane ($50/m^2). For a 0.50 mm PTMSP membrane, with a safety factor of 1.1 on the overall membrane area, the cost of the membrane filter was then evaluated as $313, which is expected to represent a negligible fraction on the overall capital cost.

Heat Exchanger 1 and 2. The assembly includes two distinct heat exchangers. The first heat is required for fuel cell (HE-EMR) operation, and has the purpose of adjusting the temperature of the gas to a temperature optimal for HE-EMR operation, here taken as 600° C. As the initial temperature of the gas stream may vary depending on its industrial source, thus the incoming (clean) gas may require heating or cooling to the desired temperature. In this study, we assume that the temperature of the industrial stream is compatible with the operation of the HE-EMR; as such, the setup optimizes energy requirements for operation by taking advantage of the high temperature of industrial gas stream.

A heat exchanger unit is also located between point A and the AEM. This unit has the purpose of cooling the hot gas from HE-EMR (as/if required) to a temperature suitable for operation of the AEM (here taken as 80° C). In this case the heat exchanger could work through water cooling system, which is operated by a circulator pump.[6]
In this study, we did not perform a rigorous modelling of these units. However, based on previous reports, we will assume that the manufacturing cost amounts to ~2% of the overall cost of the modular reactors. As for any energy requirements for operation of the heat exchanger (e.g., electricity for circulator pump), we incorporate their contributions into the balance of plant (see section "Adjustment factors").

Adjustment factors. Our cost analysis included an adjustment factor which is used to approximate the installation and manufacturing cost of auxiliary equipment and other necessary items (e.g., pipes, valves, electrical equipment etc.). For this study, this was set to adjustment factor of 5% of the overall cost of the reactors. At the same time, the balance of plant needs to be accounted as part of the energy requirements for operating the set-up. In this study, we approximate the balance of plant as 5% of the energy consumption of our baseline model.

2.3. The Reactors

HE-EMR. The HE-EMR is a solid oxide fuel cell which will aid concentrating the incoming CO_2 stream to concentration suitable for the following CO_2ER to ethylene. This cell consists of an anode wherein the half-reaction is described in Eq. [7].

$$CO + CO_3^{2-} \rightleftharpoons 2CO_2 + 2e^- \tag{7}$$

The half-reaction at the cathode is described in Eq. [8]:

$$CO_2 + \frac{1}{2}O_2 + 2e^- \rightleftharpoons CO_3^{2-} \tag{8}$$

As a result, the total net reaction can then be illustrated as in Eq. [9].

$$CO + \frac{1}{2}O_2 \rightleftharpoons CO_2 \tag{9}$$

Thus, one can calculate the Gibbs free energy $\Delta_r G_m$ of reaction [9] from the standard reaction free energy $\Delta_r G_m^0$ and the partial pressure of the reactants and products:

$$\Delta_r G_m = \Delta_r G^\circ{}_m - RTln\left(\frac{P_{CO_2,c}\, P_{co} P_{O_2}{}^{\frac{1}{2}}}{P_{CO_2,a}{}^{2}}\right) \tag{10}$$

The $\Delta_r G_m$ can the be used to calculate the Nernst voltage (E_n) using Eq. [11], alongside the Faradaic constant F and the number of electrons n transferred during the electrochemical process:

$$E_n = -\left(\frac{\Delta_r G_m}{n \cdot F}\right) \tag{11}$$

The operation voltage for a single cell can then be set as depending on the area specific resistance R_{HE-EMR} (W cm^2) at a set current density, j_{HE-EMR} (A/cm^2):

$$V_{Cell} = E_n - j_{HE-EMR} \cdot R_{HE-EMR} \tag{12}$$

While investigating the dependence of V_{Cell} on R_{HE-EMR}, the energy efficiency can also be defined and assessed according to Eq. [13]:

$$\eta_{HE-EMR} = \frac{V_{Cell}}{E_n} \times 100 \tag{13}$$

Furthermore, considering a stack of N_{cell} cells of individual area (A) connected in series, the operation voltage (V_{HE-EMR}) and current (I_{HE-EMR}) for the stack can be calculated according to Eqs. [14] and [15]:

$$V_{HE-EMR} = V_{Cell} \cdot N_{cell} \tag{14}$$

$$I_{HE-EMR} = j_{HE-EMR} \cdot A \tag{15}$$

The power requirement for the HE-EMR (P_{HE-EMR}) can then be easily calculated using Eq. [16]:

$$P_{HE-EMR} = V_{Cell} \cdot I_{HE-EMR} \tag{16}$$

For this study, we assumed a 100% conversion rate of CO_2 at the cathode and a 90% conversion rate of CO at the anode.

Table 3 lists all thermodynamical and electrochemical properties and their set values used for the baseline HE-EMR model; thermodynamic properties were calculated considering molar fractions for CO_2, N_2 and O_2 of 0.2, 0.7 and 0.1 at the cathode, wherein the total pressure is set to 1 atm. For the anode the molar fractions of CO and CO_2 were 0.95 and 0.05 respectively, and the total pressure was set to 1 atm.

Table 3: The thermodynamic and electrochemical properties of the HE-EMR

Property	Value
$\Delta_r S^\circ{}_m$	-0.0865 kJ K^{-1} mol^{-1}
T	600° C
$\Delta_r H^\circ{}_m$	-282.984 kJ mol^{-1}
$\Delta_r G^\circ{}_m$	-207.457 kJ mol^{-1}

$\Delta_r G_m$	-200.346 kJ mol^{-1}
E_n	1.038 V
R	0.40 W cm^2
j	1.00 A cm^{-2}
A	900 cm^2
V_{cell}	0.638 V
I	900 cm^2
N_{cell}	100
$V_{HE\text{-}EMR}$	63.822 V
$P_{HE\text{-}EMR}$	57.440 kW
η	61.473%

The molar flow rates of various chemical species at the cathode and anode can be derived as in **Table 4**.

Table 4: gas composition at the electrodes of HE-EMR:

Cathode (P_{TOT} = 1 atm)			
Inlet		**Outlet**	
Species	Molar Flow, j (mol/s)	Species	Molar Flow, j (mol/s)
CO_2	0.466	CO_2	0.00
N_2	1.632	N_2	1.632
O_2	0.232	O_2	0.00
Anode (P_{TOT} = 1 atm)			
Inlet		**Outlet**	
Species	Molar Flow, j (mol/s)	Species	Molar Flow, j (mol/s)
CO_2	0.027	CO_2	0.960
CO	0.518	CO	0.052

The operation cost for the HE-EMR is dictated by (i) its energy consumption and (ii) the cost of electricity for each kWh used. While the energy consumption is kept fixed, the effect of varying the cost of electricity was explored in this study.

To evaluate the capital cost associated with the HE-EMR assembly, we referred to the estimate cost of manufacturing solid oxide cells, as specified in recent reports. [ref] For the HE-EMR the current cost is ~690 $/kW, while the target cost to be aspire to for future manufacturing is ~90 $/kW. Both estimates will be used to assess the effect of manufacturing costs in the overall economics.

Point A. At point A, the output of the anode of the HE-EMR is split into two separate lines. One of the lines directs the gas towards the auxiliary unit (SOEC) while the other is dedicated to delivering gas to the AEM. For this system, the total molar flow required the cathode of SOEC ($\dot{N}_{t,c}$) is 0.545 mol/s, while the remaining flow will be directed to the AEM.

SOEC. The SOEC unit receives the incoming flux of CO_2 from point A and reduces it into CO through an electrochemical reduction. The anode and cathode half-reactions are shown in Eqs.
[17] and
[18], alongside the overall net reaction in Eq.
[19]:

$$O^{2-} \rightarrow 2e^- + \frac{1}{2}O_2$$

[17]

$$2e^- + CO_2 \rightarrow O^{2-} + CO$$

[18]

$$CO_2 \rightleftharpoons CO + \frac{1}{2}O_2$$

[19]

As the SOEC acts as auxiliary unit to the HE-EMR, it is convenient to set its operation conditions based on the requirements dictated by the composition of gas at the cathode, which is dictated by the HE-EMR. For the cathode, the gas composition includes 94.9% CO_2, and the remaining percentage fraction is made up by CO, for a total pressure of 1 atm (see **Table 4**). The composition at the anode is then made up of 21.0% O_2 seeded in N_2 (total pressure 1 atm). Thus, the $\Delta_r G_m$ for the SOEC can then be evaluated as for the HE-EMR, according to Eq. [10], which then allows to calculate the Nernst voltage (see Eq. [11]). All subsequent properties (η_{SOEC}, V_{SOEC}, P_{SOEC} etc.) are then calculated in a similar fashion to the method reported in Eq. [13] – [16]. For instance, as stated above, the gas flow at the cathode and its composition are dictated by the HE-EMR and the overall flow is set at point A. Thus, the CO production rate (r_{CO}) at the cathode is evaluated from (i) the total molar low rate ($\dot{N}_{t,c}$), (ii) the input molar fraction of CO $y_{CO,i}$ (here set to 0.05) and target output molar fraction of CO $y_{CO,o}$ (0.95), as in Eq. [20]:

$$r_{CO} = \dot{N}_{t,c} \cdot (y_{CO,o} - y_{CO,i})$$

[20]

Considering the desired r_{CO}, the total current through the SOEC (I_{SOEC}) stack can be calculated from Eq. [21]:

$$I_{SOEC} = \frac{r_{CO} \times F \times n}{N_{cell}}$$

[21]

The current density j_{SOEC} is then computed as the ratio between I_{SOEC} and the area A (900 cm^2). Finally, the operation voltage for a single cell and stack are computed according to Eq. [22] and [24]:

$$V_{cell} = E_n + j_{SOEC} \cdot R_{SOEC}$$

[22]

$$V_{SOEC} = V_{cell} \cdot N_{cell}$$

[23]

The power requirement for the SOEC is then calculated using Eq. [16].**Tables 5** summarizes all the calculated thermodynamic and electrochemical quantities of the SOEC.

Table 5: The thermodynamic and electrochemical properties of the HE-EMR

Property	**Value**
$\Delta_r S^{\circ}_m$	-0.0865 kJ K^{-1} mol^{-1}

$\Delta_r H^{\circ}{}_m$	-282.984 kJ mol^{-1}
T	800° C
$\Delta_r G^{\circ}{}_m$	-190.157 kJ mol^{-1}
$\Delta_r G_m$	-157.147 kJ mol^{-1}
E_n	0.814 V
R	0.30 Ohm cm^2
j	1.05 A cm^{-2}
A	900 cm^2
V_{cell}	1.130 V
I	946 A
N_{cell}	100
V_{SOEC}	112.973 V
P_{SOEC}	106.882 kW
η	72.085%

AEM Reactor. The AEM is the last reactor in the setup and has the purpose of converting the incoming CO_2 to ethylene. The relevant reactions steps for CO_2-to-ethylene conversion are shown Eqs. [24] – [26]. The cathodic half-reaction follows the two-step mechanism wherein CO_2 is initially converted to CO (Eq.[24]) and then subsequently reduced to ethylene (Eq.[25]), for a total of 12 moles of electron required.

Step I: $$CO_2 + H_2O + 2e^- \rightarrow CO + 2OH^- \quad [24]$$

Step II: $$2CO + 6H_2O + 8e^- \rightarrow C_2H_4 + 8OH^- \quad [25]$$

Half Reaction: $$2CO_2 + 8H_2O + 12e^- \rightarrow C_2H_4 + 12OH^- \quad [26]$$

At the anode, the oxygen evolution reaction takes places (Eq. [27]).

$$12OH^- \rightarrow 3O_2 + 6H_2O + 12e^- \quad [27]$$

The full net reaction for the AEM reactor can then be written as in Eq. [28]:

$$2CO_2 + 2H_2O \rightarrow 3O_2 + C_2H_4 \quad [28]$$

Analogously to the previous reactors, the E_n can be calculated from the thermodynamics of the reactions, with the caveat that the incoming CO_2 flow is dictated by the set amount at Point A. Thus, other properties (e.g., V_{cell}, V_{AEM}, I_{AEM}, P_{AEM}) can be computed as for the other reactors (**Table S6**).

Table 6: The thermodynamic and electrochemical properties of the HE-EMR

Property	Value
T	80° C
$\Delta_r G_m$	1331.4 kJ mol^{-1}
E_n	1.150 V
R	3.00 Ohm cm^2
j	1.00 A cm^{-2}
A	900 cm^2
V_{cell}	4.150 V
I	900. A
N_{cell}	100.
V_{AEM}	622.488 V
P_{AEM}	560.238 kW
η	27.71%

Baseline system and parametric studies. In this study, we proceeded by constructing a baseline system to first evaluate the production cost of ethylene from CO_2 using the novel set up described above. This proposed model system includes contributions from both operation and capital cost. The results of the analysis are reported and discussed in the main text of this manuscript. To optimize the production cost of ethylene, numerous parameters were then scanned across wide ranges with the aim of optimizing the economic impact of manufacturing and operating conditions.

The power section there is an equipment section that covers all the equipment that will have to be purchased to operate the equipment. To assess the equipment costs it first has to be designed for the maximum operational current density. This is done by setting the current density of the AEM to 1 A/cm^2 and then solving for the current densities of the SOEC and the HE-EMR. Once this has been done the number of cells are then parameterized to find the lowest equipment cost while not reducing the production amount. This optimal design then was set to the reference value which was used throughout the rest of the price calculations thereafter.
This is parameterized based on the user-entered values for the power density and in total covers forty-eight data points. Each one of the entered power densities was then used to find the values for the operational power densities of the HE-EMR and the SOEC. Once the total equipment cost has been found it is then added to the cost of electricity for the given time that the user entered. This value is then subtracted from the profit incurred from ethylene production to find the net profit. This net profit is then used to find the optimal operational current density which is then used for the second parameterization study. This parameterization study scans through prospective resistivities for the cell to find its effect on cost. For either of the studies the profit is then divided by the investment to find the ROI if the value is greater than zero which represents the minimum amount to be profitable. Although, having a ROI of 100% was also noted as being desirable especially if it is achievable within the life span of one electrochemical cell. This value is then adjusted to a per-year basis for comparative purposes, and I have also added a statistics page for further statistical calculation based on the results.

3. Results and Discussion

3.1 Baseline model system

The production cost of ethylene for the baseline systems (case 1 – 3) is evaluated according to the parameters reported in **Table 3-6.** The associated results are illustrated in **FIG 1**. The chosen c_e (0.02 $/kWh) reflects the current price of renewable electricity (*e.g.*, from wind sources).[22,23] The only distinction between the three cases is the cost of the equipment, primarily dictated by that of the reactors with the AEM making up 46-63% of the overall capital cost. The capital investment is estimated based on current average cost of the solid oxide cells and AEM reactors (case 1), the desired price of the assemblies according to recent TEAs (case 3) and an intermediate case between the two (case 2).[24] An adjustment factor is used to account for auxiliary equipment, and other indirect costs. In all cases, the operation contributes the most to the product cost at the set conditions. The total energy consumption for operation, including balance of plant, amounts to 44.8 MWh/mt of product – 99% of which is allocated to the AEM (cyan bars, **FIG 1**). The cost of SOEC operation (grey bars) is always the smallest contribution, since this reactor is partially supported by the HE-EMR (line pattern, **FIG 1**). This expedient allows reducing the cost of SOEC operation by ~93%. Under no instance the cost of the reactors is to be considered negligeable since it can account for a hefty ~47% at the current state-of-the-art (case 1).

Since the AEM operation is the largest contributor to the product cost, parameters related to the AEM performance will be the most cost sensitive. Therefore, we will perform parametric studies to evaluate how optimizing the AEM can lower the product cost. Parameters explored will be: (a) current density/cell voltage and area specific resistance (ASR), (b) Faradaic Efficiency, (c) stability/durability over time (cell degradation/aging).

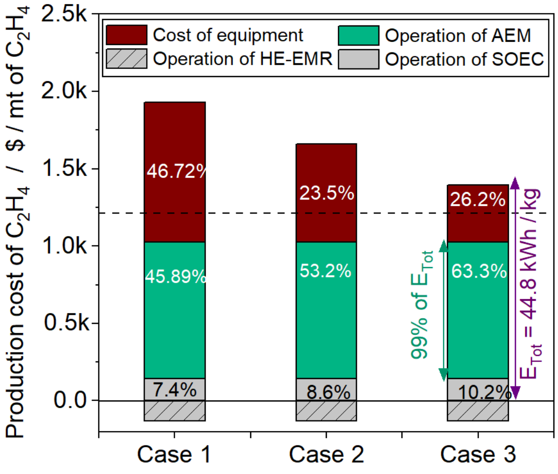

FIG 1: Baseline model systems (I=0.5 A/cm^2) to produce C_2H_4 using the modelled set-up for CO_2 capture and electrolysis. The bars represent the breakdown of the production cost of C_2H_4 into contributions of operation of the reactors *vs* cost of the equipment for case 1 – 3. The three cases only differ by the cost of the equipment (from high to low). Cost of electricity is set to 0.02$/kWh. The horizontal dashed line represents the market price of C_2H_4 in 2022. The Faradaic efficiency for CO_2 to C_2H_4 conversion was fixed at 65% and the set-up is assumed to operate for 50,000 hours. The cost is referenced to the production of 1 mt of C_2H_4.

3.2 Parametric Studies

Energy Requirements and Energy Efficiency. The energy requirements for CO_2-to-C_2H_4 electro conversion have profound repercussion on the final product cost (henceforth, c_{ethene}). First, the effect of varying the current density for the AEM (j_{AEM}) and associated voltage (V_{AEM}) is explored. In first approximation, the ASR is kept constant at various j_{AEM} values. The associated energy efficiency is also derived accordingly.

The c_{ethene} as a function of j_{AEM} and c_e is displayed in **FIG2 (a)-(c)**, while **FIG 3** shows the equivalent results broken down by source at four different j_{AEM} (c_e = 0.02 \$/kWh). The overall c_{ethene} is dictated by the interplay between the cost of operation and that of the equipment. At low current densities, *e.g.*, instances for which the product output is low, the cost of the equipment accounts for up to 70.0% of c_{ethene} (case 1, **FIG 3**). The predicted c_{ethene} reaches a minimum at high current densities (0.3- 1.0 A cm^{-2}, **FIG 2**), wherein higher product yields allow minimizing the impact of manufacturing processes. Further increase in j_{AEM}, results in a steady rise in c_{ethene}, due higher energy requirements to perform CO_2ER. The optimal j_{AEM} depends both on cost of the equipment and electricity. Firstly, progressively lower c_e tends to shift the optimal j_{AEM} towards higher values. In essence, lowering of the operational cost of the AEM clearly allows for higher energy usage while retaining competitive c_{ethene}, which is beneficial to increase the yield of ethylene.

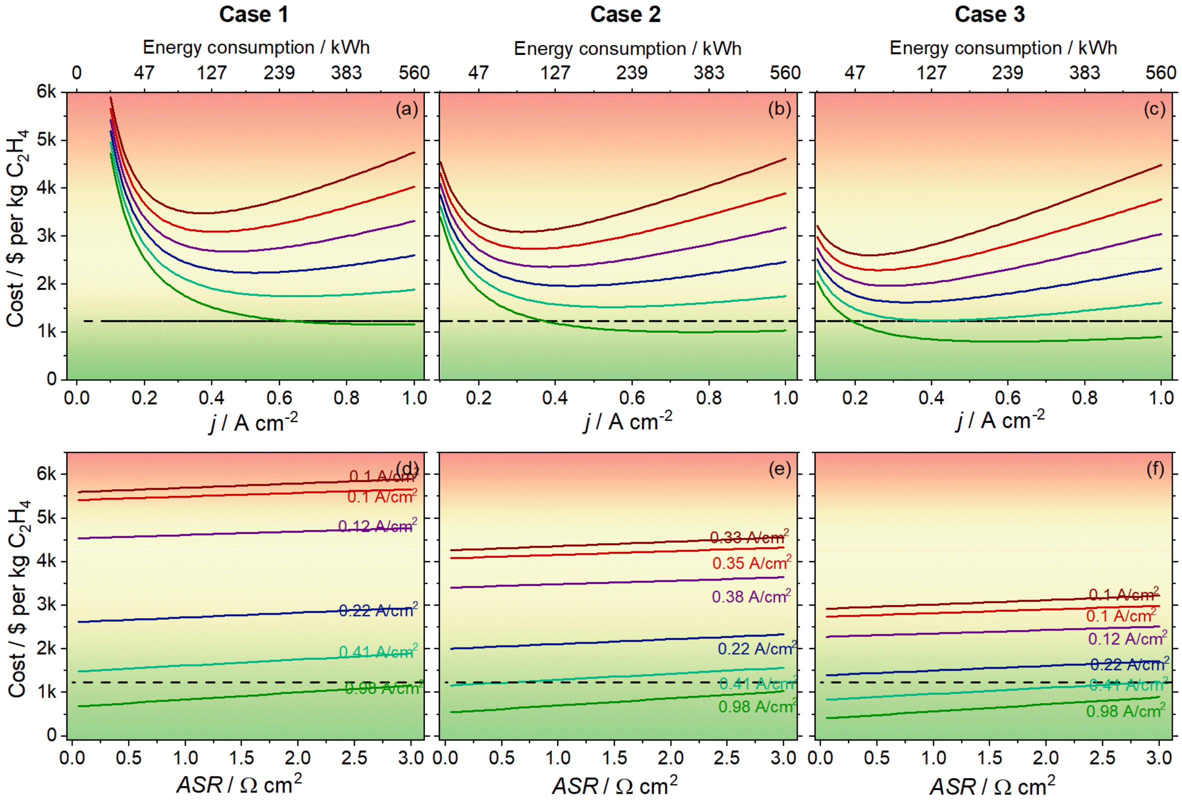

FIG 2: production cost of C_2H_4 using the modelled set-up for CO_2 capture and electrolysis. (a) – (c) Effect of varying current density for case 1 – 3 at different prices of electricity; (d) – (f) effect of ASR for case 1 – 3. The horizontal dashed line represents the market price of C_2H_4 in 2022. The Faradaic efficiency for CO_2 to C_2H_4 conversion was fixed at 65% and the set-up is assumed to

operate for 50,000 hours. The cost is referenced to the production of 1 mt of C_2H_4. Cost of electricity is set to 0.02\$/kWh.

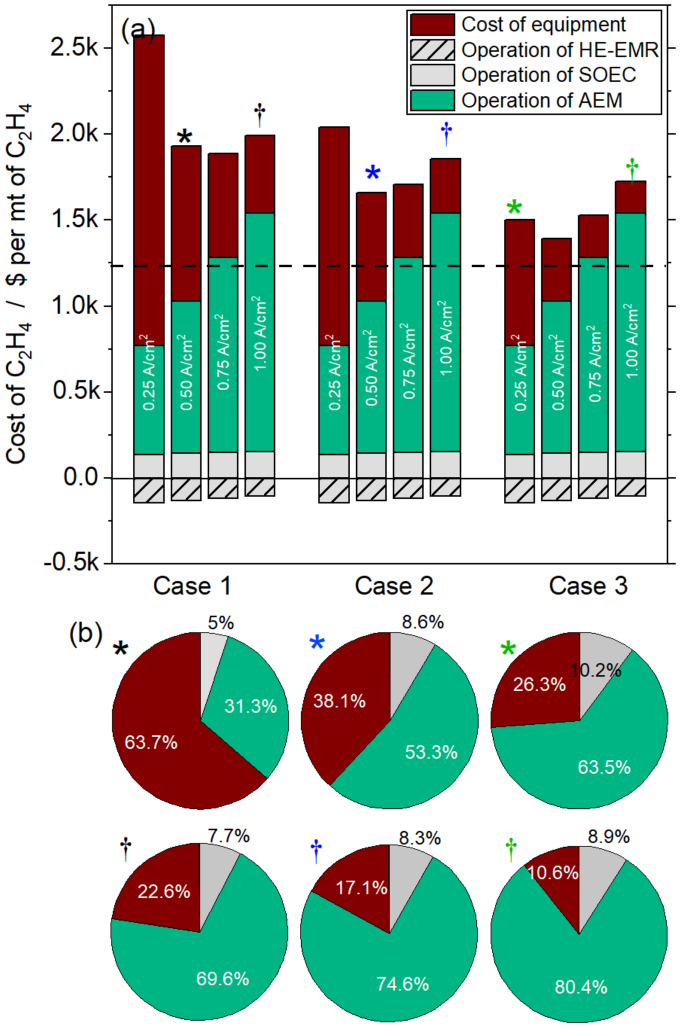

FIG 3: Breakdown of the production cost of C_2H_4 using the modelled set-up for CO_2 capture and electrolysis. (a) Contributions of operation of the reactors vs cost of the equipment for case 1 – 3 at different current densities and (b) the corresponding percentage contributions. The operation of the HE-EMR is explicitly displayed as a negative contribution; this is related to the production of electricity by this reactor. The Faradaic efficiency for CO_2 to C_2H_4 conversion was fixed at 65% and the set-up is assumed to operate for 50,000 hours. The cost is referenced to the production of 1 mt of C_2H_4 and cost of electricity was fixed to 0.02 \$/kWh.

In turn, this may aid amortizing the cost of equipment. If we reference to the market price of ethylene in 2022 (\$1,235\$/mt, dashed line in **FIG 2 and 3**) against the current average price of electrochemical reactors (case 1), a very narrow range of high current densities (~0.6 A cm^{-2}) are required to achieve competitive c_{ethene}, exclusively at 0.01\$/kWh. A moderate decrease in the equipment cost (case 2) allows a somewhat wider range of desirable current densities at the same c_e. If one projects the cost of equipment to the target case scenario (case 3), then very competitive

c_{ethene} values are achieved at most current densities for a c_e of 0.01$/kWh. Furthermore, at the current price of renewable electricity (0.02$/kWh), competitive c_{ethene} values are still achievable at in a wide range of j_{AEM} (0.4-1.0 A cm^{-2}). These results suggest the economic feasibility for ethylene production using state-of-the-art reactors integrated in our novel set-up. Manufacturing costs are further amortized at ultra-high j_{AEM} (*vide* 1.00 A cm^{-2}), nonetheless, energy requirements for operation of AEM become overwhelming. This causes c_{ethene} to increase steadily with j_{AEM} in this ranges.

The j_{AEM} yielding minimum c_{ethene} is identified in each curve (*vide* cross symbols, **FIG 2**) and fixed for further analysis. Firstly, we consider the effect of varying ASR as in **FIG 2**. Clearly, a linear dependence of c_{ethene} on the ASR is observed. In a purely theoretical scenario where ASR is projected to 0 W cm^2, V_{AEM} is exclusively dictated by the Nernst voltage. From **FIG 2,** it is apparent that the Nernst voltage has a much higher impact on the overall c_{ethene} *cf*. ASR. Nonetheless, increasing ASR can still reflect in a fairly steep increase in c_{ethene} , on averaged by a factor of 1.3-1.5 across the range explored in this study. These findings highlight the upmost importance of low ASR for both performance of electrochemical reactors and economic viability of their corresponding processes.

Faradaic Efficiency. Clearly selectivity for formation of the desired product is essential for the economic feasibility of a chemical process. Although ethylene is notably a product of CO_2ER for which selectivity may benefit from improvement, several recent studies achieved Faradaic Efficiency for ethylene production (FE_{C2H4}) by far exceeding 50%.[125] In this context, FE_{C2H4} provides a measure of the selectivity of the CO_2ER and the efficiency of energy use towards forming the product of interest. It is therefore an important variable to explore in this study. **FIG 4** shows the c_{ethene} as a function of both j_{AEM} and FE_{C2H4} (c_e=0.02$/kWh). At the limiting case wherein FE_{C2H4} approaches 100%, all case 1-3 yield potentially competitive c_{ethene} at high j_{AEM}. The predicted c_{ethene} falls below or close to the current market price in the whole range of j_{AEM} if FE_{C2H4} > 80%. Clearly, at lower FE_{C2H4}, the range of target j_{AEM} gets progressively narrow, yet competitive c_{ethene} can still be achieved in case 3. Furthermore, at a FE_{C2H4} of ~100% (**FIG 4**, ASR = 3 W cm^2, j_{AEM} = 1 A/cm^2), the energy efficiency of the electrochemical process is evaluated as ~28%. Any optimization of energy efficiency (e.g. decrease in ASR) would lower the operation cost of the AEM, thus minimizing the predicted c_{ethene}.

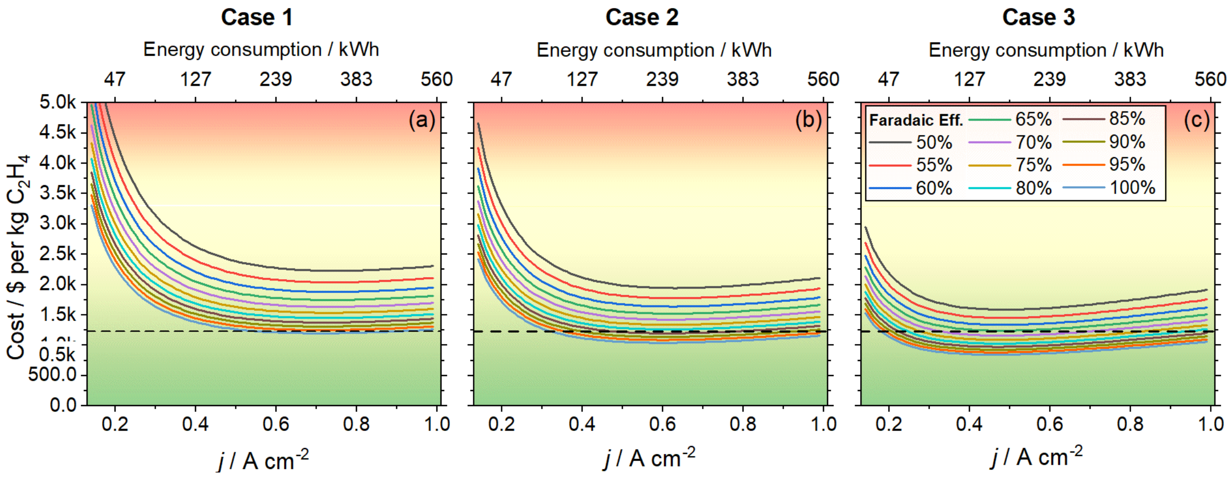

FIG 4: production cost of C_2H_4 using the modelled set-up for CO_2 capture and electrolysis. (a) – (c) Effect of varying faradaic efficiency and current densities for case 1 – 3. The horizontal dashed line represents the market price of C_2H_4 in 2022. The Faradaic efficiency for CO_2 to C_2H_4 conversion was fixed at 65% and the set-up is assumed to operate for 50,000 hours. The cost is referenced to the production of 1 mt of C_2H_4 and cost of electricity was fixed to 0.02 $/kWh.

Cell aging. Considerations about the durability and stability of electrochemical devices are included in this study, especially given the hefty contribution of the capital cost to the overall c_{ethene}. A model for the decline in performance due to cell aging is restricted our model to the AEM. For a conservative estimate, we will assume complete disposal of the reactor at the end of its lifetime. On the other hand, case 3 is considered for the capital cost, and c_e is set to both 0.02$kWh (**FIG 5(a)** and **(c)**) and 0.01$kWh (**FIG 5(b) and (d)**). End of life for the reactor is considered equivalent to a decline of 10% in efficiency coinciding with 50,000 hours of service. **FIG 5** illustrates the total profit as a function of time and intended product price. Two cycles are illustrated in the Figure, with the green areas corresponding to regions wherein the profit approaches the total product cost (*i.e.*, 0 $ profit). For **FIG 5(a) and (b),** net positive profit over two cycles is only possible if the intended price of ethylene greatly exceeds its current market price. As the price of electricity is decreased to 0.01$/kWh, the c_{ethene} landscape drastically changes and returns an uphill trend even at a price lower than 1,000$/mt of ethylene. At the current market price of ethylene, a run time of ~20,000 hours is sufficient to amortize the capital investment and operation costs. The estimated lifetime of the reactor is set to obtain conservative c_{ethene} values and is somewhat shorter than that used in other modeling studies (e.g., 7-10 years of service).[26] Extension of the lifetime would clearly return even more favorable scenarios.

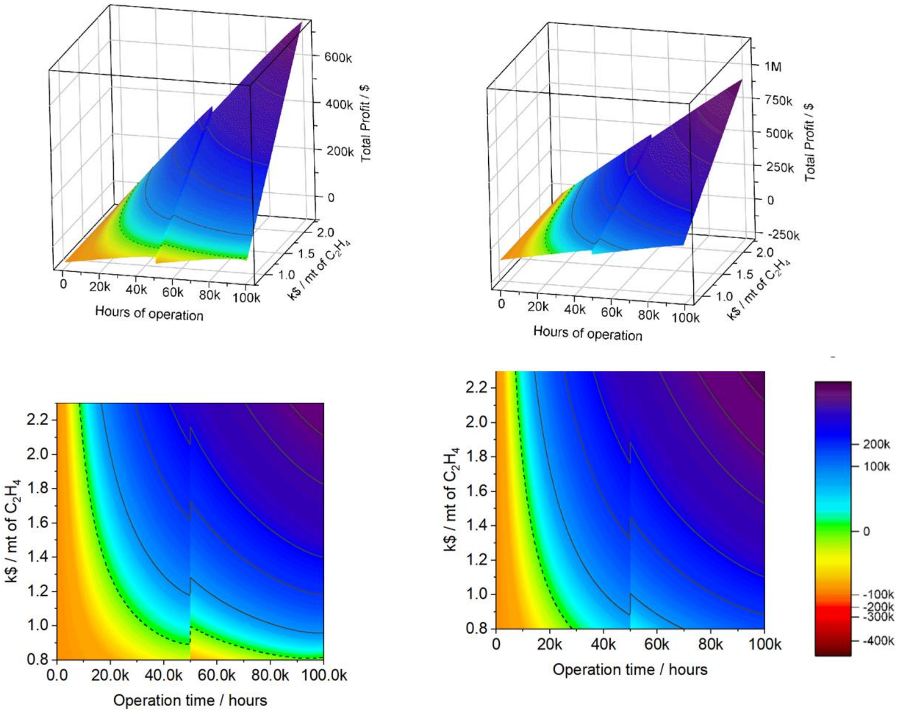

FIG 5. Total profit for production of ethylene using the modelled set-up for CO_2 capture and electrolysis, accounting for degradation of cell performance over operation time. The profit is dictated by the energy consumption and projected market price of C_2H_4. (a) and (c) 3D surface and

its 2D projection for case 1 (cost of electricity 0.02 $/kWh). (c) and (d) 3D surface and its 2D projection for case 1 (cost of electricity 0.01 $/kWh).

3.3 Technology Gap Analysis and general discussion

This TEA study reports promising results regarding the economic feasibility of CO_2ER using a state-of-the-art set-up of electrochemical devices. For competitive production cost of ethylene, we found that high, yet realistic performance of the key reactors is required together with competitive prices of electricity. Our TEA considered production of ethylene without accounting for energy and cost required for downstream processes. An example could be the purification and separation of ethylene from unreacted CO_2 or co-products. According to recent modelling studies, however, energy for ethylene separation may be approximately 3.0-3.2 kWh/kg of product. When compared to the energy requirement to operate the set-up, this value only accounts for small percentage and could therefore be included in the adjustment factor used in our estimate.

Even if this study focuses on the operation of the AEM as the reactor of highest impact on the c_{ethene}, optimization of the capture and SOEC may offer some margins for cost minimization. Besides the economic aspects, it should be considered that when coupled to renewable energy sources, the set-up described here could offer promising approach for environmental mitigation. If one considers that the average carbon intensity of wind electricity of ~11 g of CO_2/kWh[24], then operation of the integrated set-up would correspond to ~0.8 kg of CO_2e emitted per kg of ethylene produced or ~1.3 kg of CO_2 utilized. Although this estimate is far from being a systematic Life Cycle Assessment, it suggests that operation in tandem of the reactors may aid reduce CO_2 emissions from anthropogenic sources. More comprehensive environmental assessment will be carried out soon on this setup. In the meantime, a look at the future landscape of energy production suggests that a larger-scale deployment of renewable sources is imminent. This may allow even more favorable scenarios for large-scale application of the electrochemical CCU technologies, to maximize both their environmental and economic benefit and greatly contribute to the transition to cleaner, carbon-neutral economies.

ACKNOWLEDGMENTS

We would like to thank the Department of Energy for the support of this work by the Office of Fossil Energy and Carbon Management under DE-FE0031919 and the Advanced Manufacturing Office of the Office of Energy Efficiency and Renewable Energy under DE-EE0009421.

References

1. EIA. (2021). *Monthly Energy Review*. Total Energy .
2. Mimura N. Sea-level rise caused by climate change and its implications for society. Proc Jpn Acad Ser B Phys Biol Sci. 2013;89(7):281-301. doi: 10.2183/pjab.89.281. PMID: 23883609; PMCID: PMC3758961.
3. Pidcock, S. Connors, J.B.R. Matthews, Y. Chen, X. Zhou, M.I. Gomis, E. Lonnoy, T. Maycock, M. Tignor, and T. Waterfield (eds.)]. Cambridge University Press, Cambridge, UK and New York, NY, USA, 616 pp., doi:10.1017/9781009157940.
4. IPCC, 2018: Global Warming of 1.5°C. An IPCC Special Report on the impacts of global warming of 1.5°C above pre-industrial levels and related global greenhouse gas emission pathways, in the context of strengthening the global response to the threat of climate change, sustainable development, and efforts to eradicate poverty [Masson-Delmotte, V., P. Zhai, H.-O. Pörtner, D. Roberts, J. Skea, P.R. Shukla, A. Pirani, W. Moufouma-Okia, C. Péan, R
5. Battelle. (2023). *Battelle*. Carbon Capture and Storage FAQs.
6. Rao, M., Fernandes, A., Pronk, P., & Aravind, P. v. (2019). Design, modelling and techno-economic analysis of a solid oxide fuel cell-gas turbine system with CO2 capture fueled by gases from steel industry. *Applied Thermal Engineering*, *148*, 1258–1270. https://doi.org/10.1016/J.APPLTHERMALENG.2018.11.108
7. Alexander Stern, S. (1994). Polymers for gas separations: the next decade. *Journal of Membrane Science*, *94*(1), 1–65. https://doi.org/10.1016/0376-7388(94)00141-3
8. Aravind, P. v., & de Jong, W. (2012). Evaluation of high temperature gas cleaning options for biomass gasification product gas for Solid Oxide Fuel Cells. *Progress in Energy and Combustion Science*, *38*(6), 737–764. https://doi.org/10.1016/J.PECS.2012.03.006

F. Task 7. A Systematic Life Cycle Assessment of the Electroconversion of Carbon Dioxide

Abstract. In this study, we report a cradle-to-gate life cycle assessment of assembling and operating an electrochemical cell for conversion of carbon dioxide (CO_2) to formic acid. This process is followed by product separation *via* liquid-liquid extraction. The results suggest that cell operation yields the highest environmental impact *cf*. other processes. Parametric studies were performed to identify conditions that minimize the environmental impact. It was found that:

(i) stability/durability and current density/cell voltage have high impact on the carbon emissions;
(ii) the optimal parameters include stable operation for at least 4,000 hours at (ultrahigh) current densities (0.50 - 1.00 A cm^{-2});
(iii) through use of renewable energy sources zero carbon emissions may be achieved only if high cell performance conditions are met; and
(iv) the cumulative carbon emissions were predicted during the entire life cycle of the system (4,000 hours), while modelling cell aging and corresponding decline in performance. Here, the use of renewable energy is of outmost importance to achieve climate change mitigation.

KEYWORDS: Carbon utilization process, Environmental analysis, Life cycle assessment, Climate Change Mitigation

Table 1. Acronym Reference Table

Acronym	Definition
EPA	Environmental Protection Agency
GHG	Greenhouse Gas
CO_2ER	Carbon Dioxide Electrochemical Reduction
LCA	Life Cycle Assessment
LCIA	Life Cycle Inventory Analysis
FA	Formic Acid
CCU	Carbon Capture and Utilization
NETL	National Energy Technology Laboratory
GWP100	Global Warming Potential (100 years)
Bi-MOF	bismuth-based metal-organic framework
PG	Power Grid

1. Introduction

Over the past few decades, an increasing anthropogenic emission of greenhouse gases (GHGs), especially CO_2, has led to profound consequences for both human well-being and the environment[1–4] (*v*. **Section S1** of Supplementary Information). Such negative ramifications have driven much of the current research efforts towards the development of technologies to reduce GHG emissions and mitigate their environmental consequences. Among various approaches, electrocatalytic reduction of CO_2 (CO_2ER) represents a promising route to promote conversion of CO_2 to useful chemicals, [5–13] which, coupled with the use of electricity from renewable energy providers, could represent a green approach to utilize previously captured CO_2. Despite this, construction of electrochemical cells for CO_2ER and their operation are complex processes, which may require sophisticated synthetic procedures or use of methods and technologies which may themselves come with a non-zero environmental impact. Clearly, environmental assessment of CO_2 utilization technologies requires further exploration, as only a handful of studies has been reported so far.[14–28] Previous studies have successfully implemented a life cycle assessment (LCA) approach to evaluate the environmental benefits of using CO_2ER technologies to produce formate (or formic acid), or other relevant products.[15–26] Typically, the formation of CO_2ER products is main focus in such studies, however, upstream processes and downstream product separation need accounting as they may require considerable energy consumption.[17,29] A recent study by Nabil *et al*.[17] reports a comparative LCA which analyses the conversion of CO_2 to an array of eight different products, considering both their generation and separation to obtain high purity chemicals. In their assessment, most of the environmental impact was related to the energy requirement, which was majorly attributed to the conversion of CO_2 to such products and their separation processes. Interestingly, the global warming impact was found to depend on the CO_2 conversion product.

To the best of our knowledge, there is still a lack of comprehensive, systematic LCA studies aimed at evaluating the environmental effect of tuning various experimental and operation parameters (*v*. **Table S1** in **Section S2** for survey of previous reports). The interplay between manufacturing and operation of CO_2ER technologies also requires further exploration. In particular, it is paramount to investigate how optimization of energy-to-product conversion, stability and durability of CO_2ER technologies can aid reducing the net carbon emissions, since these factors are potentially highly impactful under health and environmental perspectives. Previous reports have investigated the production of various useful chemicals from CO_2ER, while also including some sensitivity analysis or the effect of the energy source to some extent.[14–28] However, since different frameworks and methods may yield to substantially different results, thus making comparison between studies rather challenging. Thus, it is paramount to provide a unifying, comprehensive study, in which these different aspects are explored using the same approach and consistent methodology. Furthermore, evaluation of manufacturing procedures should be as comprehensive as possible.

For this purpose, a detailed cradle-to-gate LCA was carried out. Firstly, a comprehensive assessment was used to investigate the impact of CO_2ER technologies using a baseline model. We focused on evaluating resource and energy requirements for CO_2ER and all related energy-intensive upstream and downstream processes. As such, the aim is to evaluate the environmental impact of the entire electrochemical cell lifetime, including manufacturing or synthesis processes, cell operation and separation procedures to obtain a commercial grade product, here taken as formic acid (FA). The choice of the product is justified by various motivations, including its numerous applications in many industrial processes and potential of being used as hydrogen carrier and for fuel cell applications. Furthermore, compared to other CO_2ER products, FA has a high molar mass per electron transfer, which is energetically preferable for production by CO_2ER.[17] Secondly, an important objective of this LCA is to complement the existing reports by carefully evaluating various factors, *i.e.*, operational variables, which may affect most heavily the outcome of the analysis. Therefore, a parametric analysis was performed on the model; the overarching goal is to identify the set of conditions which offer a good match and/or compromise between product output, energy requirements, and minimal environmental impact. Finally, we performed an overall evaluation of the cumulative global warming impact over the whole lifespan of the cell, by factoring the decline in energy efficiency as the electrochemical device ages. The results of this LCA study are expected to provide valuable guidance in the development of CO_2ER technologies, especially regarding ways in which, not only their performance, but also the environmental benefits of their implementation can be maximized. This will provide insights to favour the transition to more sustainable, carbon neutral technology.

2. Methodology and Framework

The methodology, mathematical relationships, and life cycle inventory for this study are described in detail in **Sections S3 and S4** of the Supplementary Information, alongside the goal and scope of the study. Briefly, the LCA was performed using the openLCA software in conjunction with the freely available databases.[30,31] The Tool for the Reduction and Assessment of Chemical and other environmental Impacts,[32–34] **(**TRACI 2.1**)** was selected as Life Cycle Inventory Analysis (LCIA) method (*v*. Section S5.1).

The goal of the study is to evaluate the environmental impact of manufacturing and operating an electrochemical reactor for CO_2ER and identify the optimal circumstances under which the impact can be minimized. To this end, we consider the interplay between upstream manufacturing processes and the operation of the CO_2ER technology. We include an extremely extensive inventory to ensure that the description of manufacturing processes is as accurate as possible. The upstream processes will then be linked to the main process of interest for the model system, e.g., operation of the reactor. An additional downstream process is added for product purification, to obtain commercial grade FA, *e.g.*, at least 85% purity of the product in its acidic form, rather than FA or its conjugate base (formate) in dilute aqueous solution. Details on the operation and purification unit processes are reported in Section **S4.2 Operation processes** of the Supporting Information. On the model system, the overall environmental impact and the single contributions by source will be evaluated using systematic parametric studies.

This differs from what is currently found in literature as currently, most studies focus on the operation of the electrochemical cell alone. Although this is a sensible conclusion for the operation of the cell over long periods it does not cover periods closer to the production of the cell.

In the framework of this study, the environmental impact can be assimilated to a multidimensional surface which is a function of different variables, including current density/cell voltage, durability/stability etc. The parametric studies correspond to scans performed across different variables. While scanning such variables at finite intervals, the potential impact is predicted at each step to identify a local minimum point or a good compromise between the impact and the product yield. We proceed as it follows. At first, we set variables to describe a baseline model system (**3.1 Baseline Model**). We then perform a single-variable scan along the projected lifetime of the cell and evaluate the environmental impact at each selected operation time/lifetime (**4.1 Stability and Durability**). Based on the results, the variable is fixed to its optimal value. This optimal value is determined by finding the lifetime profit of the system over 50,000 hrs. This is done by finding the net profit from ethylene at any current density with the highest net profit being the optimal point. This is done due to the fact that increasing the current density will often create a larger profit that will offset the increase in the price of production. Subsequently, we simultaneously vary the cell voltage and current density to identify how the potential impact is impacted by these two parameters. This scan is performed using an empirical approach, wherein the relation between current density and voltage is defined by experimentally measured data.

Finally, to the best of our knowledge, no previous LCA study has investigated the decline in performance as a function of operation time (*e.g.*, cell aging). Our model to address this theme is reported in **Section S.4.3** (Supporting Material) and **4.4 Cumulative Life Cycle Emissions** (main text) and shows the cumulative impact along the whole life cycle of the reactor.

3. Results and discussion

In the following sections, the LCIA results and their interpretation will be discussed. We will initially focus our attention on the analysis of a baseline system, focussing on the GWP100. We will then discuss parametric studies. It is worth to remind that the GWP100 provides a good tool for estimating the carbon (or in general, GHG) emissions, and is therefore particularly relevant to this study. For simplicity, we will often refer to the GWP100 as GHG emissions in the following text. All results will be referenced to the functional unit of 1 kg of FA produced upon CO_2ER. A schematic, simplified version of the model system is illustrated in **Figure 1**, which shows the most relevant upstream processes linked to the process of interest, *i.e.*, the operation of the electrochemical assembly for CO_2ER. Following cell operation is the product separation process, ('formic acid separation').

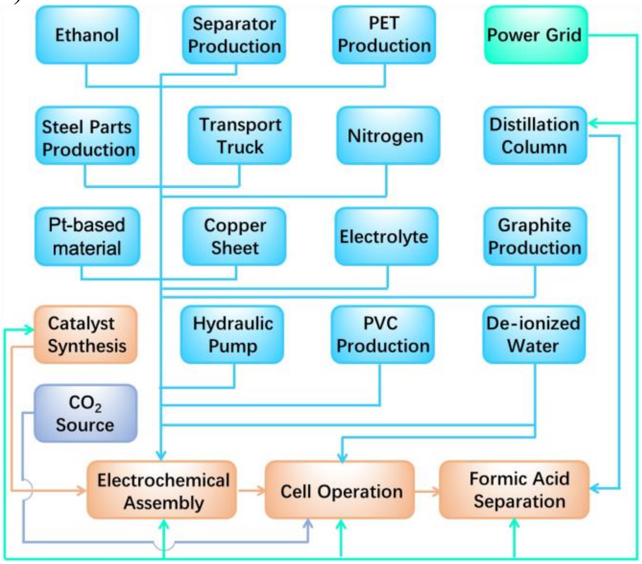

Figure 1: Collapsed model graph of the model system for CO_2ER.

The power grid (PG) or energy provider in general (v. **Section S3)** is displayed explicitly as connected to a subset of unit processes, which were modelled by the authors. This PG has a carbon intensity of about 0.467 kg of CO_2e per kWh of electricity produced. This value may be relatively large compared to the carbon emissions of electricity produced in many US states or European countries. It is however representative of the average carbon emissions from electricity worldwide, as of 2019.[35] Other processes in **Figure 1** also require energy providers but, for conciseness and clarity, these are not explicitly displayed.

3.1 Baseline Model

Overview. A simplified models and schematics of the CO_2ER system are shown in **Figures S1** and **S2** of the Supporting Information. For the first assessment, the results were computed by setting operational parameters as explained in **Section S4.2**, *i.e.*, 4,000 hours cell operation time at 1.00 A cm^{-2} (at 5.48 V),[36] and 255 g/hour recovery of commercial grade FA upon liquid-liquid extraction.[37] A general analysis of the environmental impact for various categories is reported in **Section S5.2**; in the text below, we will focus on the GHG emissions.

Emissions. The analysis of GWP100 predicts ~5.5 kg of CO_2e for 1 kg of FA produced (0.861 kg of CO_2 utilized). Hence, positive, net emissions of GHGs are predicted, at least when a generic electricity provider is used. More detailed impact results are reported in **Table 2** and **Figure 2**, which illustrate the absolute and percentage contributions to the GWP100 of the various processes.

Table 2: Detailed impact results of LCIA for GWP100 impact category for the base model system

Process	**kg CO_2 e.q**	**Contribution**
Cell operation (PG)	3.235	59.00%
Separation (PG)	1.621	29.57%
CO_2 Source	0.343	6.25%
DI H_2O production	0.005	0.08%
Reactor Preparation	0.085	1.55%
Separation set-up	0.194	3.54%

Hence, the energy consumption for cell operation and product separation account for most of the GHG emissions. Manufacturing of the electrochemical and extraction/distillation assemblies accounts collectively for 5.09% of the overall GHG emissions, with processes related to the preparation of the reactor only accounting for 1.55% of the impact. The larger contribution of the separation apparatus is due to comparatively higher quantities of required materials, including glass and metal components. These findings are in qualitative agreement with previous reports of CO_2ER and other energy-related technologies, with the values reported here suggesting higher GHG emissions.[15–17,38–40] The higher GHG emissions predicted in this study may be rationalized by the selection of more carbon intensive power grid *cf.* studies which invoke more optimistic scenarios, and/or the use of a more extensive inventory of materials.

Clearly the nature of energy provider has a high impact on the GHG emissions. If we break down the impact of cell operation (PG) in various energy sources (**Figure 2(b)**), the highest emissions arise from coal-based power generation (32.5%) although it accounts only for 22% of the total electricity produced. This is followed by natural gas (23% of the GWP100), as it constitutes the largest source of electricity. Although typically associated with higher impact in other categories (**Section S5**), nuclear power contributes by merely 0.7%, as it is a low carbon emitting source. Renewable energy sources, which account for ~20% of the used PG mixer, are collectively responsible for just above 2% of the overall GHG emissions. Clearly, decreasing the fraction of coal-based power, at least for cell operation, can help reduce GHG emissions by nearly a third of the overall value.

This is a clear-cut illustration of the importance of using clean electricity for operation purposes, as a first step towards lower carbon emitting technologies. Since net positive emissions of GHGs are predicted, the following sections will present exploratory studies aimed at identifying ways in which these emissions can be minimized. This will be done by scanning or varying selected operation parameters or conditions to ensure minimal environmental impact associated with the production of this valuable chemical by CO_2ER.

To identify the parameters of highest environmental impact, a parametric study was performed on the model system. Details of the analysis are included in **Section S5.2** of the Supporting Information, which also reports a general description of the impact for various categories. In the text below, we will focus on how varying different parameters affects GHG emissions.

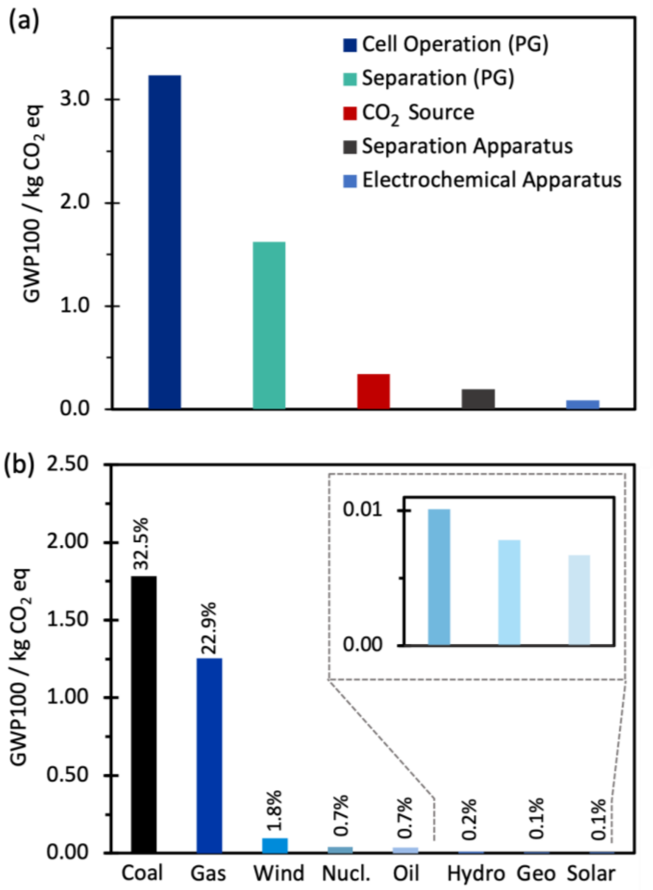

Figure 2: GWP100 impact results. (a) contribution of various processes, (b) Contribution of various power generation sources. The inset shows an enlarged view of the contributions from Hydrothermal, Solar and Geothermal Electricity.

4. Parametric Analysis

4.1 Stability and Durability

Overview. The stability and durability of the electrochemical cell represent important factors which can affect both its economic and environmental feasibility.[16,41] Thus, in this study, we explore the implications that varying the cell lifetime has on the environment and global climate impact. To this end, the overall operation time of the cell was set to discrete values between 24 and 40,000 hours; subsequently, assessment of environmental impact was performed at the various points. To first approximation, all other parameters are kept constant: in the last section of this study, we will assess how decline of cell performance throughout its lifetime can affect environmental impact.

GHG emissions. The overall GWP100 as a function of the operation time is shown in **Figure 3(a)**. The GHG emissions are predicted to decrease sharply with the increase of cell lifetime. These results are broken down into different contributions, arising from various processes in **Figure 3(a)** and **3(b)**. Manufacturing the two assemblies accounts for over 80% of the overall GHG emissions at limited cell lifetimes. Particularly, assembling the extraction/distillation apparatus is associated by far with the highest impact (**Figure 3(b)**). As our quantitative reference is the production of 1 kg of FA, when the operation time increases, contributions of manufacturing the assemblies decreases at the same time, until becoming negligible at 40,000 hours of operation. Consequently, the impact associated with cell operation and product separation (energy consumption) becomes dominant at longer lifetime (> 250 hours). This is true since the faradaic efficiency, current density and other parameters are not changed. As the GHG emissions results appear to approximately plateau around 4,000 hours, further extension of the cell lifetime is not expected to greatly affect the emissions.

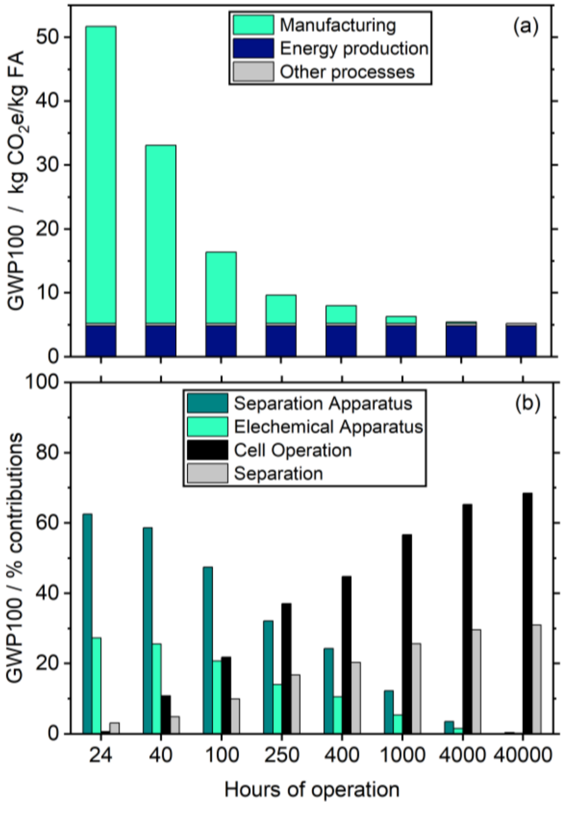

Figure 3: (a) Carbon emissions at different operation time; the contributions of manufacturing the apparatuses, energy production and other processes are shown, (b) percentage contributions of PG manufacturing of the apparatuses *vs.* operation processes.

In view of these results, we therefore reckon that 4,000 hours (or longer) of operation at the set conditions could be considered an appropriate time to amortize the environmental cost of production of materials thus providing lower, although not negligible global warming impact. This value (4,000 hours) will therefore be set as the 'target' durability of the cell at optimal conditions for the following investigations, in the effort of identifying the conditions which will lead to the lowest GHG emissions. As our final consideration, these results are in qualitative agreement with a previous study by Rumayor *et al.*,[16] wherein the authors estimated that a lifetime of cathode materials of 210 hours is enough for amortizing the environmental effect of cathode fabrication. The discrepancy with the current results may arise from the use of a more extensive inventory, consisting of all major components to construct both the reactor and separation apparatus. This is expected to increase the overall environmental impact of manufacturing and preparation processes. As a final consideration, in the most general terms, durability and lifetime of the technology is always an important factor to amortize the cost of manufacturing processes. However, the dependence maybe be process-specific and, in the case of CO_2ER appears to be product-specific. As some products of CO_2ER have much lower molar mass per electronic transfer, energy requirements for CO_2ER may dominate the impact even at short lifetimes in such cases. This implies that reducing environmental impact of manufacturing processes may become a less pressing issue, compared to optimization of other operational parameters and conditions (e.g., cell voltage, resistance, faradaic efficiency, energy efficiency etc.).

4.2 Current Density and Cell Voltage

Overview. The effect of varying the current density j (and associated voltage V) is explored by setting this variable to discrete values between 0.25 and 1.50 A cm^{-2}, while maintaining the other parameters unvaried. The energy consumption required to perform CO_2ER at various j values (and V) this was calculated in accordance with previous studies on analogous electrochemical devices[36] and is explicitly discussed in **Section S4.2.** The energy required for ancillary equipment was also accounted for but was set to exclusively depend on the operation time, here fixed to 4,000 hours. The product is assumed to be collected and separated by liquid-liquid extraction. The rate of recovery of the final product was not changed. The following analysis will assume that the faradaic efficiency does not change in this (wide) range of current densities.

GHG emissions. The GWP100 results as a function of j are shown in **Figure 4**. Particularly, **Figure 4(a)** shows the cumulative GHG emissions. An initial, modest decrease in the GHG emissions is observed with increasing j (up to 0.75 A cm^{-2}), followed by a small, but steady increase. The initial decrease is attributed primarily to lower contributions arising from manufacturing the assemblies, as seen in both **Figure 4(a)** and **4(b)**. However, this effect is outrun by the larger demand in energy for CO_2ER at higher current densities, wherein operation of the electrochemical cell becomes dominant. By contrast, since the separation of the product is assumed to occur at the same rate, the contribution of this process stays constant or, in terms of percentages, it slightly decreases at high current densities. Under the environmental perspective, it is therefore inferred that operating at current densities of 0.50-1.00 A/cm^2 may be favourable and sufficient to (i) render manufacturing processes negligeable and (ii) limit the environmental impact of energy consumption for CO_2ER. In general terms, aiming for the higher end of this range could represent a good trade-off between lowering GHG emissions and obtaining good product output. The latter is necessary for larger-scale applications, and techno-economic analysis also suggests that current densities exceeding 1.00 A cm^{-2} (lifetimes > 30,000 hours) are required for industrial deployment of electrolysis technologies.[42] As far as the use of the generic PG is considered, very high j values do not seem compatible with efforts aimed at minimizing the environmental impact. Furthermore, operation at high j may have an impact on the stability/durability of the cell materials. In this context, lower *j* may be advisable for decreasing material degradation within the cell, thus extending the cell lifetime.

Our final consideration is that the dependence of the GHG emissions on the current density is related to the cell performance and energy efficiency. In this study, we refer to a recent publication[36] to model how the energy requirements for CO_2ER change upon varying *j*. In other words, this part was evaluated based on available experimental data. The details in the trend and specific values for GHG emissions may vary to some extent depending on the data used for the model. However, in general, it is reasonable to assume that, at higher current densities, energy efficiency tends to decrease. It can then be inferred that, despite higher products output, the global climate impact is bound to increase (*v.* **Figure 4** and **Figure S3**). It is our understanding that a dependence on the product of CO_2ER may also be observed. This is a manifestation of the fact that different products will exhibit substantially different molar masses per electron transfer. In these cases, the interplay between product output and energy requirements may be different.

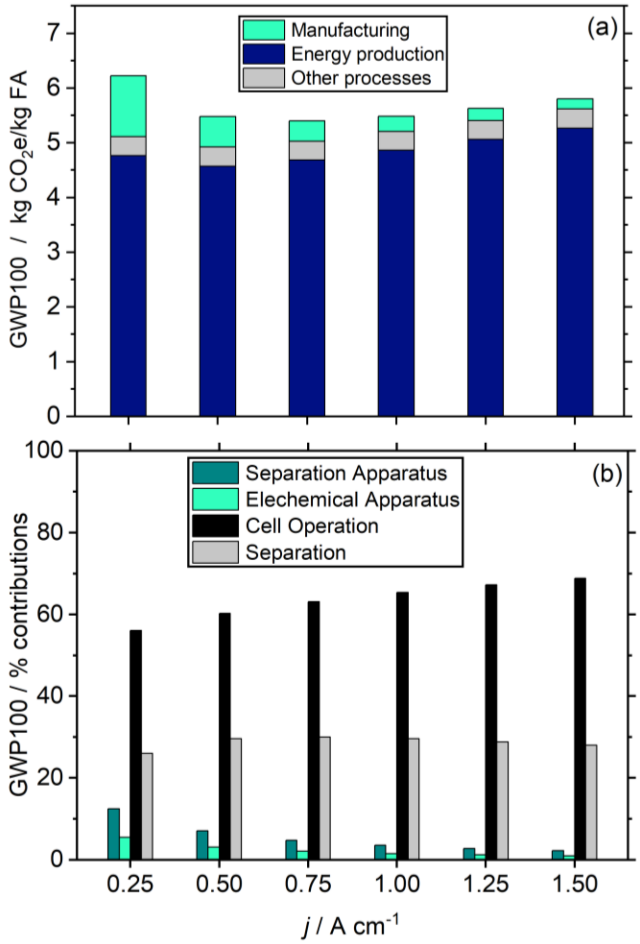

Figure 4: Carbon emissions at different current densities; the contributions of manufacturing, energy production and other processes are shown, (b) percentage contributions of PG manufacturing of the apparatuses *vs.* operation processes.

4.3 Role of Renewable Energies Sources

Overview. The results presented in the previous sections show that the energy usage, especially for CO_2ER, is the dominant factor affecting the environmental feasibility of the CO_2ER technologies modelled in this study. As such, we investigated the role that renewable energy sources may play in favouring transition to lower carbon emitting technologies. To do this, we selected five different electricity providers within the NETL CO2U Database version 2.0[31], namely the (adjusted) PG and Nuclear electricity (as non-renewable energy providers), Solar Thermal, Hydrothermal and Wind as renewable energy sources. The operation time and current densities were varied in turns and the results computed at each point.

GHG emissions. Figure 5(a) shows a comparison between the GWP100 estimated for the five electricity sources at three current densities (0.25, 0.50 and 1.00 A cm^{-2}) and 4,000 hours of operation; the dashed horizontal line represents the mass of CO_2 consumed per production 1 kg of FA (0.861 kg); we can approximately consider this as the threshold at which zero carbon emissions are achieved. The use of PG results in 2-5 times higher GHG emissions *cf*. the other energy sources, some which return (close to) zero GHG emissions at 1.00 A cm^{-2}.

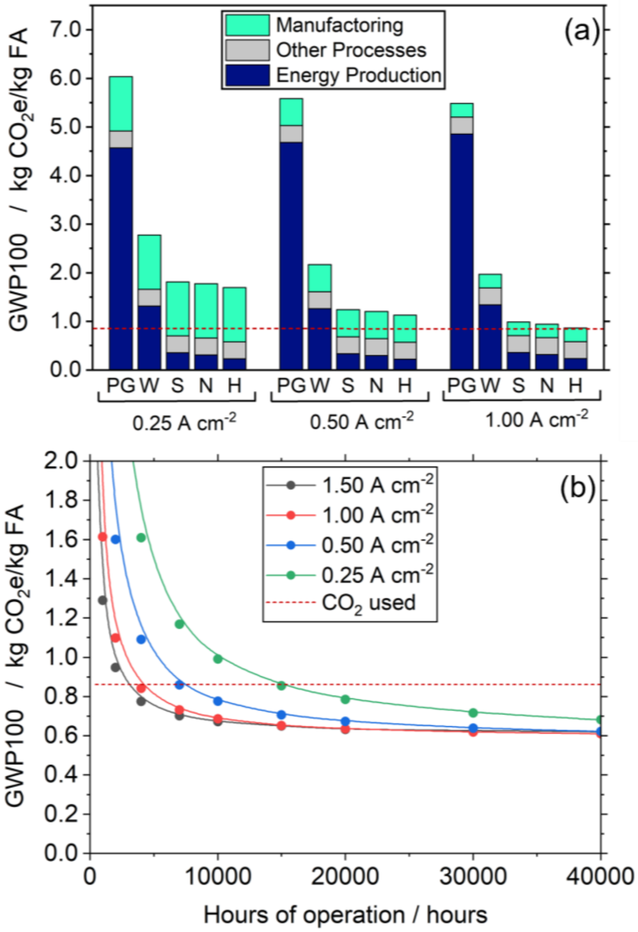

Figure 5: GHG missions for various energy sources at three different current densities. (b) GHG emissions as a function of current density and lifetime when the hydroelectric energy provider is used for cell operation and product separation. Horizontal dashed line represents the net 0 emission threshold.

Figure 5(b) shows the estimated GHG emissions as a function of varying both *j* and durability of the cell. The emissions consistently decrease both at higher *j* and longer cell lifetime when a clean, renewable energy source (hydrothermal) is used to operate the cell and separate the product. Our predictions suggests that very long lifetimes, exceeding 15,000 hours, are required to achieve zero or negative GHGs emissions at current densities equal or lower than 0.25 A cm^{-2}, while 3,000-4,000 hours are requiring at higher *j* values. When compared to the use of PG, the renewable source (hydropower) shows a different trend of GHG emissions with *j*. This is explained if one considered that the environmental impact of manufacturing procedures decreases higher *j* values, and, at the same time, the impact of higher energy consumption is counterbalanced by higher yields of FA. Thus, it is apparent that operation at ultrahigh *j* could yield higher environmental benefits. However, these benefits seem to level-off at ~1.50 A cm^{-2}. Under a more practical perspective, this implies that clean energy favours minimum environmental impact at conditions which are more compatible with those invoked by technoeconomic analysis.[42] Under the perspective of their applicability, this also means that stability and durability of the cell materials becomes a less environmentally compelling issues when compared to the use of the generic PG.

In conclusions, the results in **Figure 5** confirm that use of renewable energy sources,[15,43] as well as nuclear-based power generation, could represent a viable route to obtain considerably lower or even negative GHGs emissions in electrolysis and/or carbon utilization technologies, while, at the same time, maximize the use of intermittent renewable energy sources.[15,23,43,44]

4.4 Cumulative life cycle emissions

Overview. The primary aim of this section is to explore how the life cycle GWP100 varies with the decrease efficiency as a function of the operation time. A higher operation voltage, owing to the degraded electrochemical cell, leads to the lower energy efficiency for constant current or constant FA production. In this framework, we set the output of FA to be constant, while the energy consumption is increasing with increasing lifetime. Details about the model are reported in Section S.6 of the *Supporting Information*. Briefly, we perform the environmental assessment at 100-hour increments, for a total of 4,000 hours of operation. The approach used in this portion of the study differs from the previous section in that the functional unit was not restricted to 1 kg of FA produced. Rather, the assessment was performed by considering the total mass of FA produced during each time increment, with consequent consumption of CO_2 *vs*. emissions of GHGs.

GHG Emissions. **Figure 6** illustrates the incremental and cumulative GHG emissions when the PG (**Figure 6(a)** and **6(b)**), and hydrothermal provider (**Figure 6(c)** and **6(d)**) are used for operation and product separation. Contributions of preparation of the set-ups are accounted once and are distributed throughout the entire lifetime of the cell.

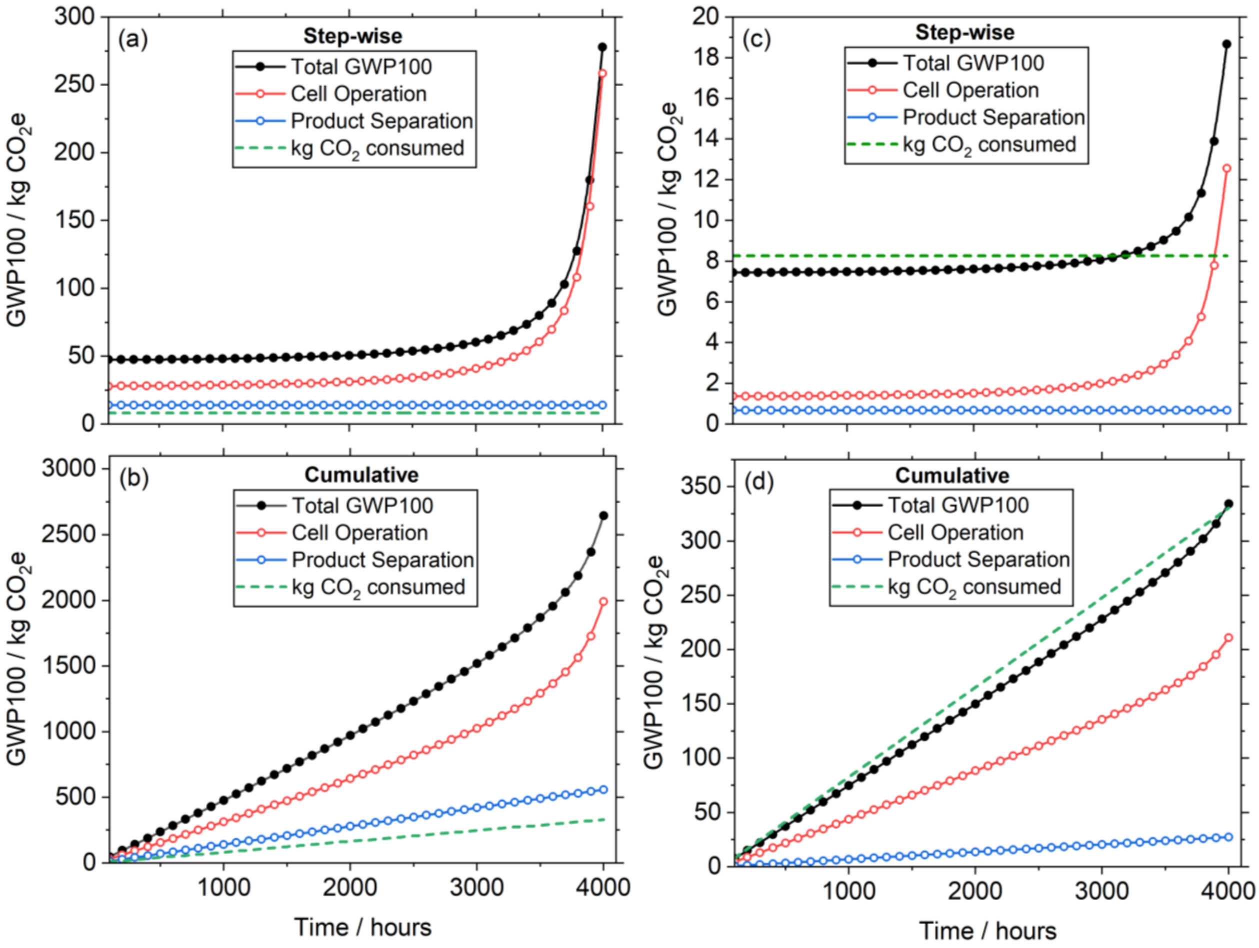

Figure 6: (a) GWP100 results and contributions of different processes at 100-hour time intervals up to 4,000 hours, (b) cumulative GWP100, and mass of CO_2 converted a at the above conditions. The electricity provider is a generic power grid representative of the US modern grid.

As observed in **Figure 6(a)** and **6(b)**, the GHG emissions undergo a steep increase after 3,000 hours of operation, because of the higher energy consumption. It is clearly shown that, GHGs emissions overwhelmingly outweigh the mass of CO_2 utilized throughout the lifetime of the cell, thus retuning net positive emissions at all times. When using hydropower (**Figure 6(c)**), the GHG emissions are considerably lower *cf.* the mass of CO_2 utilized. Clearly, this is ascribed to a decrease in the contribution of GHG emissions due to the selection of the clean, renewable energy source for cell operation and product separation. The GHG emissions fall below the mass of consumed CO_2, it is observed that utilization of CO_2 upon CO_2ER. At the beginning of the cell lifetime, it is estimated that a total of ~7.4 kg of CO_2e is produced across a 100-hour operation time interval, while ~8.3 kg of CO_2 is being consumed. Only at lifetimes longer than 3,000 hours the environmental benefits are largely outweighed by the energy consumption. However, the cumulative GHG emissions (**Figure 6(d)**) always remain negative or close to zero. After 4,000 hours, the cumulative GWP100 is calculated to be of ~ 334 kg of CO_2e being emitted, per ~330 kg of CO_2 converted, suggesting, again, that use of a renewable energy source for CO_2ER, coupled to CO_2 capture, can help reducing the global warming impact by a considerable amount, while at the same time obtaining a valuable product.

4.5 Further considerations

As a final consideration, we show three possible case scenarios for our proposed model system. Case 1 is modelled in accord with a recent study exploring the stability and durability of electrolysers for CO_2-to-FA conversion,[36] which we will take as a plausible scenario for state-of-the-art electrolysers developed in laboratory settings. While no additional process was added to the model, the product yield was here rescaled to match Faradaic Efficiency of ~75% across 1,000 hours operation at 0.25 A cm^{-2}. The results represent a lower limit for the GHG emissions, as in complete model, separation of by-products might also require accounting. Case 2 represents a desirable scenario under the environmental perspective, while case 3 is analysed by setting parameters to optimistic values for large scale deployment according to recent techno-economic assessments (highest performance, stability, and durability).[42] The parameters are specified in **Figure 7**, alongside the associated results. Estimating uncertainties for our results is challenging as it requires accounting of possible uncertainty arising from a vast number of measurements as well as possible deviations due to assumptions and approximations made in the model. However, we may consider the results in **Figure 7** as upper and lower limits for GHG emissions in three possible case scenarios; in this instance, the associated GHG emissions show a deviation of about 1.1 kg of CO_2e/kg of FA considering the three values (v. **Section S5.1**) for the PG, or 0.7 kg of CO_2e/kg of FA for hydropower. Interestingly, when using the generic PG lower, the desired conditions for industrial deployment estimated upon techno-economic analysis do not match the optimal conditions for least GHG emitting scenario. This occurs only when a clean energy source (hydropower) is selected for operation of the cell and separation of the final product. In this model, uncertainties related to GHG emissions from energy production/usage may probably come with the largest uncertainty when compared to other processes.

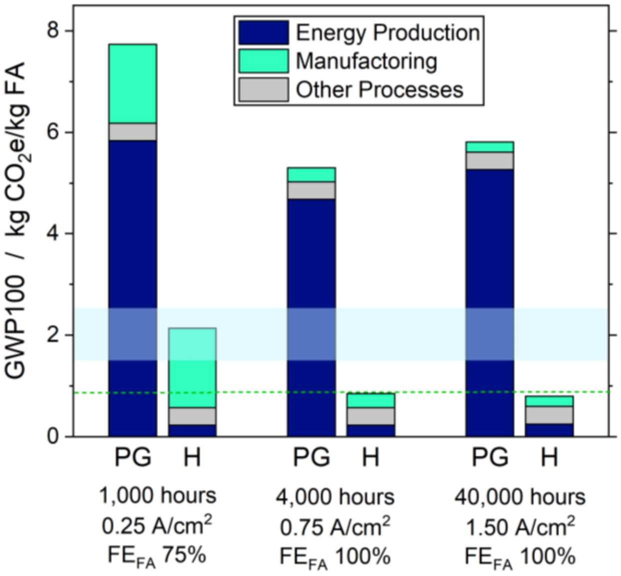

Figure 7: comparison between the GWP100 for Case 1-3 (from left to right)

Furthermore, due to the heavy contribution of power generation, the carbon intensity of the electricity used for operation deserves consideration, since, for set operation parameters, it can affect the GHG emissions to colossal extent. In this context, for instance, the carbon intensity of electricity in European countries as of 2021 ranged from 946 to 9 kg of CO_2e per kWh.[45] As such, when Case 2 is considered, the associated distribution of GHG emissions would span a range between 11.2 to 0.6 kg of CO_2e/kg of FA (**Figure 8**), depending on the geographical location (as well as the time) which is considered for the analysis. In **Figure 8**, we can see that the model system returns net negative emissions in Sweden (below red dashed line), where electricity comes primarily from renewable sources. The average US grid will place emissions in the US in between Ireland and Romania, still below the GHG emissions modelled in this study (grey dashed line).

We did not model any alternative pathways for production of FA, however, LCA of thermochemical methods for FA production have been reported in previous studies,[46,47] which primarily focus on energetic requirements for the process. The light blue shaded areas in **Figures 7** and **8** show the approximate ranges of GHG emissions evaluated for thermochemical methods (without subtracting for CO_2 consumption) according to such previous studies. From this comparison, we may conclude that production of FA by CO_2ER may be a comparably clean process when low carbon emitting electricity is used for cell operation and product separation.

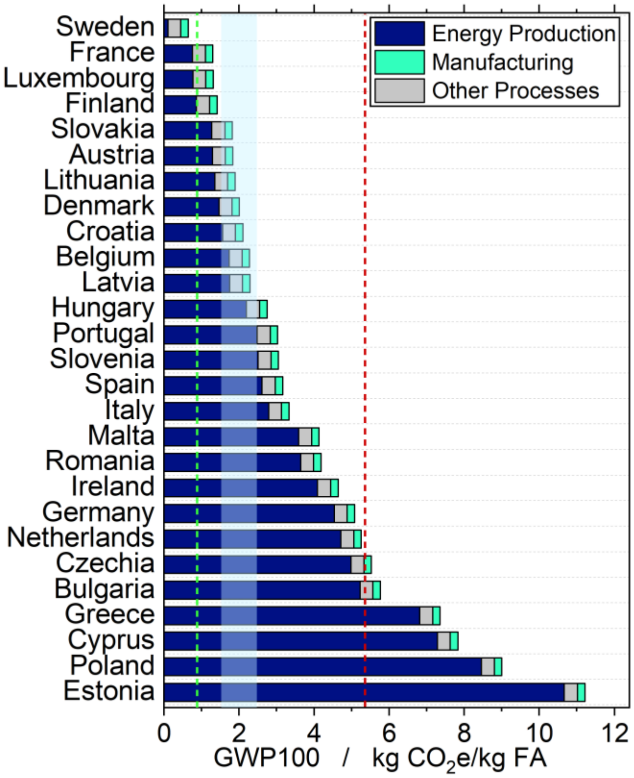

Figure 8: Predicted GWP100 for Case 2 in various European Countries

5. Conclusions and Outlook

We investigated the life-cycle environmental impact of manufacturing and operating an electrochemical cell for reduction of previously captured CO_2 to FA. Purification of the product by liquid-liquid extraction was considered. In many instances, cell operation and product separation were associated with the highest GHG emissions *cf.* other processes. This is attributed due to the high energy consumption required to perform these processes. Parametric studies were performed to evaluate the conditions and parameters which mostly affect the impact results. Furthermore, with the addition of the production of the cell to the life cycle analysis, the optimum minimum operation time can be evaluated. Accordingly, some considerations on the implementation of CO_2ER technologies should be made, as it follows:

(1) The use of clean energy sources is truly essential for cutting down on the emissions of GHGs. However, contrarily to the common conception, clean energy sources cannot be considered *a priori* the solution to obtain net zero or negative emissions. Our studies show that high cell performance, durability and high product yields are still crucial for achieving low GHG emissions, even when clean energy is used for operation processes.

(2) Durability and stability of the electrochemical cell should be a concerning issue when considering the GHG emissions, especially if non-renewable electricity is used. Stability and longevity of the cell assure that environmental impact of manufacturing processes is minimized. In such cases, performing routine operation (CO_2ER and product separation) can be considered the primary cause of environmental impact and optimization of performance can then promote meaningful reduction of GHG emissions. In our study, minimal impact is predicted at cell lifetime equal or longer than 4,000 hours.

(3) The current density and cell voltage govern the interplay between energy consumption and reaction rate. Clearly, low voltages/energy consumption are desired for low environmental impact, while ultrahigh current densities are imperative for large-scale deployment of CO_2ER technologies, according to technoeconomic assessments. For the cell modelled here, we found here that current densities of 0.50-1.00 A cm^{-2} are appropriate for minimizing GHG emissions when the generic PG is used. Using a clean energy source may allow environmental benefits even at higher current densities/energy consumption, such as those desired are useful for industrial application, if durability, and faradaic efficient remain suitable across the whole lifespan of the electrochemical cell.

(4) Recent theoretical studies of CO_2 utilization or comparable energy technologies have employed sophisticated statistical or modelling approaches, some of which rely on artificial intelligence and machine learning, to evaluate performance and optimize large number of operational parameters. Such sophisticated models are largely employed to explore and rationalize the relationships between operation conditions and electrochemical properties of electrolysers or batteries. [48–50] Such methodology has already been applied to LCA for selected applications. [51,52] Implementation and use of such approaches could assist exploration of electrolysers and energy storage technologies, by providing a mean to optimize large number of parameters in time-effective manner and paving the way to more accurate environmental assessment of energy technologies.

ACKNOWLEDGMENTS

We would like to thank the Department of Energy for the support of this work by the Office of Fossil Energy and Carbon Management under DE-FE0031919 and the Advanced Manufacturing Office of the Office of Energy Efficiency and Renewable Energy under DE-EE0009421, and National Science Foundation under NSF-2119688.

REFERENCES

1 EPA, *Inventory of U.S. Greenhouse Gas Emissions and Sinks: 1990-2020. U.S. Environmental Protection Agency, EPA 430-R-22-003*, 2022.

2 IPCC, *Summary for Policymakers. In: Climate Change 2007. The Physical Science Basis. Contribution of Working Group I to the Fourth Assessment Report of the Intergovernmental Panel on Climate Change*, [S. Solomon, D. Qin, M. Manning, Z. Cheng, M. Marquis, K. B. Averyt, M. Tignor, H. L. Miller, (eds)], Cambridge University PressCambridge, United Kingdom and New York, NY, USA, 996 pp., 2007.

3 USGCRP 2017, *Climate Science Special Report: Fourth National Climate Assessment, Volume I*, [Wuebbles, D.J., D.W. Fahey, K.A. Hibbard, D.J. Dokken, B.C. Stewart, and T.K. Maycock (eds.)]. U.S. Global Change Research Program, Washington, DC, USA, 470 pp, 2017.

4 IPCC, *Climate Change 2007: Mitigation. Contribution of Working Group III to the Fourth Assessment Report of the Intergovernmental Panel on Climate Change*, e [B. Metz, O.R. Davidson, P.R. Bosch, R. Dave, L.A. Meyer (eds)], Cambridge University Press, Cambridge, United Kingdom and New York, NY, USA., 851 pp., 2007.

5 R. A. Tufa, D. Chanda, M. Ma, D. Aili, T. B. Demissie, J. Vaes, Q. Li, S. Liu and D. Pant, Towards highly efficient electrochemical CO2 reduction: Cell designs, membranes and electrocatalysts, *Appl Energy*, 2020, **277**, 115557.

6 A. Saravanan, P. Senthil kumar, D.-V. N. Vo, S. Jeevanantham, V. Bhuvaneswari, V. Anantha Narayanan, P. R. Yaashikaa, S. Swetha and B. Reshma, A comprehensive review on different approaches for CO2 utilization and conversion pathways, *Chem Eng Sci*, 2021, **236**, 116515.

7 A. D. N. Kamkeng, M. Wang, J. Hu, W. Du and F. Qian, Transformation technologies for CO2 utilisation: Current status, challenges and future prospects, *Chemical Engineering Journal*, 2021, **409**, 128138.

8 M. D. Garba, M. Usman, S. Khan, F. Shehzad, A. Galadima, M. F. Ehsan, A. S. Ghanem and M. Humayun, CO2 towards fuels: A review of catalytic conversion of carbon dioxide to hydrocarbons, *J Environ Chem Eng*, 2021, **9**, 104756.

9 D. D. Zhu, J. L. Liu and S. Z. Qiao, Recent Advances in Inorganic Heterogeneous Electrocatalysts for Reduction of Carbon Dioxide, *Advanced Materials*, 2016, **28**, 3423–3452.

10 A. Liu, M. Gao, X. Ren, F. Meng, Y. Yang, L. Gao, Q. Yang and T. Ma, Current progress in electrocatalytic carbon dioxide reduction to fuels on heterogeneous catalysts, *J. Mater. Chem. A*, 2020, **8**, 3541–3562.

11 C. Jia, K. Dastafkan, W. Ren, W. Yang and C. Zhao, Carbon-based catalysts for electrochemical CO2 reduction, *Sustainable Energy Fuels*, 2019, **3**, 2890–2906.

12 K. Zhao and X. Quan, Carbon-Based Materials for Electrochemical Reduction of CO2 to C2+ Oxygenates: Recent Progress and Remaining Challenges, *ACS Catal*, 2021, **11**, 2076–2097.

13 J. P. Edwards, Y. Xu, C. M. Gabardo, C.-T. Dinh, J. Li, Z. Qi, A. Ozden, E. H. Sargent and D. Sinton, Efficient electrocatalytic conversion of carbon dioxide in a low-resistance pressurized alkaline electrolyzer, *Appl Energy*, 2020, **261**, 114305.

14 D. Kim and J. Han, Comprehensive analysis of two catalytic processes to produce formic acid from carbon dioxide, *Appl Energy*, 2020, **264**, 114711.

15 A. Dominguez-Ramos, B. Singh, X. Zhang, E. G. Hertwich and A. Irabien, Global warming footprint of the electrochemical reduction of carbon dioxide to formate, *J Clean Prod*, 2015, **104**, 148–155.

16 M. Rumayor, A. Dominguez-Ramos and A. Irabien, Environmental and economic assessment of the formic acid electrochemical manufacture using carbon dioxide: Influence of the electrode lifetime, *Sustain Prod Consum*, 2019, **18**, 72–82.

17 S. Kibria Nabil, S. McCoy and M. G. Kibria, Comparative life cycle assessment of electrochemical upgrading of CO2 to fuels and feedstocks, *Green Chemistry*, 2021, **23**, 867–880.
18 J. B. Greenblatt, D. J. Miller, J. W. Ager, F. A. Houle and I. D. Sharp, The Technical and Energetic Challenges of Separating (Photo)Electrochemical Carbon Dioxide Reduction Products, *Joule*, 2018, **2**, 381–420.
19 X. Li, P. Anderson, H.-R. M. Jhong, M. Paster, J. F. Stubbins and P. J. A. Kenis, Greenhouse Gas Emissions, Energy Efficiency, and Cost of Synthetic Fuel Production Using Electrochemical CO2 Conversion and the Fischer–Tropsch Process, *Energy & Fuels*, 2016, **30**, 5980–5989.
20 P. De Luna, C. Hahn, D. Higgins, S. A. Jaffer, T. F. Jaramillo and E. H. Sargent, What would it take for renewably powered electrosynthesis to displace petrochemical processes?, *Science (1979)*, 2019, **364**, eaav3506.
21 H. H. Khoo, I. Halim and A. D. Handoko, LCA of electrochemical reduction of CO2 to ethylene, *Journal of CO2 Utilization*, 2020, **41**, 101229.
22 P. Yue, Q. Fu, J. Li, X. Zhu and Q. Liao, Comparative life cycle and economic assessments of various value-added chemicals' production via electrochemical CO2 reduction, *Green Chemistry*, 2022, **24**, 2927–2936.
23 J. Wyndorps, H. Ostovari and N. von der Assen, Is electrochemical CO2 reduction the future technology for power-to-chemicals? An environmental comparison with H2-based pathways, *Sustain Energy Fuels*, 2021, **5**, 5748–5761.
24 D. Rojas Sánchez, K. Khalilpour and A. F. A. Hoadley, How sustainable is CO2 conversion to ethanol? – A life cycle assessment of a new electrocatalytic carbon utilisation process, *Sustain Energy Fuels*, 2021, **5**, 5866–5880.
25 P. Yue, Z. Kang, Q. Fu, J. Li, L. Zhang, X. Zhu and Q. Liao, Life cycle and economic analysis of chemicals production via electrolytic (bi)carbonate and gaseous CO2 conversion, *Appl Energy*, 2021, **304**, 117768.
26 A. Somoza-Tornos, O. J. Guerra, A. M. Crow, W. A. Smith and B.-M. Hodge, Process modeling, techno-economic assessment, and life cycle assessment of the electrochemical reduction of CO2: a review, *iScience*, 2021, **24**, 102813.
27 N. Thonemann, Environmental impacts of CO2-based chemical production: A systematic literature review and meta-analysis, *Appl Energy*, 2020, **263**, 114599.
28 X. Wang, M. Yang, X. Zhu, L. Zhu and S. Wang, Experimental study and life cycle assessment of CO2 methanation over biochar supported catalysts, *Appl Energy*, 2020, **280**, 115919.
29 T. Alerte, J. P. Edwards, C. M. Gabardo, C. P. O'Brien, A. Gaona, J. Wicks, A. Obradović, A. Sarkar, S. A. Jaffer, H. L. MacLean, D. Sinton and E. H. Sargent, Downstream of the CO2 Electrolyzer: Assessing the Energy Intensity of Product Separation, *ACS Energy Lett*, 2021, **6**, 4405–4412.
30 Federal Commons LCA data repository, https://www.lcacommons.gov/lca-collaboration/.
31 NETL (2022), NETL CO2U openLCA LCI Database (Version 2.0), Pittsburgh, PA: National Energy Technology Laboratory, U.S. Department of Energy.
32 J. C. Bare, Traci, *J Ind Ecol*, 2002, **6**, 49–78.
33 J. Bare, TRACI 2.0: the tool for the reduction and assessment of chemical and other environmental impacts 2.0, *Clean Technol Environ Policy*, 2011, **13**, 687–696.
34 J. C. Bare, *Tool for the Reduction and Assessment of Chemical and Other Environmental Impacts (TRACI) TRACI version 2.1 User's Guide*, U.S. EPA Office of Research and Development, Washington, DC, EPA/600/R-12/554, 2014.

35 International Energy Agency, Global Energy & CO2 Status Report 2019 Emissions,https://www.iea.org/reports/global-energy-co2-status-report-2019/emissions.

36 H. Yang, J. J. Kaczur, S. D. Sajjad and R. I. Masel, Performance and long-term stability of CO2 conversion to formic acid using a three-compartment electrolyzer design, *Journal of CO2 Utilization*, 2020, **42**, 101349.

37 US Patent, US4326073A, 1982.

38 M. Shemfe, S. Gadkari, E. Yu, S. Rasul, K. Scott, I. M. Head, S. Gu and J. Sadhukhan, Life cycle, techno-economic and dynamic simulation assessment of bioelectrochemical systems: A case of formic acid synthesis, *Bioresour Technol*, 2018, **255**, 39–49.

39 J. Jung, S. Postels and A. Bardow, Cleaner chlorine production using oxygen depolarized cathodes? A life cycle assessment, *J Clean Prod*, 2014, **80**, 46–56.

40 J. Sadhukhan, N. Joshi, M. Shemfe and J. R. Lloyd, Life cycle assessment of sustainable raw material acquisition for functional magnetite bionanoparticle production, *J Environ Manage*, 2017, **199**, 116–125.

41 A. J. Martín, G. O. Larrazábal and J. Pérez-Ramírez, Towards sustainable fuels and chemicals through the electrochemical reduction of CO2: lessons from water electrolysis, *Green Chemistry*, 2015, **17**, 5114–5130.

42 S. Malkhandi and B. S. Yeo, Electrochemical conversion of carbon dioxide to high value chemicals using gas-diffusion electrodes, *Curr Opin Chem Eng*, 2019, **26**, 112–121.

43 M. Rosental, T. Fröhlich and A. Liebich, Life Cycle Assessment of Carbon Capture and Utilization for the Production of Large Volume Organic Chemicals, *Frontiers in Climate*, 2020, **2**, 586199.

44 R. Sadok, G. Benveniste, L. Wang, J. Clavreul, A. Brunot, J. Cren, M. Jegoux and A. Hagen, Life cycle assessment of power-to-gas applications via co-electrolysis of CO 2 and H 2 O Life cycle assessment of power-to-gas applications via co-electrolysis of CO 2 and H 2 O, *J. Phys. Energy*, 2020, **2**, 024006.

45 European Environmental Agency, Greenhouse gas emission intensity of electricity generation in Europe, https://www.eea.europa.eu/ims/greenhouse-gas-emission-intensity-of-1.

46 J. Artz, T. E. Müller, K. Thenert, J. Kleinekorte, R. Meys, A. Sternberg, A. Bardow and W. Leitner, Sustainable Conversion of Carbon Dioxide: An Integrated Review of Catalysis and Life Cycle Assessment, *Chem Rev*, 2018, **118**, 434–504.

47 S. J. Bennett, D. J. Schroeder and S. T. McCoy, Towards a Framework for Discussing and Assessing CO2 Utilisation in a Climate Context, *Energy Procedia*, 2014, **63**, 7976–7992.

48 S. Erol, A Statistical Design Approach on Electrochemical Impedance Spectroscopy of NMC Li-Ion Battery, *J Electrochem Soc*, 2022, **169**, 100503.

49 S. Temiz, H. Kurban, S. Erol and M. M. Dalkilic, Regeneration of Lithium-ion battery impedance using a novel machine learning framework and minimal empirical data, *J Energy Storage*, 2022, **52**, 105022.

50 U. Morali and S. Erol, Analysis of electrochemical impedance spectroscopy response for commercial lithium-ion batteries: modeling of equivalent circuit elements, *Turk J Chem*, 2020, **44**, 602–613.

51 M. Algren, W. Fisher and A. E. Landis, in *Data Science Applied to Sustainability Analysis*, Elsevier, 2021, pp. 167–190.

52 A. Ghoroghi, Y. Rezgui, I. Petri and T. Beach, Advances in application of machine learning to life cycle assessment: a literature review, *Int J Life Cycle Assess*, 2022, **27**, 433–456.

Supporting Information for Task 7. Final Life Cycle Analysis

S1. General background on Greenhouse Gas Emissions

Carbon dioxide (CO_2) is the primary greenhouse gas (GHG) in the troposphere and anthropogenic activities account for the great majority of its emissions. According to the United States Environmental Protection Agency (EPA), in 2020 nearly 80% of total CO_2 emissions in the US arose from human activities, of which combustion and energy production processes constitute a large share.[1] Interestingly, although transportation was estimated to be the largest source of GHG emissions, electric power generation alone, which is primarily based on fossil fuels, accounted for 31% of total emission of CO_2 in the US and for overall 25% of all GHG emissions; furthermore, industrial processes were estimated responsible for additional 24% of GHG emissions (and 16% of CO_2 emissions). It has been long established that the increase of CO_2 concentration in the troposphere has led (and continues to yield) to detrimental environmental effect[1–4] which are acerbated by the long atmospheric lifetime of this GHG.[5] As emissions of CO_2 have increased in past decades,[3] the quest to find sustainable and feasible strategies to mitigate the related environmental impacts has become increasingly pressing. Among these, the development of technologies to capture and utilize CO_2 has been at the focus of much research efforts, [6–14] as associated with the great prospective of decreasing the CO_2 budget in the atmosphere, and converting this GHG into usable materials and products. This differs from carbon capture as carbon capture often just captures the carbon and stores in often in underground deposits which does not solve the problem as there is no reduction in overall CO_2. As CO_2 is naturally very stable, its conversion is achievable only with the use of technologies and methods developed *ad hoc* for this purpose. Among various approaches, electrocatalytic reduction of CO_2 (CO_2ER) represents a promising route to promote its reactivity and conversion to other chemicals, [6–14] which, coupled with the use of electricity from renewable energy providers, could represent a green approach to use and convert previously captured CO_2. Despite this, construction of electrochemical cells for CO_2ER and their operation, as well as sourcing CO_2, are complex processes, which may require sophisticated synthetic procedures or use of methods and technologies which may themselves come with a non-zero environmental impact. Clearly, assessment of environmental impacts of use of CO_2 utilization technologies requires further exploration, as only a handful of studies has been reported so far. [15–29]

Section S.2 Survey of previous literature

Table S1 shows a survey of the previous literature and provides a few highlights for each reference cited. Since impact results may vary considerably for different products formed upon CO_2ER, we restrict our discussion primarily to formic acid, which is the product of interest of this study. Although extensive LCA investigations have been carried out previously as outlined in Table S1, the current study can complement the previous reports at least with the following contributions:

1. More systematic sensitivity/parametric investigations to be performed using consistent system modelling and methodology.
2. More inclusive inventory of materials especially for elucidating impact of manufacturing processes

3. More impact categories are analysed
4. Alternative method for product recovery
5. Different energy sources explored using the same system and methodology
6. Implementation of realistic impact of energy and resource/materials requirements
7. Selection of a power providers which are representative of the average modern-day power grid

Some of these points have been addressed in some previous work, however, comparison between results from different studies may be challenging due to the use of different approaches and methodologies. Therefore it is important to provide a unifying analysis by using a systematic approach; we strive to implement all points above using a single model with the same methodology and approach to ensure ease of comparability between various results, as well as rigorous analysis.

Table S1 Collection of previous LCA studies for electrochemical conversion of CO_2 to formic acid. In this table, we report the main highlights of each study alongside the corresponding literature reference. Furthermore, we outline how the results presented in the current work complement the existing literature on this topic.

Ref.	**Highlights**
30	• Focusses economic and environmental assessment (resource depletion and carbon emissions) of CO_2 to formic acid. • Presents three scenarios base scenario vs low and high performance) where different parameters are changed at the same time. • Factors mainly operation • Offers a techno-economic assessment alongside an environmental analysis.
31	• The study focusses on scaling up conversion of CO_2 to FA: it assesses primarily carbon emissions. • The study presents different scenarios base scenario vs low and high performance) where different parameters are changed at the same time. • The study factors mainly operation, rather than manufacturing • Includes consideration of lifetime of apparatus, but very long lifetimes are considered
24	• Analyses formation of different products upon CO_2 (photo)electrochemical reduction • Focusses on the energetic requirements for reaction and product separation (for different products)
25	• Analyses formation of different products upon CO_2 to CO • Focusses mainly on the economics, with some discussion on carbon emissions • Two case scenarios presented • System modelled is different from this work: it couples electrolysis with Fischer-Tropsch process (different from this work)
26	• Analyses formation of different products upon CO_2 to different products • Focusses mainly on the economics, with some discussion on carbon emissions • Different case scenarios presented
28	• Combines technoeconomic and environmental assessment • Analyses formation of different products upon CO_2 to different products

	- Focuses on operation, and does not consider manufacturing processes - Some sensitivity study for Cell Voltage and Faradaic efficiency - Only accounts for clean energy sources
23	- Analyses formation of different products upon CO_2 to different products - Focusses mainly on carbon emissions - Explores importance of electricity emission factor and energy efficiency - Includes electroreduction and product separation, no emphasis on manufacturing processes - Analysis one-step and two-steps reactions
16	- Focusses on resources depletion and carbon emissions from conversion of CO_2 to formate. - Different scenarios, wherein different parameters are changed. - no extensive modelling of manufacturing processes - no systematic parametric investigation
32	- Focusses on carbon emissions from conversion of CO_2 to formic acid. - three scenarios where different parameters are changed at the same time. The model uses photovoltaic energy for operating the reactor. - More focused on the operation of the reactor (no extensive modelling of manufacturing processes).
22	- Compares carbon storage and carbon utilization technologies. It focusses on the potential reduction of carbon emissions - Two scenarios realistic vs conservative) where different parameters are changed at the same time. - Factors both operation and manufacturing, but for the latter, it mainly focusses on the cathode materials - Explores lifetime of cathode material, but does not present a systematic parametric investigation

S.3 Methodology

S3.1 Overview

The LCA was performed using exclusively open-access resources. The openLCA software was used in conjunction with the freely available databases, mainly within the Federal Commons LCA data repository[33] and the National Energy Technology Laboratory (NETL) database for carbon capture and utilization (NETL CO2U database v. 2.0).[34] CO_2 source and electricity provider was selected from the NETL CO2U database v. 2.0. In cases in which no previously reported data were found, an appropriate proxy was selected or, alternatively, we proceeded to assess the environmental impact by modelling the process of interest. The Tool for the Reduction and Assessment of Chemical and other environmental Impacts,[35–37] version 2.1 **(TRACI 2.1)** was selected as Life Cycle Inventory Analysis (LCIA) method, as implemented in openLCA. The method was employed for generating the results within several impact categories. **Table S2** provides an overview of all impact categories considered within the LCIA method and their corresponding indicators.

Table S2. Overview of impact categories and impact indicators

Impact category	Acronym	Indicator
Human Health Cancer Potential	HHCP	CTUh
Human Health Non-Cancer Potential	HHNCP	CTUh
Ecotoxicity Potential	EP	CTUe
Resource depletion Potential - fossil fuels	RDP	MJ surplus
Global Warming Potential	GWP100	kg CO_2 eq
Acidification Potential	AP	kg SO_2 eq
Respiratory effects Potential	REP	kg PM2.5 eq
Photochemical ozone formation Potential	PO_3FP	kg O_3 eq
Eutrophication Potential	EuP	kg N eq
Ozone Depletion Potential	O_3DP	kg CFC-11 eq

Among the impact categories listed in **Table S2**, the acidification and eutrophication potentials can be considered indicators of water (or soil) pollution. The former is primarily liked to the emission of sulphur dioxide from fossil fuel combustion and consequent acidification of rainwater, which can subsequently damage or contaminate basins and soil. The eutrophication potential provides a mean to evaluate the extent to which water or soil are enriched with nutrients, which can result in deleterious unbalance in ecosystems. Clearly, ecotoxicity (in comparative toxicity units, CTU) also refers to aquatic (or terrestrial) pollution upon presence of chemical agents, such as heavy metals. Additionally, other categories of interest include (i) human toxicity, *i.e.*, human health cancer potential (HHCP) and human health non-cancer potential (HHNCP), and (ii) resource depletion, with reference to fossil fuels, which is expected to entail contributions from energy use as well as production of required materials. The remaining categories are primarily a measure of air pollution. Among these, of particular interest to this study is Global Warming Potential (GWP100) which is used to evaluate climate change due to the release of GHGs.[1]

This is possible as openLCA is a software that does all the summation of the pollutants released and the scaling required to make a certain amount of one substance based off input values. The software then uses the final product of the product system to scale the entire preceding process off it. In this studies case the preceding production lines are based off a certain amount of formic acid. The amount of formic acid is then chosen, upon which the results are then obtained through the summation of all the pollutants formed throughout the preceding steps.

Although, to obtain these material input values it is often necessary manually calculate the necessary type and quantity of materials to make a certain amount of a given material. This was often done through use of values available through literature sources, as well through use of stoichiometry to estimate the amounts used assuming the reaction goes to completion.

S3.2 The Goal and Scope

The primary goal of this LCA is to evaluate the environmental impact of manufacturing and operating an electrochemical cell for CO_2 conversion to a valuable product, taken as formic acid (henceforth also referred to as FA), followed by its recovery in high purity. We will focus our attention primarily on the life cycle GWP100, in order to assess whether and how the life cycle of newly developed CO_2 utilization technologies may contribute to mitigate climate changes. A simplified, schematic illustration of the electrochemical cell modelled in this study is represented in **Figure S1**. The catalyst for electrochemical conversion of CO_2 to formic acid is taken as bismuth-based metal-organic framework (Bi-MOF) material. Such materials have been recently investigated in laboratory studies as promising catalysts for this purpose, especially by virtue of their high efficiency and selectivity; the specific catalyst for CO_2 conversion used for this LCA is synthesized as described in recent publications (*vide infra*) [38–41] which were used to model the catalyst preparation process. The counter electrode is platinum-based, as described later in this report (*v*. section S4 for details).

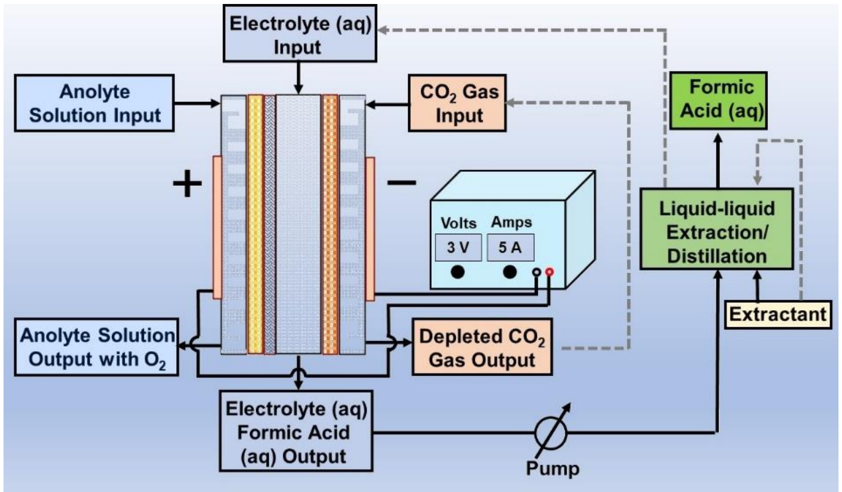

Figure S1: simplified schematic illustration of the electrochemical cell modelled in this LCA

A simplified schematic illustration of the model system is shown in **Figure S2**. Among these, the reactor operation is the process of interest as it produces the desired product upon CO_2ER, coupled with separation of the final product, formic acid, from the electrolyte solution.

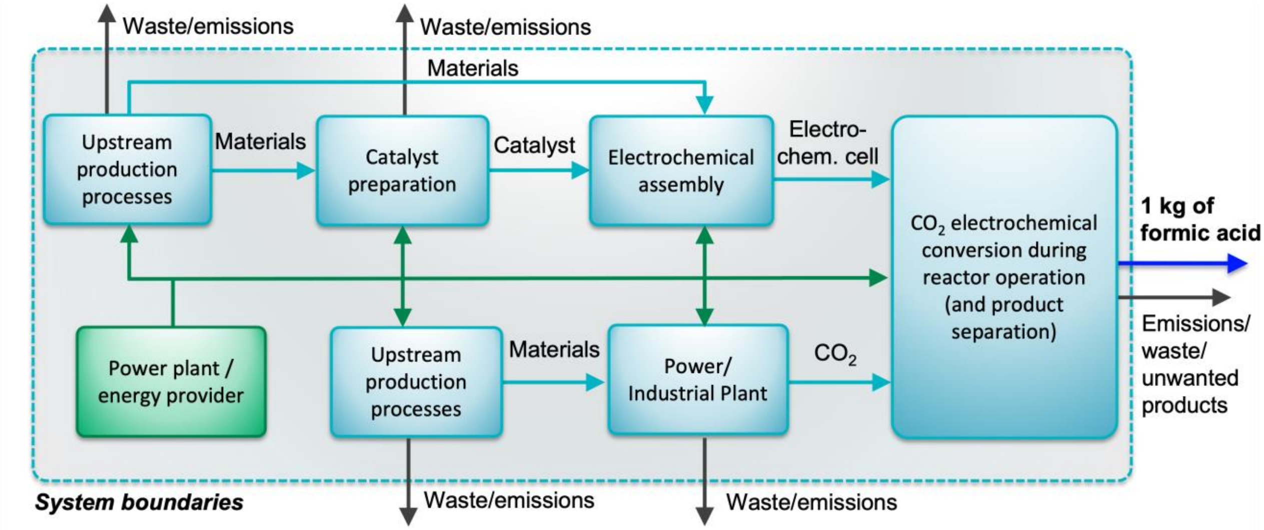

Figure S2: Schematic illustration of the model system.

In **Figure S2**, the expression ‘upstream processes’ refers to the preparation of any chemical reagents or materials necessary for the catalyst synthesis and preparation of the electrochemical assembly, as well as the apparatus required for product separation. Procurement of CO_2 from the power/industrial plant is displayed explicitly. A power plant or equivalent energy provider delivers electricity to power various processes, including electrochemical cell and any associated auxiliary equipment and devices. The functional unit was taken as 1 kg of formic acid being produced upon CO_2ER.

In this study, the energy provider was first selected as to be representative of the modern-day US power grid. The chosen power grid (henceforth PG) accounts for a mixture of both non-renewable and renewable energy sources, with 38% of electricity being generated by natural gas, 22% by coal, 19% by nuclear power plants, and the remaining arising primarily from renewable sources (**Table S3**).[42]

Figure S2, does include some changes throughout the length of the study to account for differences in tech. This includes changes to the operation due to changes in current density of the cell, and changes to the power source to account for the use of more carbon-neutral power sources such as solar or wind.

Table S3: Energy sources and percent contributions for electricity provider

Energy Source	**% Contribution**
Natural gas	38.0%
Coal	22.0%
Nuclear (Gen II)	19.0%
Hydrothermal	6.4%
Wind	9.3%
Solar	2.8%
Other Renewable	1.5%
Petrol	0.5%

S4. Life-cycle inventory

A comprehensive inventory of all required chemical substances and energy carriers was prepared for each process necessary to brief describe the model system, as part of the LCI phase of the assessment. Below we provide a description of such inventories. We also list all input and output flows for each unit process in **Tables S4 – S13** of the *Supporting Information*. Each process was initially modelled based on absolute (estimated) quantities required in the laboratory setting (as reported in **Tables S4-S13**); during the LCAI phase such quantities were referenced to the functional unit of 1 kg of formic acid produced upon CO_2ER.

S4.1 Synthesis and Manufacturing Processes

a. Synthesis of the catalyst

The synthesis procedures of the Bi-based catalysts have been reported in previous literature.[38–41] The relative quantities of required chemical reagents have been scaled up so as to allow the synthesis of 0.3750 g of Bi-MOF, *i.e.*, the mass necessary to prepare one electrode (1 item) of a total area of 100 cm^2 with a catalyst load of 3.75 mg/cm^2. All the input flows required for synthesis are reported in **Table S4**. Here, the term 'electricity' accounts for the energy required to power the necessary laboratory equipment (*e.g.*, heating platform, stirrer, centrifuge etc.). **Table S5** reports the output flows for the process. Similarly, a comprehensive inventory of chemicals, materials and energy providers for the preparation of the electrode and assembly is reported in **Table S6**, while all output flows are listed in **Table S7**. The '*' indicated that the processes were modelled by the authors.

Briefly, In the laboratory, the synthesis would proceed as it follows; 0.3696 g of bismuth nitrate pentahydrate ($Bi(NO_3)_3 \cdot 5H_2O$) and 0.4319 g of 1,3,5-benzenetricarboxylic acid (H_3BTC) are mixed in 4.7311g of dimethylformamide (DMF) and 0.4319 g of methanol (MeOH). The mixture is heated at 120 °C for 24 h, then centrifuged to separate the precipitate product from the supernatant fluid (electricity input required). The solid product is then washed with methanol three times, and vacuum-dried for 12 h at a temperature of 80 °C. The powder is pyrolyzed at 600^{o}C for 2 hours. Use of electricity is required to power different laboratory devices for required for various procedures; this includes 2.4 kWh required for pyrolysis of the powder (1.2 kW, 2 h of pyrolysis) as well as the use of heating equipment, *e.g.* an autoclave, (a total of 4.8 kWh considering 24 h heating time) and centrifuge (a total of 0.194 kWh).

Table S4: Input flows for synthesis of the Bi-MOF catalyst

Flow	**Amount**	**Unit**	**Description**
$Bi(NO_3)_3 \bullet 5H_2O$*	0.3696	g	
DMF *	4.7311	g	
H_3BTC *	0.4319	g	
Methanol	15.00	g	
Electricity	7.394	kWh	Powering equipment
Transportation	20.00	kg × km	Transportation by truck – for all materials
Glass	10.00	g	Formed/finished: reaction container

Table S5: Output flows for synthesis of the Bi-MOF catalyst

Flow	**Amount**	**Unit**	**Description**
Bi-MOF catalyst	**0.3750**	**g**	**Quantitative reference**
Nonhalogenated solvent waste	20.1146	g	Disposal of solvent mixture containing; water, methanol, DMF, H_3BTC and nitrate

Synthesis of $Bi(NO_3)_3 \bullet 5H_2O$, DMF and H_3BTC were modelled by the authors; the associated inventories can be made available upon request.

The mass of the Bi-MOF catalyst is set as the quantitative reference for this process and is inputted into the following process consisting of the preparation of the electrodes and CO_2ER reactor (*v.* Manufacturing of the reactor)

b. Manufacturing of the reactor

The inventory below includes materials and energy required for electrode preparation as well as manufacturing a fully functional reactor. Use of electricity is required to power different laboratory devices for required for electrode preparation. This mainly includes a small heating element (0.054 kW, heating for 12 h).

Table S6. Input flows for assembling of the reactor for the conversion of CO_2 to formic acid.

Flow	**Amount**	**Unit**	**Description**
Bi-MOF catalyst *	**0.375**	**g**	**Product from ‘catalyst preparation’**
Battery-Grade Graphite *	0.275	kg	Graphite plates
Copper sheet	153.0	g	
De-ionised water	100.0	g	For electrode preparation
Electricity	0.648	kWh	Heating/drying (electrode preparation)
Electrolyte, $KHCO_3$(aq) *	10.0	kg	Large batch of electrolyte, circulated, 0.5 M
Ethanol, mass	119.65	g	For electrode preparation
Granulates (PET,HDPE,PP)	1500	g	Container for electrolyte/reaction product
Hydraulic pumps	1	item	Small circulator/pump, materials cost $25
Nitrogen	150	g	For electrode preparation
Platinum	200	mg	
B-PVC resin	11.52	g	Tubing
Separator *	25.38	g	Polymeric, electrode separator
Steel Plates and bolts *	1002	g	
Transport	2500	kg × km	Combination truck, diesel powered

Table S7. Output flows for assembling of the reactor for the conversion of CO_2 to formic acid.

Flow	**Amount**	**Units**	**Description**
Electrochemical Cell	**1**	**item**	**Reactor for electrochemical process**
Nonhalogenated solvent waste	329.65	g	Disposal of solvent mixture containing primarily water and ethanol
Nitrogen	150.00	g	Emission to air

The electrochemical cell is the quantitative reference and is inputted into the following process, *i.e.*, cell operation.

c. Manufacturing of the separation set-up

The apparatus used for this purpose is qualitatively modelled according to an established procedure[43] and it is envisaged to be constituted by an extraction column followed by two distillation stages. In absence of a full inventory, we considered the most abundant materials required to build the apparatus and estimated their quantities based on the required size of the apparatus. Plastics for containers (collection of phases, FA, extractant etc.) as well as for tubing are accounted for. Minor steel/metal components are also considered. Extractant was selected as ethyl acetate[43] to be recovered and recycled during the process.

Table S8. Input flows for preparation of extraction/distillation apparatus

Flow	**Amount**	**Unit**	**Description**
Ethyl acetate *	10.0	kg	Extractant, large batch to be recycled
Glass	14.6537	kg	Formed and finished, for extraction/distillation columns
Glass	0.25	kg	Formed and finished, minor parts of extraction column
Plastics	0.725	kg	Containers (PC, LDPE, PB)

Heating mantle *	2.0	Items	Heating system, 1 for each distillation stage
Pump	1	item	Proxy for low vacuum pump (materials cost $50)
B-PVC	0.1	kg	Tubing
Steel	0.528	kg	Parts of extraction column

Table S9. Output flows for preparation of extraction/distillation apparatus

Flow	**Amount**	**Unit**	**Description**
Separation apparatus	**1.0**	**item**	

In absence of available data set for production of ethyl acetate and the heating element, we proceeded by evaluating the environmental impact of their production by modelling such processes. The associated inventories can be made available upon request.

The separation apparatus is the quantitative reference and is inputted into the following process, *i.e.*, formic acid separation.

S4.2 Operation processes

a. Cell operation

Operation of the electrochemical cell was subsequently modelled. In first approximation, we assumed that all converted CO_2 produces formic acid and that no by-products (H_2, CO etc) are formed. The assumption is justified by experimental studies which show high efficiency and selectivity for formation of formic acid by CO_2 conversion catalysed by Bi-based catalysts[38–41,44–46] and, therefore, negligeable yields for production of unwanted/side-products. We envisage that, in order to maximize the utilization of CO_2, any leftover, output gas should be recycled as to allow virtually 100% of the gas to be converted, thus minimizing waste and increasing the potential environmental benefits.[23,47] For the baseline model, the total amount of CO_2 utilized, formic acid produced, and electricity used are estimated by considering a projected cell lifetime of 4,000 hours at a current density of 1.00 A cm^{-2}. The overall energy consumption for operating the cell (7.50 kWh/kg of formic acid) includes the energy required to sustain CO_2ER (6.92 kWh/kg of formic acid), which was determined in accord with previously reported studies,[48] as well as a contribution arising from the use of ancillary equipment (0.58 kWh/kg of formic acid).

The formic acid produced upon CO_2 electroconversion is assumed to be obtained as dissolved in the aqueous solution. Therefore, separation of the formic acid from the said solution is required to recover a commercial grade final product (≥85% purity). In this study, we selected liquid-liquid extraction as a method to recover high purity formic acid.[43,49–51] Although techno-economic assessments suggest this separation method might not be always efficient and cost effective,[52] it is established to allow recovering the great majority of the product in high purity.[43] The LCA could provide some insight regarding its feasibility or benefits under the environmental perspective, especially compared to (energy-intensive) direct distillation from aqueous solution.[23] The apparatus used for this purpose is qualitatively modelled according to an established procedure[43] and it is envisaged to be constituted by an extraction column followed by two distillation stages. Both aqueous medium and extractant are assumed fully recovered and recycled after extraction and distillation, while virtually all formic acid (99.9%) is obtained in high purity at the end of the distillation procedure. A small fraction of unrecovered formic acid (0.1%) is considered emitted to water. The rate of recovery of high purity formic acid is set to 255 g / hour.[43] It should be specified that the feasibility of liquid-liquid extraction is contingent upon the product being dissolved in the starting aqueous solution in its protonated form rather than its conjugate base (formate).[47] Much of the current literature has reported the production of formate,[53–56] as typically the *p*H of the electrolyte solution is considerably higher than the *p*Ka of formic acid. In such situations, an acidification step is required before performing liquid-liquid extraction. However, a few studies reporting formation and direct observation of formic acid upon CO_2ER[57–59] obtained in water in high concentration (up to 20% in weight). In all cases, adequate product concentrations are necessary for an efficient extraction/distillation procedure. In the following discussion, we work under two assumption; (i) the aqueous (or electrolyte) solution is recirculated through the apparatus to allow build-up of the product until concentrations suitable for liquid-liquid extraction are obtained (e.g., 10%-20% by weight),[23,43] and (ii) the product is dissolved in the aqueous solution in its acidic form when fed into the extractor. In our analysis, we do not model possible changes in faradaic efficiency which may arise from increasing concentration of product in the electrolyte solution,[57,58,60] but we recognize that it could results to loss of efficiency, thus potentially higher environmental impact. In this study, the overall energy consumption to sustain the separation processes was estimated as 3.50 kWh/kg of formic acid produced, accounting for energy requirements of vacuum and heating elements. All relevant inventories are reported in **Tables S10-S15**, alongside the mathematical relationships used during the modelling phase of the study.

a. Cell operation

The total minimum mass of CO_2 ($m(CO_2)$, in grams) to be utilized for CO_2ER during the whole operation time (*t*) can be calculated based on the target current density *j* (in A/cm^2) for operation time, *t*, as in Equation [1]:

$$m_{CO2}(g) = \frac{j\times A\times 6.28\times 10^{18}\times 44.01\times t\times 3600}{2\times 6.022\times 10^{23}} \qquad [1]$$

In this study, the overall area *A* was fixed to 100 cm^2, while *j* and *t* were scanned across wide ranges during parametric studies. Based on simple stoichiometric considerations, the input and output flows for other chemical substances over the time *t* are calculated according to the Equations [2]-[4]:

$$m_{FA(aq)}(g) = \frac{m(CO_2)\times 46.03}{44.01} \qquad [2]$$

$$m_{O2}(g) = \frac{m(FA)\times 15.999}{46.03} \qquad [3]$$

$$m_{H2O}(g) = \frac{m(FA)\times 18.02}{46.03} \qquad [4]$$

The mass of formic acid produced ($m\big(FA(aq)\big)$) is set as the quantitative reference for this process and is inputted into the following process (formic acid extraction). The electricity required to perform CO_2ER is then evaluated considering the following relationships:

$$E_{CO2ER}(kWh) = \frac{V \times j \times A \times t}{1000} \quad [5]$$

With the voltage V evaluated as in a recent publication, according to Equation [6]:

$$V(V) = 1.359 + 0.3731 * \ln(j \times 1000) + 0.001543 \times j \times 1000 \quad [6]$$

An additional, minor contribution for electricity consumption is added to account for ancillary equipment, such as a small circulator/pump. This balance of plant is estimated by considering a required power of 50 W multiplied by the set operation time, *t*. The inventory below reports the list of input and output flows with quantities relative to the baseline system (*t* = 4,000 hours, *j* = 1.00 A/cm^2).

Table S10. Input flows for operation of the electrochemical cell

Flow	**Amount**	**Units**	**Description**
Electrochemical Cell*	**1**	**item**	**Reactor for CO_2ER (previous process)**
Carbon dioxide	3.3E5	g	CO_2 utilized in 4000 h
Electricity	2392	kWh	Operation, 1.00 A/cm^2, 4,000 h, includes cell and BoP
DI water	1.4E5	g	De-ionised water production, reverse osmosis

Table S11. Output flows for operation of the electrochemical cell

Flow	**Amount**	**Unit**	**Description**
Formic Acid (aq)*	**3.5E5**	**g**	**Dissolved in electrolyte solution, to recover**
Oxygen, in air	1.2E5	g	Emission to air
End-of-life reactor	1	Item	End-of-life reactor to be disassembled

The total energy consumption (E_{Tot}) for cell operation is also reported. If the current density j and associated voltage V are changed, then energy requirement to perform CO_2ER will vary according to Eq. [5], alongside all input and output flows of reactants and products (Eq. [1]-[4]). **Table S12** reports the estimated energy consumption estimated per kg of FA produced upon CO_2ER (E_{CO2ER}) at various current densities. The total energy, including the balance of plant is also reported.

Table S12: Energy consumption for CO_2ER (E_{React}) and total energy consumption for cell operation, accounting the BoP, (E_{Tot}) in units of Wh per kg of FA produced upon CO_2ER.

***j* (A/cm^2)**	**E_{CO2ER} (Wh/kg FA)**	**E_{Tot} (Wh/kg FA)**
0.25	4.40	6.72
0.50	5.15	6.31
0.75	5.77	6.54
1.00	6.34	6.92
1.25	6.88	7.35

1.50	7.41	7.80

Analogous values are plotted in **Figure S3**, which provides a clear-cut illustration of the trends in energy consumption as a function of the current density *j* explored in this study. The figure shows as the energy required for the CO_2ER increases (Wh/kg of FA) more sharply with increasing the current density when compared to the mass of FA produced.

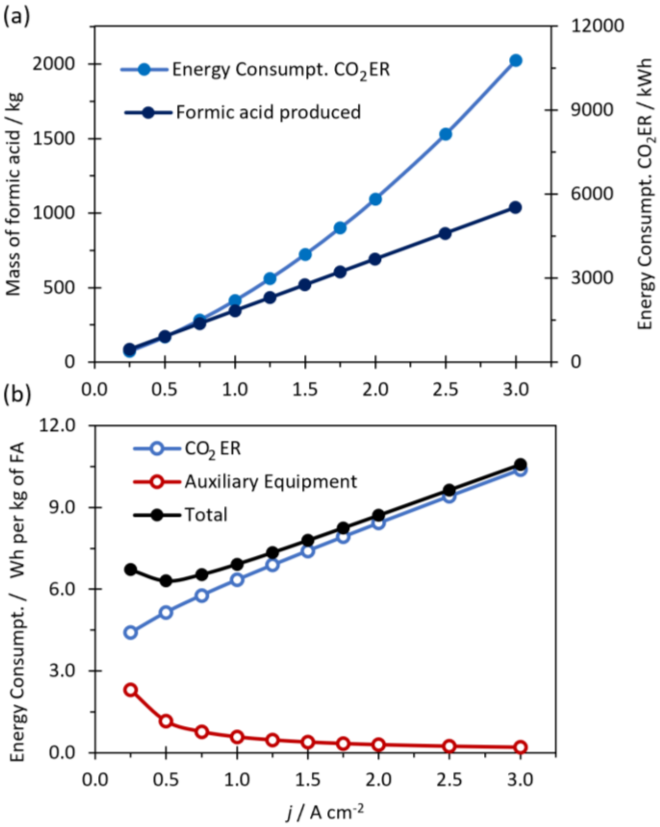

Figure S3: (a) mass of FA produced and energy consumption to perform CO_2ER as a function of current densities (4,000 hours). (b) Energy consumption per kg of FA produced for auxiliary equipment (red) and CO_2ER (blue) and total energy consumption (black).

b. <u>Formic acid extraction</u>

In **Table S13**, the separation apparatus is the product flow which accounts for the extraction and distillations column, vacuum and eating elements, extractant phase and other required basic materials for a fully functional set-up.

The other crucial input flow is clearly the formic acid (aq) product, generated *via* CO_2ER (*v*. <u>Cell operation</u>), for which the total amount produced for the baseline system is reported in **Table S3**. Cooling water is taken as a resource; this is not recycled, but rather simply re-emitted to water as not chemically contaminated. This is done since the TRACI 2.1 model does not consider water usage as impact category and therefore use of water resource does not affect any of the impact results in the various categories. The flow rate of water was assumed to be 60 L/minute. Electricity was assumed to have a contribution arising from the use of various ancillary equipment, mostly heating elements, but also an intermittently operating vacuum pump, and constantly operating stirrer. Amongst the output flows, we list the high purity formic acid recovered (99.9% of overall input flow) plus a small fraction of formic acid not during the process (0.1%), considered as ultimately emitted to water. Water waste and used apparatus are also listed as outputs for completeness. All total quantities at the end of the process clearly depend on the extraction and distillation run time and are all evaluated as it follows.

The total separation run time (t_{sep}) is *approximately* evaluated as a ration between the total mass of FA(aq) produced and the rate of its recovery:

$$t_{sep} = \frac{m_{FA(aq)}}{v} \quad [7]$$

For this study, we assumes a recovery rate of 255 g per hour, as mentioned above.[43]

The overall volume (in L) of water $V_{H2O,cool}$ used is then evaluated as:

$$V_{H2O,cool}(L) = 60 \times 2 \times 60 \times t_{sep} \quad [8]$$

Similarly, the total, recovered FA output ($m_{FA,prod}$) is evaluated as:

$$m_{FA,prod}(g) = v \times t_{sep} \times y \quad [9]$$

With *y* being the yield for FA recover here set to 99.9%. Therefore, the unrecovered FA will equal the difference between the total $m_{FA(aq)}$ and $m_{FA,prod}$:

$$m_{FA,lost} = m_{FA(aq)} - m_{FA,prod} \quad [10]$$

The electricity requirements are calculated as the overall sum of various contributions: these include electricity to run the heating elements, accounted as 803 W for each hour of operation, while the stirrer and (intermitted) pump collectively account for ~81 W for each hour of operation. All input and output flows for the extraction/distillation process are reported in **Tables S13** and **S14**; the corresponding amounts reported are the ones calculated for the baseline system. Clearly, input mass of FA(aq) will depend on the upstream CO_2ER process (cell operation): its values will then determine all other input and output amounts.

Table S13. Input flows for preparation of extraction/distillation apparatus

Flow	**Amount**	**Unit**	**Description**
Separation apparatus*	**1.0**	**Item**	
Formic acid (aq)*	**3.5E5**	**g**	**Depends on the parameters set in cell operation**
Water (Cooling, fresh)	5.9E8	L	60 L/min flow rate
Electricity	1198	kWh	Includes heating, stirrer, pumping

Table S14. Output flows for preparation of extraction/distillation apparatus

Flow	**Amount**	**Unit**	**Description**
Formic Acid	**345.27**	**kg**	**Product recovered**
Formic Acid	0.34527	kg	Emitted to water (not recovered)
Water, waste	9E6	L	Emitted to water (not chemically contaminated)
Used separation apparatus	1.0	item	Product recovered

S.4.3 Cell performance degradation and loss of efficiency

This section describes the model used to simulate the decline in performance due to cell aging and subsequent loss of CO_2-to-formic acid efficiency.

This model was developed based on a time-dependent exponential decay curve for the efficiency ($\mathrm{N}(t)$) represented by:

$$\mathrm{N}(t) = 1 - e^{a(t-t_{max})} \quad [11]$$

Wherein a represents the decay constant, t is the operation time and t_{max} is the maximum operation time. The value of t_{max} is estimated considering a target minimum efficiency (η_{min}) of 10% and a cell lifetime corresponding to 4,000 hours of operation (t_{op}), according to the following equations:

$$t_{max} = t_{op} - \frac{ln(1-\eta_{min})}{a} \quad [12]$$

For this study, the decay constant a was set to 9.8×10^{-4}, and the t_{max} was derived as 4107 hours. The model can be fully implemented using Excel or an equivalent data processing program; the differential form of equation [11] with respect to time is derived and used to plot the associated changes in efficiency as a function of time. This is done by taking the derivative of the equation concerning time which results in the following equation:

$$\eta(t) = \eta(t-\Delta t) - \Delta t a e^{a(t-t_{max}-S_c)} \quad [13]$$

A sample graph obtained from Eq.[12] is displayed in **Figure S4**; here the $\eta(t)$ is plotted across several cell lifetimes. The parameter S_{c} in Eq.[13] can be simply considered a shift factor which effectively accounts for number of electrochemical cell being used in the plotted time frame *t*. In other words, Sc allows to simulate the gain in efficiency after each 4,000 hours, which due to cell replacement. In this study, operation of a single cell for 4,000 hours was explored (highlighted area).

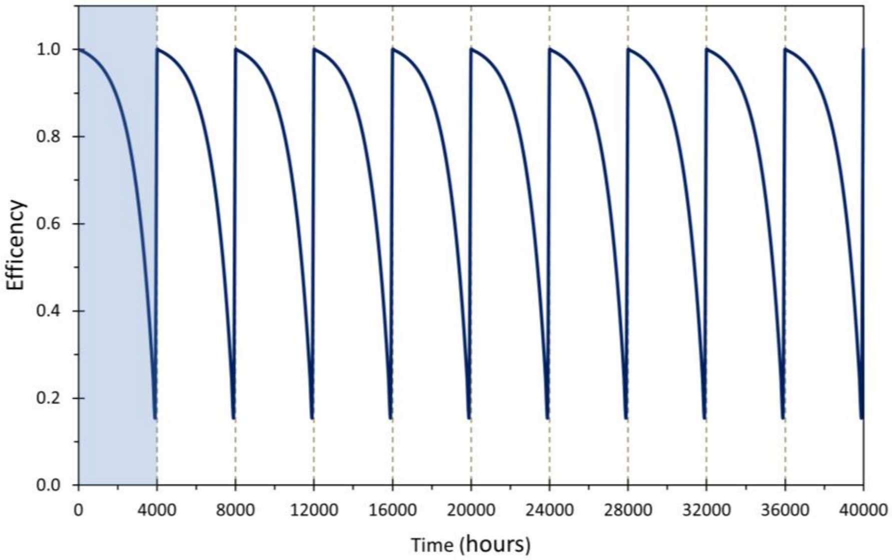

Figure S4: plot of the changes in efficiency as a function of time across various cell lifetimes of

4,000 hours

The CO_2-to- FA conversion efficiency is modelled to follow an exponential-type decay as illustrated in **Figure S5** (blue trace and open circles) while the energy consumption is represented as the reciprocal of the efficiency (black trace and symbols).

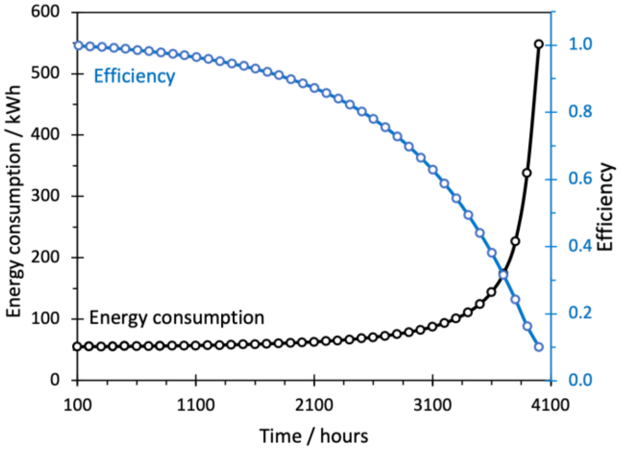

Figure S5: Modelling the electrochemical cell lifetime: the decline in efficiency is illustrated as a function of operation time for an overall cell lifetime of 4,000 hours (blue trace). The corresponding energy consumption (black trace) is also illustrated

S5 Life Cycle Inventory Analysis

S5.1 The Method

General background. The Tool for the Reduction and Assessment of Chemical and Other Environmental Impacts Was selected as LCIA method for this study. Detailed information about TRACI 2.1 can be found in references.[35–37] Briefly, in the most general form, the potential environmental impact *I* associated for impact category *i* is evaluated as in Equation [14]: [35–37]

$$I^i = \sum_s \sum_x \sum_m F^i_{xms}\ P^i_{xms}\ M_{xms}$$

[14]

Where the potential impact for the chosen category I^i depends on the fate and potency of all chemical species x emitted to the media m, at specific sites s, *i.e.*, F^i_{xms} and P^i_{xms}, respectively, as well as the mass of same (M_{xms}). As in this study (and many others), location is not considered as it is not expected to substantially influence the potential impact; this is true because in most cases the fate and potency of chemical species do not have a marked dependence on the site of emission. Then the location variable s can be disregarded and potential impact I^i expressed in a more compact, generic form as in Equation [15]:

$$I^i = \sum_{xm} CF^i_{xm} \times M_{xm}$$

[15]

Where CF_{xm}^{i} is the characterization factor for species x emitted to the media m associated with category i, and M_{xm} is the mass of the species x emitted to the media m. As a final remark, the overall I^{i} will be rescaled considering a target mass of 1 kg of FA produced.

GHG Emissions from the Energy Sources. The GWP100 can be considered a category indicative of the global warming impact arising from the release of GHGs. In this instance, the overall GWP100 can be estimated according to Eq. [15], by considering that the chemical species x is emitted exclusively to air.

$$I^{GWP100} = \sum_{x} CF_{x,air}^{GWP100} \times M_{x,air}$$

[16]

As a considerable amount of GHG emissions in the present studies arises from use of electricity to sustain CO_2ER and product separation, the contribution of the energy provider to the GWP100 deserves consideration. Table S15 shows the carbon intensity of various energy providers *j* (*CI$_j$*) selected from the NETL CO2U database v. 2.0,[34] thus showing the corresponding mass of CO_2e emitted per each kWh of electricity produced/used.

Table S15: Carbon intensity of different energy providers (NETL CO2U database v. 2.0)[34]

Energy Source	kg CO_2e/kWh
Natural gas	0.477
Coal	1.169
Nuclear (Gen II)	0.030
Hydrothermal	0.023
Wind	0.129
Solar	0.034
Petrol	1.080

For a generic PG mix, the carbon intensity (CI) clearly depends on the relative contributions (*Wj*) of the different energy sources to the energy mix. For the adjusted PG used in the study, the contributions will be as it follows:

$$CI = \sum_{j} CI_j \times W_j$$

[17]

For the PG as defined in **Section S2.5**, CI is estimated as 0.467 kg of CO_2e/kWh. Although this value may be higher than the CI for electricity in many countries, it is representative of the average carbon intensity of electricity today.

Data ranges and deviations. In the parametric studies performed for this LCA, the I^{i} ma vary considerably based on the parameters used. To obtain an estimate of the deviation between each data point, we can use a simple statistic approach as in Eq. [16]:

$$\sigma = \frac{\sum_n (I_n^i \times \overline{I^i})}{N} \qquad [18]$$

Wherein I_n^i is the the value of I^i for data point n and $\overline{I^i}$ is impact averaged across the number of data point N.

5.2 Environmental impact: the baseline system

An overview of the corresponding impact results is reported in **Table S14**.

Table S14: Impact results for the baseline model

Impact category	**Impact result**	**Unit**
HHCP	1.6×10^{-8}	CTUh
HHNCP	$9.\ 8\times10^{-7}$	CTUh
Ecotoxicity	1.5	CTUe
Resource depletion	0.54	MJ surplus
GWP100	5.5	kg CO_2e
Acidification	1.0×10^{-2}	kg SO_2e
Respiratory effects	1.6×10^{-3}	kg PM2.5e
Photochem. O_3 formation	0.10	kg O_3e
Eutrophication	5.7×10^{-4}	kg N eq
O_3 Depletion	2.3×10^{-8}	kg CFC-11e

Further analysis reveals that the energy provider accounts for most of the impact, especially referring to the CO_2ER and product separation which are both energy-intensive processes. For instance, impact on resource depletion (**Figure S6(a)**) is primarily attributed to extensive use of energy (68.9%), the majority of which is accounted for during cell operation (39.1%) and extraction/distillation processes (19.6%). This is followed by contributions arising from the production of glass components, primarily for the extraction/distillation apparatus, which account for about ~16% of the total impact, and manufacturing of plastic materials employed to construct the assemblies, contributing by ~13% to the overall results. Furthermore, impact in the HHCP category (**Figure S6(b)**, left panel) also arises primarily from the energy provider, especially from nuclear power generation, as linked to the potential emission of heavy metals (*i.e.*, arsenic) in water and/or soil. Additional ~14% of impact is attributed to the production of plastic materials (*e.g.*, PVC) and associated release of toxic chemicals, such as dioxins, into water and air. The impact for HHNCP **(Figure S6(b)**, right panel) is overwhelmingly attributed to the energy provider. Similar results are observed for other impact categories (not discussed in this work).

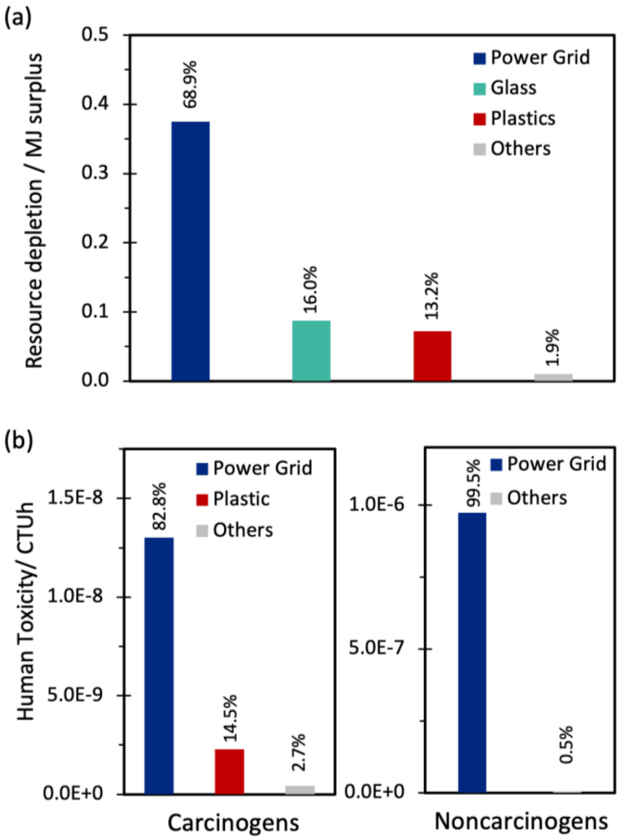

Figure S6: Impact results within (a) resource depletion impact category, and (b) HHCP (left panel) and HHNCP (right panel) for the base model system.

5.3 Parametric Studies

The sections below report the impact results for electrochemical reduction of CO_2 using the model system, alongside the interpretation and discussion of the results obtained. We will primarily restrict our discussion to impact results concerning GHG emissions (GWP100) but will provide a short description of other impact results for completeness. **Table S15** reports an overview of the various parameters and relative ranges explored in this LCA study.

Table S15. Overview of parameters and ranges for the sensitivity analysis in this LCA study.

Parameters	**Range**
Reactor Lifetime	24 – 40,000 h
Current Density, *j*	0.25 – 1.50 A cm^{-2}
Energy provider	PG vs Renewable
Total life cycle emissions	Over 4,000 h operation

S5.2.1 Stability and Durability

General Analysis. Figure S7 illustrates an overview of impact results for various impact categories as a function of the cell lifetime. For convenience, the impact results of each category have been rescaled so as to allow displaying them appropriately on a single graph. Scaling factors are specified in the figure caption.

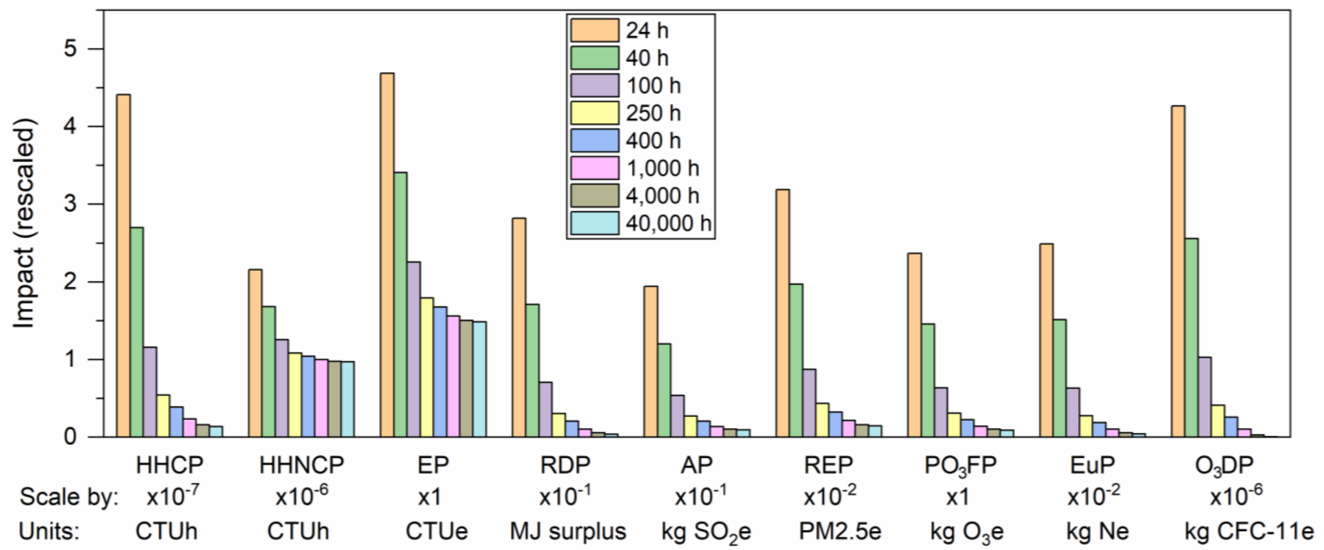

Figure S7: Overview of impact results for various impact categories as a function of the cell lifetime (24 – 40,000 hours). EP = ecotoxicity potential, RDP = resource depletion potential, AP = acidification potential, REP = respiratory effect potential, PO_3FP = photochemical ozone formation potential, EuP = eutrophication potential, O_3DP = ozone depletion potential.

All impact results decrease as the lifetime (or operation time) of the electrochemical cell is extended. This dependence is more evident in the short lifetime regime, while the impact results change less drastically or even level off at lifetimes longer than 1,000 hours of operation. Higher impact results at shorter lifetimes are primarily attributed to larger contributions arising from manufacturing processes (*cf.* cell operation and product separation), which progressively decrease as the lifetime of the cell is extended. This can be ascribed to larger absolute quantities of FA being produced, thus comparatively lower impact of manufacturing processes. To further illustrate this finding, **Figure S8** displays some representative results for the resource depletion (**Figure S8(a)**), HHCP and HHNCP (**Figure S8(b)**) categories at 24 h of operation.

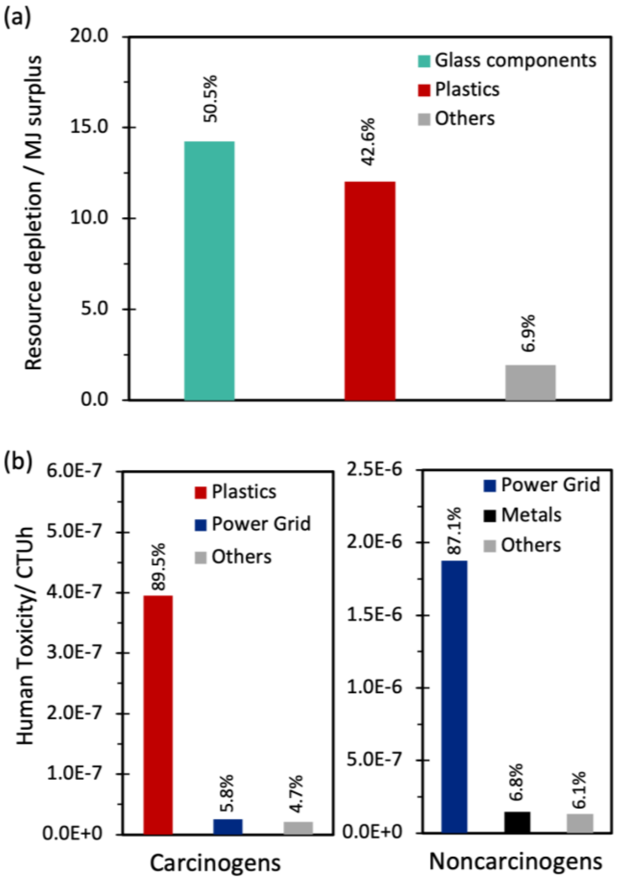

Figure S8: Selected impact results at 24 h lifetime/operation: (a) Resource depletion potential, (b) HHCP (left pane) and HHNCP (right panel).

If the lifetime or operation time of the cell is 24 hours, the resource depletion category (**Figure S8(a)**) is heavily impacted by the production of petrochemical products, including plastic/polymeric materials, and glass for various components of the assemblies, which account together for over 90% of the impact. A 50-fold decrease of is observed as the lifetime of the electrochemical cell is extended from 24 h (**Figure S8(a)**) to 4,000 h with the result falling from 28.19 to 0.54 MJ surplus per kg of FA produced. This is, again, attributed to greater weight of preparation procedures at shorter lifetimes. Analogously, compared to the HHCP results a ~30-fold decrease as the lifetime varies from 24 to 4,000 h, with values of 4.41×10^{-7} CTU_h and 1.58×10^{-8} per kg of FA, respectively. By inspection of **Figure S8(b)**, it is clear that the majority of impact for HHCP at 24 h arises from production of plastic materials and associated release of dioxins (~90%), as opposed to the (nuclear) energy provider, which account for a smaller fraction of the impact. By contrast, HHNCP results show a less marked dependence on the operation time. This can be understood if one considers that the major contributor to this impact category is predicted to be the power grid (especially nuclear power) at all operation times.

S5.2.2 Current Density

General analysis. An overview of impact results for the different categories is shown in **Figure S9**. Again, impact results have been rescaled to be displayed on comparable scales in a graph. In this analysis, the impact results vary mildly with the current density. Impact results of most categories are observed to decrease at first, and then slightly increase as function of the current density *j*, since cell operation (and CO_2ER in particular), which makes up the largest impact, progressively requires more energy.

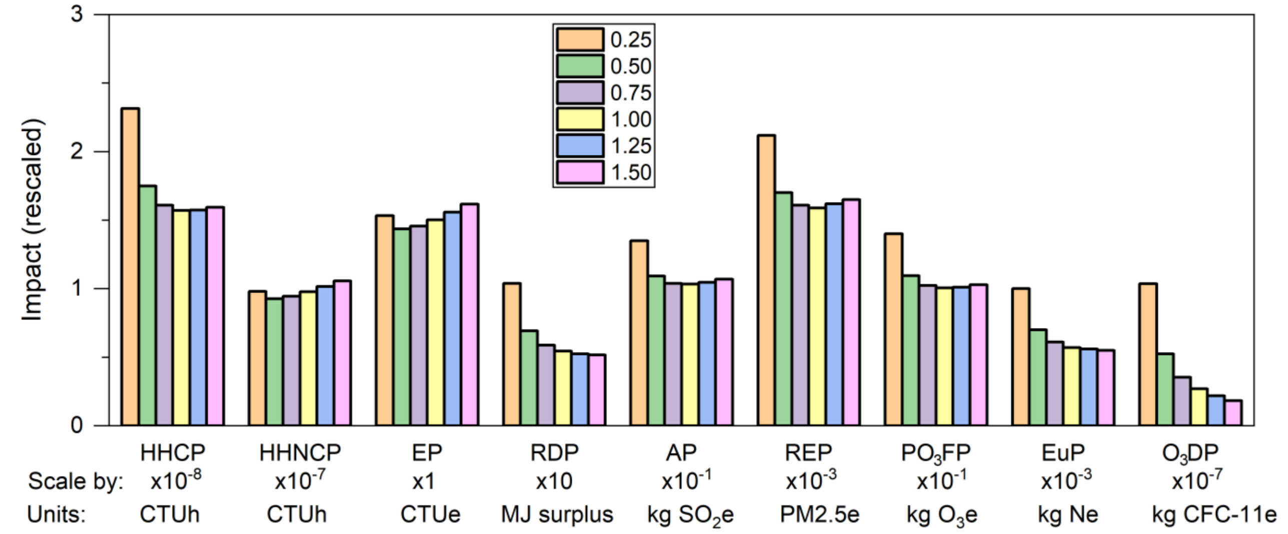

Figure S9: Overview of impact results for various impact categories as a function of the current density (0.25 – 3.00 A cm^{-2}). EP = ecotoxicity potential, RDP = resource depletion potential, AP = acidification potential, REP = respiratory effect potential, PO_3FP = photochemical ozone formation potential, EuP = eutrophication potential, O_3DP = ozone depletion potential.

In **Figure S9**, only ozone depletion potential is predicted to considerably decrease; this trend can be understood if one considers that materials production and preparation of the electrochemical and separation assemblies are determinant for this impact category. The ozone depletion is found to arise primarily from preparation of the two assemblies (~95% at 1.00 A cm^{-2}). In particular, it is related to the production of polymeric materials and glass within the electrochemical cell and extraction/distillation apparatus, as well as the associated use of organic solvents and compounds. As the impact of ozone depletion decreases at higher current density, it can be inferred that the contribution of preparation procedures declines at the same time, since higher current density leads to increased production of FA.

Section S6. Method Comparison

Table S16: comparison between the Impact analysis obtained through TRACI 2.1 and CLM methods for three selected categories. The analysis is run on the same inventories, thus the results with the two methods are comparable.

Impact category	TRACI 2.1	CLM	Unit
GWP100	**5.5**	**5.5**	**kg CO_2e**
Acidification	1.0×10^{-2}	9.7×10^{-3}	kg SO_2e
O_3 Depletion	2.3×10^{-8}	1.8×10^{-8}	kg CFC-11e

References

1 EPA, *Inventory of U.S. Greenhouse Gas Emissions and Sinks: 1990-2020. U.S. Environmental Protection Agency, EPA 430-R-22-003*, 2022.

2 IPCC, *Summary for Policymakers. In: Climate Change 2007. The Physical Science Basis. Contribution of Working Group I to the Fourth Assessment Report of the Intergovernmental Panel on Climate Change*, [S. Solomon, D. Qin, M. Manning, Z. Cheng, M. Marquis, K. B. Averyt, M. Tignor, H. L. Miller, (eds)], Cambridge University PressCambridge, United Kingdom and New York, NY, USA, 996 pp., 2007.

3 USGCRP 2017, *Climate Science Special Report: Fourth National Climate Assessment, Volume I*, [Wuebbles, D.J., D.W. Fahey, K.A. Hibbard, D.J. Dokken, B.C. Stewart, and T.K. Maycock (eds.)]. U.S. Global Change Research Program, Washington, DC, USA, 470 pp, 2017.

4 IPCC, *Climate Change 2007: Mitigation. Contribution of Working Group III to the Fourth Assessment Report of the Intergovernmental Panel on Climate Change*, e [B. Metz, O.R. Davidson, P.R. Bosch, R. Dave, L.A. Meyer (eds)], Cambridge University Press, Cambridge, United Kingdom and New York, NY, USA., 851 pp., 2007.

5 M. Saunois, A. R. Stavert, B. Poulter, P. Bousquet, J. G. Canadell, R. B. Jackson, P. A. Raymond, E. J. Dlugokencky, S. Houweling, P. K. Patra, P. Ciais, V. K. Arora, D. Bastviken, P. Bergamaschi, D. R. Blake, G. Brailsford, L. Bruhwiler, K. M. Carlson, M. Carrol, S. Castaldi, N. Chandra, C. Crevoisier, P. M. Crill, K. Covey, C. L. Curry, G. Etiope, C. Frankenberg, N. Gedney, M. I. Hegglin, L. Höglund-Isaksson, G. Hugelius, M. Ishizawa, A. Ito, G. Janssens-Maenhout, K. M. Jensen, F. Joos, T. Kleinen, P. B. Krummel, R. L. Langenfelds, G. G. Laruelle, L. Liu, T. Machida, S. Maksyutov, K. C. McDonald, J. McNorton, P. A. Miller, J. R. Melton, I. Morino, J. Müller, F. Murguia-Flores, V. Naik, Y. Niwa, S. Noce, S. O’Doherty, R. J. Parker, C. Peng, S. Peng, G. P. Peters, C. Prigent, R. Prinn, M. Ramonet, P. Regnier, W. J. Riley, J. A. Rosentreter, A. Segers, I. J. Simpson, H. Shi, S. J. Smith, L. P. Steele, B. F. Thornton, H. Tian, Y. Tohjima, F. N. Tubiello, A. Tsuruta, N. Viovy, A. Voulgarakis, T. S. Weber, M. van Weele, G. R. van der Werf, R. F. Weiss, D. Worthy, D. Wunch, Y. Yin, Y. Yoshida, W. Zhang, Z. Zhang, Y. Zhao, B. Zheng, Q. Zhu, Q. Zhu and Q. Zhuang, The Global Methane Budget 2000-2017, *Earth Syst. Sci. Data*, 2020, **12**, 1561–1623.

6 R. A. Tufa, D. Chanda, M. Ma, D. Aili, T. B. Demissie, J. Vaes, Q. Li, S. Liu and D. Pant, Towards highly efficient electrochemical CO2 reduction: Cell designs, membranes and electrocatalysts, *Appl. Energy*, 2020, **277**, 115557.

7 A. Saravanan, P. Senthil kumar, D.-V. N. Vo, S. Jeevanantham, V. Bhuvaneswari, V. Anantha Narayanan, P. R. Yaashikaa, S. Swetha and B. Reshma, A comprehensive review on different approaches for CO2 utilization and conversion pathways, *Chem. Eng. Sci.*, 2021, **236**, 116515.

8 A. D. N. Kamkeng, M. Wang, J. Hu, W. Du and F. Qian, Transformation technologies for CO2 utilisation: Current status, challenges and future prospects, *Chem. Eng. J.*, 2021, **409**, 128138.

9 M. D. Garba, M. Usman, S. Khan, F. Shehzad, A. Galadima, M. F. Ehsan, A. S. Ghanem and M. Humayun, CO2 towards fuels: A review of catalytic conversion of carbon dioxide to hydrocarbons, *J. Environ. Chem. Eng.*, 2021, **9**, 104756.

10 D. D. Zhu, J. L. Liu and S. Z. Qiao, Recent Advances in Inorganic Heterogeneous Electrocatalysts for Reduction of Carbon Dioxide, *Adv. Mater.*, 2016, **28**, 3423–3452.
11 A. Liu, M. Gao, X. Ren, F. Meng, Y. Yang, L. Gao, Q. Yang and T. Ma, Current progress in electrocatalytic carbon dioxide reduction to fuels on heterogeneous catalysts, *J. Mater. Chem. A*, 2020, **8**, 3541–3562.
12 C. Jia, K. Dastafkan, W. Ren, W. Yang and C. Zhao, Carbon-based catalysts for electrochemical CO2 reduction, *Sustain. Energy Fuels*, 2019, **3**, 2890–2906.
13 K. Zhao and X. Quan, Carbon-Based Materials for Electrochemical Reduction of CO2 to C2+ Oxygenates: Recent Progress and Remaining Challenges, *ACS Catal.*, 2021, **11**, 2076–2097.
14 J. P. Edwards, Y. Xu, C. M. Gabardo, C.-T. Dinh, J. Li, Z. Qi, A. Ozden, E. H. Sargent and D. Sinton, Efficient electrocatalytic conversion of carbon dioxide in a low-resistance pressurized alkaline electrolyzer, *Appl. Energy*, 2020, **261**, 114305.
15 D. Kim and J. Han, Comprehensive analysis of two catalytic processes to produce formic acid from carbon dioxide, *Appl. Energy*, 2020, **264**, 114711.
16 A. Dominguez-Ramos, B. Singh, X. Zhang, E. G. Hertwich and A. Irabien, Global warming footprint of the electrochemical reduction of carbon dioxide to formate, *J. Clean. Prod.*, 2015, **104**, 148–155.
17 D. Rojas Sánchez, K. Khalilpour and A. F. A. Hoadley, How sustainable is CO2 conversion to ethanol? – A life cycle assessment of a new electrocatalytic carbon utilisation process, *Sustain. Energy Fuels*, 2021, **5**, 5866–5880.
18 P. Yue, Z. Kang, Q. Fu, J. Li, L. Zhang, X. Zhu and Q. Liao, Life cycle and economic analysis of chemicals production via electrolytic (bi)carbonate and gaseous CO2 conversion, *Appl. Energy*, 2021, **304**, 117768.
19 A. Somoza-Tornos, O. J. Guerra, A. M. Crow, W. A. Smith and B.-M. Hodge, Process modeling, techno-economic assessment, and life cycle assessment of the electrochemical reduction of CO2: a review, *iScience*, 2021, **24**, 102813.
20 N. Thonemann, Environmental impacts of CO2-based chemical production: A systematic literature review and meta-analysis, *Appl. Energy*, 2020, **263**, 114599.
21 X. Wang, M. Yang, X. Zhu, L. Zhu and S. Wang, Experimental study and life cycle assessment of CO2 methanation over biochar supported catalysts, *Appl. Energy*, 2020, **280**, 115919.
22 M. Rumayor, A. Dominguez-Ramos and A. Irabien, Environmental and economic assessment of the formic acid electrochemical manufacture using carbon dioxide: Influence of the electrode lifetime, *Sustain. Prod. Consum.*, 2019, **18**, 72–82.
23 S. Kibria Nabil, S. McCoy and M. G. Kibria, Comparative life cycle assessment of electrochemical upgrading of CO2 to fuels and feedstocks, *Green Chem.*, 2021, **23**, 867–880.
24 J. B. Greenblatt, D. J. Miller, J. W. Ager, F. A. Houle and I. D. Sharp, The Technical and Energetic Challenges of Separating (Photo)Electrochemical Carbon Dioxide Reduction Products, *Joule*, 2018, **2**, 381–420.
25 X. Li, P. Anderson, H.-R. M. Jhong, M. Paster, J. F. Stubbins and P. J. A. Kenis, Greenhouse Gas Emissions, Energy Efficiency, and Cost of Synthetic Fuel Production Using Electrochemical CO2 Conversion and the Fischer–Tropsch Process, *Energy & Fuels*, 2016, **30**, 5980–5989.
26 P. De Luna, C. Hahn, D. Higgins, S. A. Jaffer, T. F. Jaramillo and E. H. Sargent, What

would it take for renewably powered electrosynthesis to displace petrochemical processes?, *Science (80-.).*, 2019, **364**, eaav3506.

27 H. H. Khoo, I. Halim and A. D. Handoko, LCA of electrochemical reduction of CO2 to ethylene, *J. CO2 Util.*, 2020, **41**, 101229.

28 P. Yue, Q. Fu, J. Li, X. Zhu and Q. Liao, Comparative life cycle and economic assessments of various value-added chemicals' production via electrochemical CO2 reduction, *Green Chem.*, 2022, **24**, 2927–2936.

29 J. Wyndorps, H. Ostovari and N. von der Assen, Is electrochemical CO2 reduction the future technology for power-to-chemicals? An environmental comparison with H2-based pathways, *Sustain. Energy Fuels*, 2021, **5**, 5748–5761.

30 R. Aldaco, I. Butnar, M. Margallo, J. Laso, M. Rumayor, A. Dominguez-Ramos, A. Irabien and P. E. Dodds, Bringing value to the chemical industry from capture, storage and use of CO2: A dynamic LCA of formic acid production, *Sci. Total Environ.*, 2019, **663**, 738–753.

31 N. Thonemann and A. Schulte, From Laboratory to Industrial Scale: A Prospective LCA for Electrochemical Reduction of CO2 to Formic Acid, *Environ. Sci. Technol.*, 2019, **53**, 12320–12329.

32 M. Rumayor, A. Dominguez-Ramos and A. Irabien, *Appl. Sci.*, 2018, 8.

33 Federal Commons LCA data repository, https://www.lcacommons.gov/lca-collaboration/.

34 NETL (2022), NETL CO2U openLCA LCI Database (Version 2.0), Pittsburgh, PA: National Energy Technology Laboratory, U.S. Department of Energy.

35 J. C. Bare, Traci, *J. Ind. Ecol.*, 2002, **6**, 49–78.

36 J. Bare, TRACI 2.0: the tool for the reduction and assessment of chemical and other environmental impacts 2.0, *Clean Technol. Environ. Policy*, 2011, **13**, 687–696.

37 J. C. Bare, *Tool for the Reduction and Assessment of Chemical and Other Environmental Impacts (TRACI) TRACI version 2.1 User's Guide*, U.S. EPA Office of Research and Development, Washington, DC, EPA/600/R-12/554, 2014.

38 M. Feyand, E. Mugnaioli, F. Vermoortele, B. Bueken, J. M. Dieterich, T. Reimer, U. Kolb, D. de Vos and N. Stock, Automated Diffraction Tomography for the Structure Elucidation of Twinned, Sub-micrometer Crystals of a Highly Porous, Catalytically Active Bismuth Metal–Organic Framework, *Angew. Chemie Int. Ed.*, 2012, **51**, 10373–10376.

39 A. K. Inge, M. Köppen, J. Su, M. Feyand, H. Xu, X. Zou, M. O'Keeffe and N. Stock, Unprecedented Topological Complexity in a Metal–Organic Framework Constructed from Simple Building Units, *J. Am. Chem. Soc.*, 2016, **138**, 1970–1976.

40 X. Zhang, Y. Zhang, Q. Li, X. Zhou, Q. Li, J. Yi, Y. Liu and J. Zhang, Highly efficient and durable aqueous electrocatalytic reduction of CO2 to HCOOH with a novel bismuth–MOF: experimental and DFT studies, *J. Mater. Chem. A*, 2020, **8**, 9776–9787.

41 Y. Guan, X. Zhang, Y. Zhang, T. N. V Karsili, M. Fan, Y. Liu, B. Marchetti and X.-D. Zhou, Achieving high selectivity towards electro-conversion of CO2 using In-doped Bi derived from metal-organic frameworks, *J. Colloid Interface Sci.*, 2022, **612**, 235–245.

42 U.S. Energy Information Administration, Electricity Explained - Basics, https://www.eia.gov/energyexplained/electricity/electricity-in-the-us.php.

43 US Patent, US4326073A, 1982.

44 S. He, F. Ni, Y. Ji, L. Wang, Y. Wen, H. Bai, G. Liu, Y. Zhang, Y. Li, B. Zhang and H. Peng, The p-Orbital Delocalization of Main-Group Metals to Boost CO2 Electroreduction,

Angew. Chemie Int. Ed., 2018, **57**, 16114–16119.
45 F. P. García de Arquer, O. S. Bushuyev, P. De Luna, C.-T. Dinh, A. Seifitokaldani, M. I. Saidaminov, C.-S. Tan, L. N. Quan, A. Proppe, M. G. Kibria, S. O. Kelley, D. Sinton and E. H. Sargent, 2D Metal Oxyhalide-Derived Catalysts for Efficient CO2 Electroreduction, *Adv. Mater.*, 2018, **30**, 1802858.
46 P. F. Liu, M. Y. Zu, L. R. Zheng and H. G. Yang, Bismuth oxyiodide microflower-derived catalysts for efficient CO2 electroreduction in a wide negative potential region, *Chem. Commun.*, 2019, **55**, 12392–12395.
47 M. Ramdin, A. R. T. Morrison, M. de Groen, R. van Haperen, R. de Kler, E. Irtem, A. T. Laitinen, L. J. P. van den Broeke, T. Breugelmans, J. P. M. Trusler, W. de Jong and T. J. H. Vlugt, High-Pressure Electrochemical Reduction of CO2 to Formic Acid/Formate: Effect of pH on the Downstream Separation Process and Economics, *Ind. Eng. Chem. Res.*, 2019, **58**, 22718–22740.
48 F. K. Bahnamiri, M. Khalili, P. Pakzad and M. Mehrpooya, Techno-economic assessment of a novel power-to-liquid system for synthesis of formic acid and ammonia, based on CO2 electroreduction and alkaline water electrolysis cells, *Renew. Energy*, 2022, **187**, 1224–1240.
49 V. V Belova, Y. A. Zakhodyaeva and A. A. Voshkin, Extraction of carboxylic acids with neutral extractants, *Theor. Found. Chem. Eng.*, 2017, **51**, 786–794.
50 L. M. J. Sprakel and B. Schuur, Solvent developments for liquid-liquid extraction of carboxylic acids in perspective, *Sep. Purif. Technol.*, 2019, **211**, 935–957.
51 J. C. Gentry and A. J. Solazzo Jr., Recovery of carboxylic acids from aqueous streams, *Environ. Prog.*, 1995, **14**, 61–64.
52 A. T. Laitinen, V. M. Parsana, O. Jauhiainen, M. Huotari, L. J. P. van den Broeke, W. de Jong, T. J. H. Vlugt and M. Ramdin, Liquid–Liquid Extraction of Formic Acid with 2-Methyltetrahydrofuran: Experiments, Process Modeling, and Economics, *Ind. Eng. Chem. Res.*, 2021, **60**, 5588–5599.
53 A. Del Castillo, M. Alvarez-Guerra, J. Solla-Gullón, A. Sáez, V. Montiel and A. Irabien, Sn nanoparticles on gas diffusion electrodes: Synthesis, characterization and use for continuous CO2 electroreduction to formate, *J. CO2 Util.*, 2017, **18**, 222–228.
54 E. Irtem, T. Andreu, A. Parra, M. D. Hernández-Alonso, S. García-Rodríguez, J. M. Riesco-García, G. Penelas-Pérez and J. R. Morante, Low-energy formate production from CO2 electroreduction using electrodeposited tin on GDE, *J. Mater. Chem. A*, 2016, **4**, 13582–13588.
55 M. Alvarez-Guerra, A. Del Castillo and A. Irabien, Continuous electrochemical reduction of carbon dioxide into formate using a tin cathode: Comparison with lead cathode, *Chem. Eng. Res. Des.*, 2014, **92**, 692–701.
56 W. Lee, Y. E. Kim, M. H. Youn, S. K. Jeong and K. T. Park, Catholyte-Free Electrocatalytic CO2 Reduction to Formate, *Angew. Chemie Int. Ed.*, 2018, **57**, 6883–6887.
57 F. Proietto, B. Schiavo, A. Galia and O. Scialdone, Electrochemical conversion of CO2 to HCOOH at tin cathode in a pressurized undivided filter-press cell, *Electrochim. Acta*, 2018, **277**, 30–40.
58 H. Yang, J. J. Kaczur, S. D. Sajjad and R. I. Masel, Electrochemical conversion of CO2 to formic acid utilizing Sustainion^{TM} membranes, *J. CO2 Util.*, 2017, **20**, 208–217.
59 C. Xia, P. Zhu, Q. Jiang, Y. Pan, W. Liang, E. Stavitski, H. N. Alshareef and H. Wang,

Continuous production of pure liquid fuel solutions via electrocatalytic CO2 reduction using solid-electrolyte devices, *Nat. Energy*, 2019, **4**, 776–785.

60 O. Scialdone, A. Galia, G. Lo Nero, F. Proietto, S. Sabatino and B. Schiavo, Electrochemical reduction of carbon dioxide to formic acid at a tin cathode in divided and undivided cells: effect of carbon dioxide pressure and other operating parameters, *Electrochim. Acta*, 2016, **199**, 332–341.

G. COST STATUS

The cost status reports the actual cost status of the award when compared with the original Baseline Cost Plan (i.e., the “Forecasted Cash Needs” originally provided on the SF-424A, Section D and as set forth in the Project Management Plan submitted with the Application and Revised with Task 1.0 of SOPO).

	Year 1: 09/01/20-08/31/21				Year 2: 09/01/21-08/31/22				Year 2: 09/01/22-08/31/23				Total
	Q1	Q2	Q3	Q4	Q1	Q2	Q3	Q4	Q1	Q2	Q3	Q4	
Forecasted													
Federal	$125,000	$125,000	$125,000	$125,000	$125,000	$125,000	$125,000	$125,000	$0	$0	$0	$0	$1,000,000
Non-federal	$31,250	$31,250	$31,250	$31,250	$31,250	$31,250	$31,250	$31,250	$0	$0	$0	$0	$250,000
Total	$156,250	$156,250	$156,250	$156,250	$156,250	$156,250	$156,250	$156,250	$0	$0	$0	$0	$1,250,000
Actual													
Federal	$150,000	$80,000	$125,000	$125,000	$125,000	$110,000	$50,000	$88,418	$96,141				$949,559
Non-federal	$37,500	$25,000	$31,250	$31,250	$31,250	$30,000	$20,000	$2,543	$13,025				$221,818
Total	$187,500	$100,000	$156,250	$156,250	$156,250	$140,000	$70,000	$90,961	$109,166				$1,057,211
Variance													
Federal	$25,000	-$45,000	$0	$0	$0	-$15,000	-$75,000	$36,582.44	$96,141				-$13,859
Non-federal	$6,250	-$6,250	$0	$0	$0	-$1,250	-$11,250	$28,706.05	$13,025				$0
Total quarterly	$31,250	-$51,250	$0	$0	$0	-$16,250	-$86,250	$65,288.49	$109,166				-$122,500
Cumulative Variance	$31,250	-$20,000	-$20,000	-$20,000	-$20,000	-$36,250	-$122,500	-$187,788	-$78,622				-$78,622

***:** A 12-month no-cost extension was requested.

H. PROJECT DELIVERABLES AND TIMELINE

REPORT DE-FE-0031919

WBS	Title	FY2021				FY2022				Planned Start Date	Planned End Dates	Acutal Start Date	Actual End Date
		Q1	Q2	Q3	Q4	Q5	Q6	Q7	Q8				
1	Task 1. Project Management, Planning and Reporting	■	■	■	■	■	■	■	■	9/1/2020	8/31/2022	9/1/2020	
2	Task 2. Design and fabricate tandem electrodes	■	■	■	■	■	■			9/1/2020	1/31/2022	9/1/2020	6/30/2021
3	Task 3. Develop graded catalyst layers		■	■	■					1/1/2021	8/31/2021	1/1/2021	8/31/2022
4	Task 4. Develop Pulsed Electrolysis Protocols		■	■	■	■	■	■	■	2/1/2021	1/31/2022	3/30/2021	3/31/2022
5	Demonstrate MEA-type cells for high efficiency conversion		■	■	■	■	■	■	■	2/1/2021	8/31/2022	3/1/2021	08/31/2022
6	Techno-economic analysis with technology gap analysis		■	■	■	■	■	■		2/1/2021	8/31/2023	4/1/2021	
7	Life-cycle anlaysis					■	■	■	■	1/1/2022	8/31/2022	1/1/2022	4/30/2022

I: PERSONNEL

The contractor will be University of Louisiana at Lafayette and the PI will be Professor Xiao-Dong Zhou. At the University of Cincinnati, the PI will be Professor Jingjie Wu. They will be assisted by postdoctoral fellows and student researchers.

Dr. Xiao-Dong Zhou is the Stuller Endowed Chair and Director of the Institute for Materials Research and Innovation at the University of Louisiana at Lafayette. Prior to that, he was a Professor at the University of South Carolina from 2010 to 2017 and a Senior Research Scientist at the Pacific Northwest National Laboratory from 2005 to 2010. He obtained his Ph.D. in Ceramic Engineering from University of Missouri Rolla. Dr. Zhou received *J. B. Wagner Jr. Young Investigator Award* in 2007 from the Electrochemistry Society (ECS) - High Temperature Materials Division and DOD DARPA's Young Faculty Award in 2011. He currently serves as the Technical Editor for the Journal of The Electrochemical Society in *Fuel Cells, Electrolzyers, and Energy Conversion*. Dr. Zhou's research interest focuses on synthesis, characterization, and theoretical understanding of materials for fuel cells, electrolyzers, and batteries.

Dr. Jingjie Wu is an Assistant Professor at the University of Cincinnati. He has 10+ years of R&D experience in the development of novel materials for renewable energy storage and conversion, such as electrolysers for CO_2 conversion, PEM fuel cells, and Li-ion batteries. His publications span the areas of the design and synthesis of atomic-scale catalysts, thermo-/photo-/electro-chemical conversion of C_1 molecules (e.g., CO_2, CO, and CH_4) to value-added chemicals or fuels, and materials for PEMFCs. He has published 80+ peer-reviewed articles and received 3 US patents/disclosures. Dr. Wu received ORAU Ralph E. Powe Junior Faculty Enhancement Awards in 2018 and University Research Council Faculty Research Award in 2018 from UC, and was recognized as Emerging Investigators 2021 by the Royal Society of Chemistry.

Dr. Xiang Lyu is a postdoc in the Co-PI (Wu)'s group. He received Ph.D. degree in Chemical Engineering from the Ohio University. Dr. Lyu's research will focus on the MEA electrolyzer for CO_2 conversion.

Mr. Tianyu Zhang is a Ph.D. candidate working in the Co-PI (Wu)'s group. He received B.S. degree from the East China University of Science and Technology. Mr. Zhang's research will focus on tandem electrode design and manufacturing.